EFFECTS OF CLIMATE CHANGE ON WIND LOADING FOR STRUCTURAL DESIGN

by

Jennifer Thompson

Submitted in partial fulfillment of the requirements
for the degree of Master of Science

at

Dalhousie University
Halifax, Nova Scotia
March 2021

Table of Contents

List of Tables

List of Figures

Abstract

Structural design requirements need to be updated to account for the projected increases in the frequency and intensity of extreme wind events due to climate change. This study investigates the effects of climate change on the wind loading design parameters used in the National Building Code of Canada. The projected changes to wind speed statistical distributions and the magnitude of uncertainty in these projections are assessed using state-of-the-art climate change models. Three new wind loading design methods that can be used under climate change are developed based on the "ultimate return period" and Load and Resistance Factor Design methods. Analyses of these three methods, proposed herein, demonstrate that the "Hybrid Ultimate Return Period" (HURP) method performs the best under climate change, since its probabilities that the HURP design wind speeds are exceeded over the 50-year design lifetime are most consistent across Canada, compared to the other two methods.

List of Abbreviations and Symbols

NBCC National Building Code of Canada

NRCC National Research Council of Canada

CHBDC Canadian Highway Bridge Design Code

LRFD Load and Resistance Factor Design

ULS ultimate limit state

SLS serviceability limit state

FORM first-order reliability method

CDF cumulative distribution function

EVT extreme value theory

POT peaks over threshold

GEVD generalized extreme value distribution

GPD generalized Pareto distribution

MML method of maximum likelihood

AIC Akaike information criterion

i.i.d. independent and identically distributed

PMF probability mass function

ECCC Environment and Climate Change Canada

SSE sum of squared errors

EC Environment Canada

NLLH negative log likelihood

IPCC Intergovernmental Panel on Climate Change

RCP Representative Concentration Pathway

ESM earth system model

GCM global climate model

RCM regional climate model

SLP atmospheric pressure at sea level

CMIP5 Coupled Model Intercomparison Project Phase 5

SRES Special Report on Emissions Scenarios

RMSD root mean squared difference

CRCM5 Canadian Regional Climate Model

CanESM2 Canadian Earth System Model 2

MPI-ESM Max-Planck-Institute Earth System Model

MOM method of moments

MSLP mean sea level pressure

GEM Global Environmental Multiscale

ERA ERA-Interim reanalysis dataset

CanHist CanESM2 over the 1981-2010 period

MME multimodel ensemble

GLS generalized least-squares

PDF probability density function

ASCE-7 *ASCE-7 Minimum Design Loads For Buildings and Other Structures*

ASCE American Society for Civil Engineers

AURP All-Inclusive Ultimate Return Period

HURP Hybrid Ultimate Return Period

ϕ resistance factor

$\hat{R}_u$ characteristic ultimate resistance

$\hat{F}_k$ k'th characteristic load

α_k load factor corresponding to the k'th load

$\hat{F}_D$ characteristic dead load

$\hat{F}_L$ characteristic live load

$\hat{F}_W$ characteristic wind load

α_p load factor for the permanent load

α_i load factor for the principle transient load

α_{ij} load factor for the companion-action transient loads

S_p permanent load

S_i principle transient load

S_j companion-action transient load

β_T target reliability index for design lifetime T

β reliability index for a given load combination

$q_{A1,50}$ fifty-year return period annual maximum one-hourly average wind pressure

I_W importance factor

C_e exposure factor

C_t topographic factor

C_g gust effect factor

C_p external pressure coefficient

ρ_{air} density of air

$v_{A1,50}$ fifty-year return period annual maximum one-hourly average wind speed

$X(t)$ random variable at point t

Ω sample space

$\mu_X(t)$ mean function of a random variable, X

$\mathrm{Cov}(X_{t_1}, X_{t_2})$ autocovariance function of a random variable, X

τ time difference between any points t_2 and t_1

$F_{v_{A1}}(v)$ CDF of the annual maximum one-hourly average wind speed distribution

u location parameter

a scale parameter

ξ shape parameter

r large threshold

Z exceedance of a random variable X over a threshold, r

$u_{v_{A1}}$ location parameter of the annual maximum one-hourly average wind speed

$a_{v_{A1}}$ scale parameter of the annual maximum one-hourly average wind speed

$\mu_{v_{A1}}$ mean of the annual maximum one-hourly average wind speed

$\sigma_{v_{A1}}$ standard deviation of the annual maximum one-hourly average wind speed

m return period

r_m threshold with annual exceedance probability, $p = 1/m$

p annual exceedance probability

N_n number of years until the next exceedance event

N_m number of exceedance events in m years

m_1 expected number of years until the next exceedance event

m_2 number of years with one expected number of exceedance event

$V(t)$ instantaneous wind speed at time t

W longer term averaging duration

$V_W(t)$ longer term average wind speed over duration W at time t

$U(t)$ unsteady gust fluctuations about $V_W(t)$ at time t

$V_{AW,m}$ m-year return period W-average annual maximum wind speed

T any averaging duration

$V_T(t)$ T-average wind speed

$\hat{\mu}_{V_T}$ sample mean of the T-average wind speed

$\hat{\sigma}^2_{V_T}$ sample variance of the T-average wind speed

$\gamma(T)$ variance reduction function

σ_V^2 variance of the instantaneous wind speed

$\sigma_{V_T}^2$ variance of the T-average wind speed

$\rho(\tau)$ correlation function

θ Markov process correlation length

$G(\omega)$ one-sided spectral density function

ω frequency

ζ spectral power parameter

G_o spectral intensity

δ local averaging distance

H Hurst coefficient

$\hat{\sigma}_V^2$ estimated variance of the instantaneous wind speed

$\overline{\hat{\sigma}_{V_T}^2}$ normalized estimate of the T-average wind speed variance such that $\overline{\hat{\sigma}_{V_{2\text{-min}}}^2} = 1$

$\overline{\theta}$ best-fit Markov correlation length to $\overline{\hat{\sigma}_{V_T}^2}$

$\overline{\delta}$ best-fit local averaging distance to $\overline{\hat{\sigma}_{V_T}^2}$

$\overline{H}$ best-fit Hurst coefficient to $\overline{\hat{\sigma}_{V_T}^2}$

$\overline{\gamma}(T)$ Markov process variance reduction function where $\theta = \overline{\theta}$ or, fractal process variance reduction function where $\delta = \overline{\delta}$ and $H = \overline{H}$

μ_{V_W} mean of W-average wind speed

σ_{V_W} standard deviation of the W-average wind speed

z_m distance from μ_{v_W} to the m-year return period annual maximum W-average wind speed measured in standard deviation units

$v_{A1,m}$ m-year return period annual maximum one-hourly average wind speed

G gust factor

w short-term averaging duration

$\hat{v}_w$ statistical measure of the w-averaged peak gust wind speed

v_W a value of $V_W(t)$

$g(w, W)$ peak factor

$\sigma_u(w, W)$ standard deviation of the gust fluctuations, $U(t)$

Φ CDF of the standard normal distribution

$\hat{v}_{w,i}$ maximum w-averaged gust speed

$V_w(t)$ short-term average wind speed over duration w at time t

μ_{V_w} mean the short-term w-average wind speed, V_w

σ_{V_w} standard deviation of the short-term w-average wind speed, V_w

$Y_w(t)$ standard normal random variable corresponding to $V_w(t)$

$Y_W(t)$ standard normal random variable corresponding to $V_W(t)$

μ_V mean of the instantaneous wind speed

$\mathrm{Cov}(Y_w, Y_W)$ covariance between $Y_w(t)$ and $Y_W(t)$

CV_V instantaneous wind speed coefficient of variation

Δ_μ rate of change in mean of a non-stationary distribution

Δ_σ rate of change in standard deviation of a non-stationary distribution

y year

$V_{A1}(y)$ annual maximum one-hourly average wind speed in year y

$\mu_{v_{A1}}(y)$ non-stationary mean of the annual maximum one-hourly average wind speed in year y

$\sigma_{v_{A1}}(y)$ non-stationary standard deviation of the annual maximum one-hourly average wind speed in year y

$F_{v_{A1}}(v; y)$ CDF of the annual maximum hourly-average wind speed in year y

$a_{v_{A1}}(y)$ non-stationary scale parameter of the annual maximum one-hourly average wind speed in year y

$u_{v_{A1}}(y)$ non-stationary location parameter of the annual maximum one-hourly average wind speed parameter in year y

Θ non-stationary Gumbel distribution parameters

b_i observed block maxima

$p(y)$ non-stationary annual exceedance probability for year y

M_y annual maximum for year y

$F(x; y)$ non-stationary extreme value distribution

N_{m_2} number of exceedance events in m_2 years

I indicator variable

c scale factor for $v_{AH,50}$ required to maintain a 50-year return period

p_{50} fifty-year lifetime exceedance probability

$\mathrm{CV}_V(y)$ instantaneous wind speed coefficient of variation in year y

$\mu_V(y)$ instantaneous wind speed mean in year y

$\sigma_V(y)$ instantaneous wind speed standard deviation in year y

$G_y(w, W)$ non-stationary gust factor in year y

v_{A0} annual maximum wind speed based on 3-hourly instantaneous observations

$v_{A0,50}$ fifty-year return period annual maximum wind speed based on 3-hourly instantaneous observations

CV coefficient of variation

v_{NBCC} fifty-year return period annual maximum one-hourly average wind speed given in the NBCC

$\%D_v$ percent difference between $v_{A1,50}$ and v_{NBCC}

v_{FD} current factored design wind speed

$p_{v_{FD}}$ annual probability that is v_{FD} exceeded

p_e annual exceedance probability target

p_{50} 50-year exceedance probability

C_c climate change effect factor

$v_{FD,CC}$ factored design wind speed under climate change

u_{CC} climate change model uncertainty factor

η_{CV_y} total relative increase in CV_V over y years

$\mathrm{CV}_{\mathrm{V_{A1}}}$ coefficient of variation of the annual maximum one-hourly average wind speed

$F_{v_{A1,50}}(v)$ CDF of $v_{A1,50}$

$u_{v_{A1,50}}(v)$ location parameter of $v_{A1,50}$

$a_{v_{A1,50}}(v)$ scale parameter of $v_{A1,50}$

$f_{v_{A1,50}}(v)$ PDF of $v_{A1,50}$

m_U current ultimate return period

v_{A1,m_U} annual maximum one-hourly average m_U-year return period wind speed

$v_{AU,CC}$ All-Inclusive Ultimate Return Period method design wind speed

$v_{A1,m_{AU}}$ annual maximum one-hourly average m_{AU}-year return period wind speed

m_{AU} all-inclusive ultimate return period

$q_{A1,m_{AU}}$ annual maximum one-hourly average m_{AU}-year return period wind pressure

m_{HU} hybrid ultimate return period

$C_{c,HU}$ hybrid climate change effect factor

$v_{A1,m_{HU}}$ annual maximum one-hourly average m_{HU}-year return period wind speed

v_{CC} wind speed with p_{50} equal to a given target under a climate change scenario where $\Delta_\mu > 0$ and $\Delta_\sigma = 0$

$v_{HU,CC}$ Hybrid Ultimate Return Period method design wind speed

p_d d-year exceedance probability

p_{75} 75-year exceedance probability

p_{100} 100-year exceedance probability

Acknowledgements

I would like to express many thanks to Dr. Gordon A. Fenton, my research supervisor, for providing me with this opportunity to broaden my experience and knowledge. Dr. Fenton's thoughtful guidance, constructive criticism and encouragement have been incredibly helpful throughout the development of this work. I am sure I will continue to benefit from Dr. Fenton's mentorship throughout my career, for which I am beyond grateful.

I am appreciative of the generous financial support provided by the National Sciences and Engineering Research Council of Canada (NSERC) Graduate Scholarship, the Bruce and Dorothy Rosetti Engineering Graduate Scholarship, the Dr. Gillespie Engineering Graduate Scholarship and Dalhousie University funding, without which this work would not have been possible.

I am grateful for my committee members, Dr. Farzaneh Naghibi and Dr. Joanna Mills Flemming, for their insightful guidance throughout the development of this thesis.

I would also like to thank my colleagues in the Engineering Mathematics Department for their support throughout this experience. A special thanks to Claire Chisholm, whose thoughtfulness always brightens my day.

Finally, I wish to extend my deepest gratitude to my family for their continuous love, encouragement and support throughout my entire academic career.

Chapter 1

Introduction

1.1 Motivation

Greenhouse gas emissions caused by human activity have undoubtedly raised the global average temperature relative to pre-industrial levels. In 2017, human-induced global average warming reached approximately 1°C relative to the average temperature from 1850 to 1900 (Allen et al., 2018). While past emissions alone are unlikely to raise the global average temperature more than 1.5°C (Allen et al., 2018), future human behaviour will dictate the magnitude of global warming over the next century. In addition to global warming, increased concentrations of greenhouse gas emissions have also greatly disrupted other aspects of the atmospheric climate. The term *climate change* refers to significant variation in long-term weather patterns. Changes in the frequency, intensity, spatial extent, duration and timing of extreme weather events due to climate change are a major global concern. Observational data collected since 1950 already shows evidence of changes in extremes, such as heavy precipitation events, daily temperature extremes and extratropical storms (Seneviratne et al., 2017). Natural climate variability, including phenomena such as El Niño, as well as decadal and multi-decadal variations influence many weather and climate extremes. For example, hurricanes are heavily influenced by ocean water temperatures. In addition, there is strong evidence that anthropogenic factors also influence such extreme weather events (Seneviratne et al., 2017). The results of some of these extreme weather events can be dire. In the period 2017 to 2020 extreme weather events have been the top-ranked global risk in terms of likelihood, while climate action failure was ranked second in 2019 and 2020. Climate action failure was the top-ranked global risk in terms of impact in 2020, while extreme weather event ranked fourth in terms of impact (behind weapons of mass destruction and biodiversity loss) (World Economic Forum, 2020). In other words, urgent action is required to reduce vulnerability

and exposure to the harmful effects of climate change, but determining the most appropriate response can be challenging. Projected changes are unknown due to the uncertainty in future human behaviour, and ill-designed mitigation plans could pose negative socioeconomic consequences, especially for poverty stricken regions.

Canadian structural design requirements are one area that needs to be updated to account for projected changes in extreme climatic events. Building codes are developed to ensure structures will resist extreme lifetime climatic loads, such as wind, rainfall and snow loads, to an acceptable probability. The National Building Code of Canada (NBCC), provides design load requirements for most locations across the country. Climatic design values include quantities such as the 50-year return period "worst storm" climatic loads. The current climatic loads were developed using historical data, and assume "steady" conditions. That is, the mean and variance of these storms are assumed constant over time. However, it is highly probable that the Canadian climate will change significantly in the future as a result of global warming. In the current NBCC, it is acknowledged that some regions may see an increase in the frequency and intensity of many weather extremes, but specific guidelines to account for these changes are not provided (National Research Council of Canada (NRCC), 2015).

Studies on updating wind loading design requirements and analysis of uncertainties in wind speed projections are currently a high priority. At this time, there is low confidence in extreme wind projections, meaning that whether the extreme wind speeds will increase or decrease is currently poorly known. This lack of certainty is due to the limited number of studies completed, and inconsistencies in the projected changes resulting from deficiencies in the simulation models (Seneviratne et al., 2017). While there is some literature that attempts to predict future wind speeds and uncertainties, to the author's knowledge there are no studies that assess the effects of climate change on wind loading for structural design requirements.

1.1.1 Thesis Objective

The objective of this thesis is to develop future wind loading design requirements that (a) account for the projected changes in wind speeds and uncertainties due to climate change and (b) improve exceedance probability consistency across Canada.

This study suggests reformulations of the statistical distributions typically used to model wind speeds across the country. State-of-the-art climate change models are used to develop these reformulated statistical distributions. Additionally, the sources of uncertainty, and associated magnitudes, in these climate change models are assessed and incorporated into the new design wind load requirements. To improve exceedance probability consistency, alternative design methods are implemented and compared to the current design method used in the NBCC.

1.2 Load and Resistance Factor Design Methodology

Both the Canadian Highway Bridge Design Code (CHBDC) and the NBCC utilize the Load and Resistance Factor Design (LRFD) methodology, a probabilistic approach to structural design that aims to achieve reliability targets, or acceptable probabilities of failure. The definition of *failure* is dependent on whether the limit state being considered is the ultimate limit state (ULS) or the serviceability limit state (SLS). The ULS is primarily concerned with structural collapse, while the SLS refers to conditions that impede the intended use of the structure. The LRFD methodology breaks down the various types of loads and applies a separate factor to each load type and to the resistance. This factor accounts for the uncertainty associated with each component. The general LRFD equation for the ULS is given as

$$\phi \hat{R}_u \geq \sum_k \alpha_k \hat{F}_k \tag{1.1}$$

where ϕ is the resistance factor, $\hat{R}_u$ is the characteristic ultimate resistance, α_k is the load factor corresponding to the k'th load, and $\hat{F}_k$ is the k'th characteristic load (NRCC, 2015). The *characteristic* value refers to the predicted design value.

Load or resistance factors are calibrated using the statistical distributions of the corresponding load or the resistance. This ensures that the probability of failure meets target reliability levels, where the probability of failure is the probability that the load exceeds the resistance capacity. Figure 1.1 demonstrates the importance of considering each load component's statistical distribution when calibrating its associated load factor.

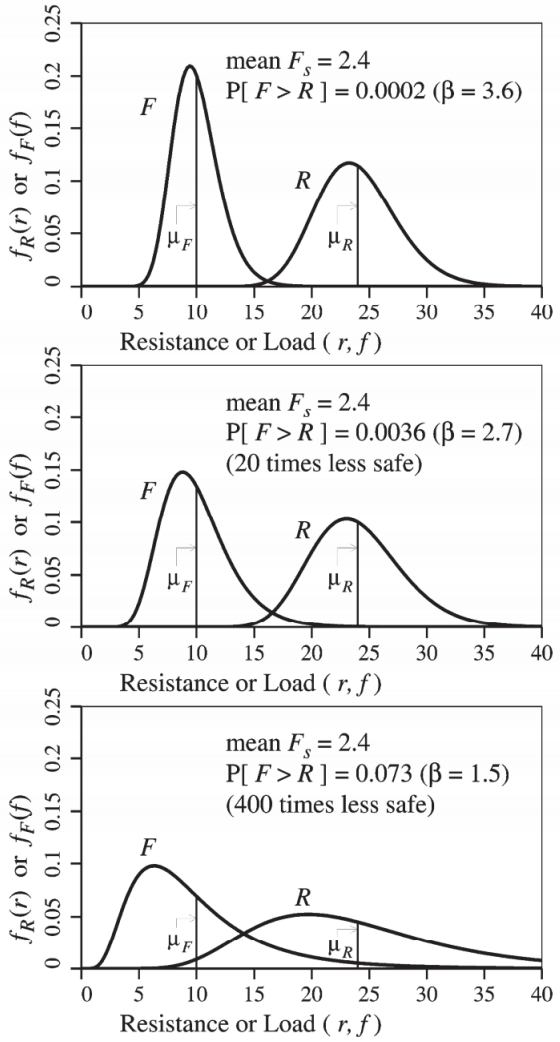

Figure 1.1: Three geotechnical systems having resistance R under load F can have precisely the same mean factor of safety and yet very different failure probabilities, $P[F > R]$ (Fenton et al., 2015).

The mean load and resistance in each plot in Fig. 1.1 are equal, but the differences in variability result in the probability of failure being 400 times greater in the bottom plot than that of the top plot. Consequently, each load factor should be different, taking into account the width of the associated load distribution. In the NBCC, the LRFD equation for wind loading, where the wind is acting as a principal load, is given as

$$\phi \hat{R}_u \geq 1.25\hat{F}_D + 0.5\hat{F}_L + 1.4\hat{F}_W \tag{1.2}$$

where $\hat{F}_D$ is the dead load, which is a "permanent load due to the weight of *building* components", $\hat{F}_L$ is the live load, "a variable load due to intended use and occupancy", and $\hat{F}_W$ is the wind load, which is also variable (NRCC, 2015).

In eq. (1.2) the dead load factor, 1.25, is less than the wind load factor, 1.4, because there is less variability in the dead load than in the wind load. The live load factor is 0.5, in this particular load combination, since there is a very low probability of the lifetime maximum wind load and maximum live load occurring simultaneously. The resistance factor, ϕ, is dependent on the material and design of the structure.

It should be noted that the research presented in this thesis is solely focused on the wind load factor, α_W, and characteristic wind load, $\hat{F}_W$. Specifically, this research investigates how these values need to be modified to achieve consistent reliability across Canada, given projected changes in extreme wind loads due to climate change.

1.2.1 Calibration of Load Factors

Load factor values used for design are calibrated considering the distributions of the loads and the way that they are combined in the LRFD formulation. Two main approaches to combining loads could be used in the LRFD equation. The first is the so-called companion-action format, the approach used in the current NBCC, which is a reliability-based approach that combines loads simultaneously. The second is the so-called probability factor design format, used in the NBCC up until 2005, which involves the use of a separate load combination factor (Madsen et al., 2006). The objective of these load combination formats is to develop simple, structured design methodologies that account for the temporal and spatial variations of the individual loads (Kariyawasam, 1996). The companion-action format is based on Turkstra's rule which states that the maximum lifetime load is most likely to occur when one variable is at its maximum lifetime value, and the others are at more frequent values (Madsen et al., 2006). The companion-action format is now utilized in the NBCC because it is simple, and it models real load combinations more accurately than the probability factor method (Bartlett et al., 2003*b*). The companion-action load combinations take the general form

$$\alpha_p S_p + \alpha_i S_i + \sum_{i \neq j} \alpha_{ij} S_j \tag{1.3}$$

where α_p is the load factor for the permanent load (e.g. dead load), S_p, and α_i is the load factor for the principle transient load, S_i, (normally the live load) assumed to be at its maximum lifetime value. The load factors α_{ij} are for the companion-action transient loads, S_j, that act on the structure while the principle load is at its maximum value (Bartlett et al., 2003*b*).

The basic steps of the load factor calibration procedure include (1) estimating the implied target reliability, β_T, used in current design standards, and (2) estimating the load factors such that the desired β_T levels is achieved. The subscript T refers to the design lifetime, so that β_T is the target reliability index over T years. (Ellingwood et al., 1980). In the NBCC, the extensively employed first-order reliability method (FORM) is commonly used to estimate the reliability index for various design situations (see, e.g., Bartlett et al., 2003*a*). Given β_T, the load factors are then determined as those values, α_i, that minimize a function which measures the "distance" between the target reliability, β_T, and the reliability of the particular load combinations, β (Ellingwood et al., 1980). The reliability index of the given load combination, β, is also typically evaluated using the FORM.

In order to achieve target reliability levels for the designed system, the calibration of load factors must include consideration of the variability of the resistance side of the LRFD equation, as well as the load side. To include the resistance side, the calibration must be specific to various possible failure modes of the system, for example, bending of a steel beam, crushing of a masonry block, etc. To simplify the calibration problem, the wind speed exceedance probability alone may be held constant from that obtained from current design levels. This assumption allows the calibration of load factors to proceed simply by looking at the factors required to achieve a sufficiently small probability that the wind speed will exceed the factored design wind speed. The research performed in this thesis makes this assumption. The target exceedance probability is then selected from currently acceptable exceedance probabilities so that the system reliability is as predicted by previous calibrations of load factors (e.g., Bartlett et al., 2003*a*).

1.2.2 Reliability Indices

The current target reliability indices used in design codes were developed by calibrating to older practices and making any necessary adjustments, as target reliability indices are dictated by what society deems acceptable in terms of balancing safety requirements and economic considerations. Bartlett et al. (2003*a*) determined the current target reliability index used in the NBCC by implementing the FORM to evaluate the implied reliability indices for steel structural members designed using the 1995 edition of the NBCC. Bartlett et al.'s (2003*a*) results suggested a 50-year design life target reliability index of 3.0 for the load combination including the dead load acting simultaneously with the live load, and 2.8 for load combinations involving the dead load plus either the wind load or snow load. Bartlett et al. (2003*a*) then calibrated load factors for the NBCC based on these findings. The load factors estimated by Bartlett et al. (2003*a*) are still used in the current NBCC (2015).

The current NBCC target reliability index is consistent with results in the literature. For example, Allen (1992) determined a reliability index between 2.0 and 3.75 for Canadian highway bridge design (i.e., Clause 12 of CAN/CSA-S6-88) based on calibration to past experience and life-safety considerations. The target reliability index varies because it is chosen by the evaluator as a function of structural behaviour (e.g., gradual or sudden failure), level of inspection and evaluation, and traffic category. Additionally, Ellingwood et al. (1980) analysed the 1980 ANSI A58 building and structural design standard and found that for steel beams the target reliability index was 3.0 for load combinations of dead load plus live load, and dead load plus snow load. However, the target reliability index was 2.5 for the dead load acting simultaneously with the live load and wind load. Similar results were also found for concrete beams with Grade 40 and Grade 60 reinforcement (Ellingwood et al., 1980). The lower reliability indices for load combinations involving wind loads are a result of calibrating to inconsistent older practice (Ellingwood, 1994). This may suggest the minimum value of 2.8 used in the NBCC for load combinations with wind or snow loads should be increased to 3.0.

1.3 Traditional Statistical Modelling of Extreme Wind Speeds

The characteristic wind load, $\hat{F}_W$, used in the NBCC is a function of the reference wind velocity pressure, as well as several factors related to the importance of the building (e.g., hospital vs. residential home), the topography of the location (i.e., urban or rural), and the size and shape of the building. The reference wind velocity pressure is the 50-year return period annual maximum one-hourly average wind pressure, $q_{A1,50}$, where the subscript A refers to annual maximum, the subscript 1 refers to one hour average, and the subscript 50 refers to the defined return period. Using the static procedure provided in the NBCC, $\hat{F}_W$ is given as

$$\hat{F}_W = I_W q_{A1,50} C_e C_t C_g C_p \tag{1.4}$$

where I_W is the importance factor, C_e is the exposure factor, C_t is the topographic factor, C_g is the gust effect factor, and C_p is the external pressure coefficient. The design wind pressure is defined as

$$q_{A1,50} = \frac{1}{2}\rho_{air} v_{A1,50}^2 \tag{1.5}$$

where ρ_{air} is the density of air, and $v_{A1,50}$ is the 50-year return period annual maximum one-hourly average wind speed. Statistical models of $q_{A1,50}$ typically focus on the 50-year return period wind speed, $v_{A1,50}$, because the density of air can be considered constant with time at any specific elevation. This study only investigates $v_{A1,50}$ and C_g, since I_W, C_e, C_t and C_p are assumed to not be affected by climate change.

1.3.1 Stochastic Processes in Time

Extreme wind speeds at a specific location can be derived using a stochastic process in time. A stochastic process is a collection of random variables indexed by some set S, usually representing time, and can be written as $X(t)$, where $t \, \epsilon \, S$. Each random variable in a stochastic process, $X(t)$, takes a value from the common sample space, Ω. A stochastic processes may be either discrete or continuous in time, and can be characterized by its mean function, $\mu_X(t) = E[X(t)]$, and autocovariance function, $\text{Cov}(X_{t_1}, X_{t_2}) = E[(X(t_1) - \mu_X))(X(t_2) - \mu_X)]$.

A stochastic process is considered strictly stationary if all the random variables are identically distributed, meaning for any $t \, \epsilon \, S$ the random variable $X(t)$ has the

same probability distribution. A stochastic process is considered weakly stationary if the mean is constant and the autocovariance function depends only on the time difference, $\tau = t_2 - t_1$. Therefore, a stationary stochastic process is independent of where it is formed along the time axis.

Currently, extreme wind speeds are assumed to be weakly stationary. That is, the probability distribution of the annual maximum wind speed is assumed to have a constant mean and autocovariance. The cumulative distribution function (CDF) used to model the annual maximum one-hourly average wind speed distribution is given by $F_{v_{A1}}(v)$, and is determined based on historical data using extreme value theory.

1.3.2 Extreme Value Theory

The probability distribution of the annual maximum one-hourly average wind speed, $F_{v_{A1}}(v)$ is determined using extreme value theory (EVT). EVT is a branch of statistics that deals with modelling the probability distribution of rare events (i.e., the tails of a distribution). The two main approaches to extreme value analysis are the block maxima method and the peaks over threshold (POT) method. The block maxima method involves dividing the data series into non-overlapping blocks of equal size and selecting the maximum (or minimum) value in each period (Faranda et al., 2011). This method was first developed by Fisher and Tippett (1928) and formalized by Gnedenko (1943) who showed that the distribution of block maxima of a sample of independent and identically distributed (i.i.d.) variables follow the so-called generalized extreme value distribution (GEVD), of which the Gumbel, Fréchet and Weibull distributions are special cases. The CDF of the GEVD is defined as

$$\text{GEVD}(x) = \begin{cases} \exp\left(-\left[1+\xi(\frac{x-u}{a})\right]^{-1/\xi}\right), \text{ for } \xi \neq 0 \\ \exp\left(-\exp(\frac{x-u}{a})\right), \text{ for } \xi = 0 \end{cases} \tag{1.6}$$

where u is the location parameter, a is the scale parameter, and ξ is the shape parameter. The main problem with the block maxima method is data are typically limited in practical applications and using only the maximum value of each block further reduces this limited sample size, inhibiting the ability to accurately determine the extreme value distribution.

The POT method also estimates the probabilities of extreme events, but uses

data more efficiently than the block maxima approach, as the POT method uses all observations above a threshold, r. While information loss is minimized, the problem of selecting an appropriate threshold arises. The POT method was introduced by Pickands et al. (1975) who showed that the distribution of exceedances over a large threshold r, (i.e., $Z_t = X_t - r|X_t > r$) follows the generalized Pareto distribution (GPD), as $r \to \infty$. The GPD CDF is given as

$$\mathrm{GPD}(z) = \begin{cases} 1 - \left(1 + \xi(\frac{z-u}{a})\right)^{-1/\xi}, \text{ for } \xi \neq 0 \\ 1 - \exp(-\frac{y-u}{a}), \text{ for } \xi = 0 \end{cases} \tag{1.7}$$

Both the block maxima and POT methods have been used to model the distribution of extreme wind speeds. The Gumbel distribution (GEVD where $\xi = 0$) is the most widely used model for the extreme wind speed analysis, however, the GEVD and GPD have also been considered (Hong et al., 2014a). The block maxima method is the most commonly used approach because of its simplicity in data processing by using the annual extremes. In comparison, the POT method requires selecting a threshold and inspecting each point to ensure they are from independent events (Hong et al., 2014a). Using the POT method for the NBCC is also impractical, as multi-year wind speed records from hundreds of weather stations would need to be analyzed. Consequently, the block maxima method is used for determining the design wind speeds in the NBCC.

Hong et al. (2014a) used the block maxima method to determine the most appropriate distribution for extreme wind speeds. Hong et al. (2014a) compared fitting the Gumbel distribution and the GEVD to annual maximum wind speed data from 235 stations using the method of maximum likelihood (MML) and found that the Gumbel distribution is preferred in over 70% of cases based on the Akaike information criterion (AIC). Their results validated that the Gumbel distribution should be the most widely used model for extreme wind speed analysis. The CDF used in this thesis then for the annual hourly-average maximum wind speed is the Gumbel distribution, given by

$$F_{v_{A1}}(v) = \exp\left(-\exp\left(-\frac{v - u_{v_{A1}}}{a_{v_{A1}}}\right)\right) \tag{1.8}$$

where $u_{v_{A1}}$ is the location parameter and $a_{v_{A1}}$ is the scale parameter. The mean, $\mu_{v_{A1}}$, and standard deviation, $\sigma_{v_{A1}}$, are given by $u_{v_{A1}} + 0.5772 a_{v_{A1}}$ and $a_{v_{A1}}\pi/\sqrt{6}$,

respectively.

1.3.3 Return Period Under Stationary Conditions

Traditionally, return period is defined as the inverse of the probability that the annual maximum event exceeds a threshold, r_m, in any given year (Cooley, 2013). Simply put, the m-year return period has an annual exceedance probability $p = 1/m$. Under stationary conditions, an equivalent interpretation of the m-year return period is that the expected number of exceedance events in m years is one (Cooley, 2013; Olsen et al., 1998). To derive these relationships, the annual exceedance probability, p, is assumed to be constant and annual exceedance events are assumed to be independent and identically distributed (i.i.d.). The number of years until the next exceedance event, N_n, then follows the geometric distribution (treating each year as a discrete trial) with probability mass function (PMF) given as (Read and Vogel, 2015)

$$f(n_n) = \Pr(N_n = n_n) = (1-p)^{y-1}p, n_n = 1, 2, ... \tag{1.9}$$

The expected return period is therefore

$$m = \mathrm{E}[N_n] = \sum_{n_n=1}^{\infty} n_n(1-p)^{n_n-1}p = \frac{1}{p} \tag{1.10}$$

If N_m is the number of exceedance events in m years, then N_m follows the binomial distribution (in the discrete case) given as (Cooley, 2013)

$$f(k) = \Pr(N_m = k) = \binom{m}{k} p^j (1-p)^{m-k} \tag{1.11}$$

The expected number of exceedance events in m years is therefore

$$\mathrm{E}[N_m] = mp = 1 \tag{1.12}$$

Given the above definitions, the 50-year return period annual maximum one-hourly average wind speed, $v_{A1,50}$, is the value that has an annual exceedance probability of 2%, or 1-in-50. This 50-year return period wind speed is estimated as

$$\hat{v}_{A1,50} = F_{v_{A1}}^{-1}\left(1 - \frac{1}{50}\right) \tag{1.13}$$

where $F_{v_{A1}}(v)$ is the annual maximum one-hourly average wind speed distribution given in eq. (1.8) with parameters to be discussed in Section 3.2.

1.3.4 Effects of Wind Speed Averaging Duration

Instantaneous wind speeds, $V(t)$, can be considered to be the sum of a longer term average wind speed over duration W, $V_W(t)$, plus an instantaneos unsteady component, $U(t)$, that fluctuates around $V_W(t)$ (Reynolds, 1895; Harper et al., 2010). That is, $V(t) = V_W(t) + U(t)$, where both $V_W(t)$ and $U(t)$ are stationary stochastic processes. Therefore, to predict the expected maximum lifetime wind speed used for structural design, it is necessary to estimate the distributions of both $V_W(t)$ and $U(t)$. These distributions can then be used to evaluate the design wind speed, which is the m-year return period W-average annual maximum wind speed, $V_{AW,m}$, as well as the expected maximum short-term deviation from $V_{AW,m}$. The expected maximum short-term deviation from $V_{AW,m}$ is referred to as the peak gust speed, defined as the highest short-duration average wind speed within a stated observation period (Harper et al., 2010), which is W in this case. The peak gust speed should be considered for the design of small buildings that are "completely enveloped by wind gusts", however, the peak gust has a less significant effect on larger buildings because gusts are typically not well correlated over the different parts of the structure (NRCC, 2015). Therefore, the NBCC advises that the product of the longer term average wind pressure, $q_{A1,50}$, and the gust effect factor, C_g (see eq. 1.4), should be used to account for the effects of wind gusts on larger buildings (NRCC, 2015). Note that the peak gust speed should still be considered when designing smaller components of large buildings, such as individual windows, as small components will almost certainly be enveloped by wind gusts.

Both the longer term average design wind speed and peak gust speed are estimated based on wind speed measurements of specific averaging durations. This subsection discusses the impact these averaging durations have on estimates of the distributions of $V_W(t)$ and $U(t)$. Figure 1.2 illustrates how the duration of the averaging period can affect estimates of wind speed mean and variance.

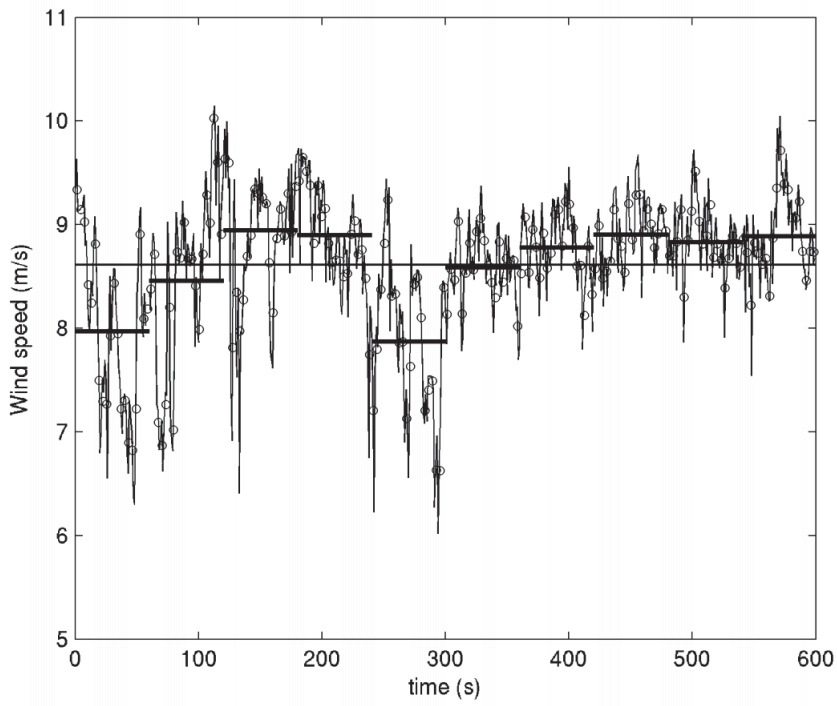

Figure 1.2: Different measures of the average wind speed (Harper et al., 2010). Note that shorter averaging lengths lead to more variability in the averages, but that the overall mean is constant.

Figure 1.2 shows ten minutes of wind speed data, where the thin curve is the 1 sec average wind speed, the open circles are the 3 sec average wind speeds, thick horizontal bars are the 1 min average wind speeds and the thin horizontal bar is the ten min average wind speed (Harper et al., 2010). The figure demonstrates that shorter averaging lengths better represent wind speed variability, while longer averaging lengths lead to closer estimates of the true mean with lower variability. Consequently, shorter averaging periods, typically 3 sec, are useful for determining the peak gust (i.e., the maximum 3 sec average within a period), while longer averages should be used to estimate the mean.

To estimate the mean wind speed, the World Meteorological Organization recommends using "the longest practical interval that can be regarded as stationary", which is generally the ten min average (Harper et al., 2010). However, a one hour average is used in the NBCC. A one hour average is used because hourly averaged wind data were recorded historically (i.e., the mileage of wind passing through the

anemometer over the entire hour). Although most stations now record shorter duration averages at the top of every hour (Hong et al., 2014*a*), the NBCC has maintained historical methods by adjusting the more recent one, two or ten minute average wind speed measurements to be equivalent to the expected one hour average (Hong et al., 2014*a*). Note that when estimating the mean, any averaging duration is an unbiased estimate of the mean as long as the measurement is a random sample (Harper et al., 2010). For example, the ten one min average wind speed measurements shown in Fig. 1.2 are unbiased estimates of the ten min average, meaning they are all equally valid. However, these shorter duration averages are likely to be higher or lower than the true ten min average due to a higher variance. Therefore, shorter duration averages are less reliable (Harper et al., 2010), unless more short duration averages are averaged.

Wind speed data recorded at six aviation stations in southern Ontario are analysed to further demonstrate how estimates of wind speed mean and variance change with averaging duration. The NAV CANADA - TO2015 Pan and Parapan American Games dataset, published by Environment and Climate Change Canada (ECCC), is used for this analysis. The dataset contains two min average wind speed measurements from May 25 to August 31, 2015, recorded in Sarnia, Kitchener/Waterloo, Oshawa, Toronto City Center, Peterborough and Muskoka. The Peterborough and Muskoka station data are not used for this analysis because they are missing 18% and 9% of data, respectively. The remaining four stations are each missing between 4% and 6% of the two min average wind speed measurements, and the missing data points are randomly spaced throughout the 3 months. For this analysis, these missing data are ignored, and all data points at each station are assessed as one continuous time series. To determine the average wind speed for durations longer than two minutes, the average of consecutive two min average values is taken (i.e., 3 consecutive two min average wind speed measurements are used to determine the six min average). Figure 1.3 shows the sample mean and variance of the wind speed measurements at Toronto City Centre Airport for the T-average wind speed, $V_T(t)$, for averaging durations $2 \leq T \leq 240$ min (i.e., $\hat{\mu}_{V_T}$ and $\hat{\sigma}^2_{V_T}$, respectively).

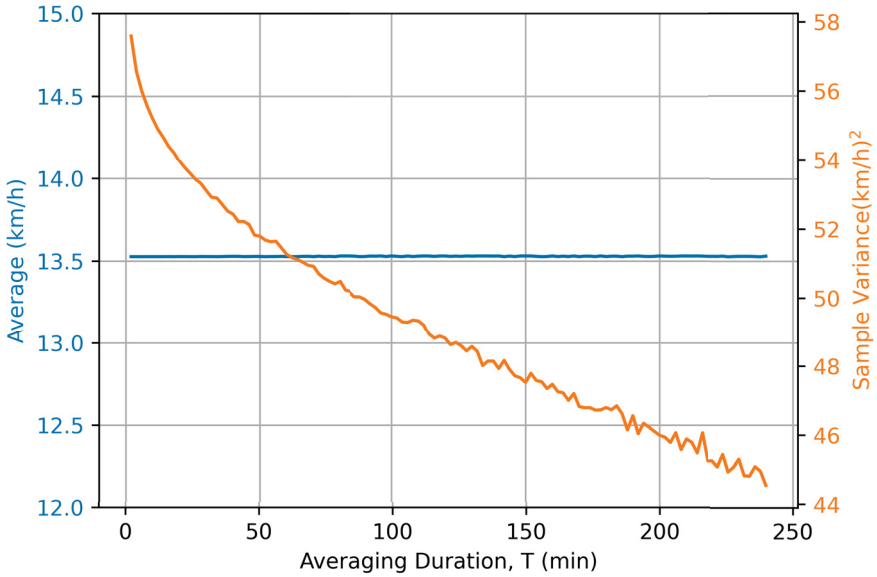

Figure 1.3: Average and sample variance of the wind speed measurements at Toronto City Centre Airport for averaging durations from 2 to 240 min.

As expected, Fig. 1.3 shows averaging length has no affect on the average of averages, while the sample variance decreases with longer duration averages. The results for the other three locations, not shown here, are similar to Fig. 1.3. The average is constant with averaging duration at all locations, although the shape and magnitude of the sample variance reduction curve changes slightly by location (see Fig. 1.4). The average is constant because all two min wind speed measurements within the observation period are used to calculate the average for each averaging duration. For example, the average at an averaging duration of six min uses all six min wind speed averages, which were each determined as the average of three consecutive two min averages. The figure demonstrates that any averaging duration is an equally valid estimate of the mean when averaged over the entire sample duration, but longer averaging durations have a lower variance. Consequently, wind speed measurements averaged over even longer durations are more likely to be closer to the true mean.

The amount that the variance of a stochastic process decreases due to averaging over duration T can be described by the so-called variance reduction function, $\gamma(T)$. The variance reduction function is equal to 1.0 at $T = 0$, and decreases towards zero as T increases. The variance of wind speed measurements at averaging duration T

can therefore be defined in terms of the variance reduction function as

$$\sigma^2_{V_T} = \sigma^2_V \gamma(T) \tag{1.14}$$

where σ^2_V is the variance of the instantaneous wind speed (i.e., at $T = 0$). The variance reduction function is defined as

$$\gamma(T) = \frac{1}{T^2} \int_0^T \int_0^T \rho(t_2 - t_1) dt_2 dt_1 \tag{1.15}$$

where $\rho(\tau)$ is the correlation function. Equation (1.15) demonstrates that the variance reduction function is the average correlation coefficient between every pair of points in the interval [0,T] (Fenton and Griffiths, 2008). If the correlation between points decreases rapidly with distance, the variance reduction function will also decrease. Conversely, if all points in the interval [0,T] are highly correlated $\gamma(T)$ will be close to 1.0. Note that $\gamma(T) = 1.0$ corresponds to perfect correlation (Fenton and Griffiths, 2008).

Second-moment behaviour can be represented by two types of covariance models: finite-scale stochastic models and fractal models (Fenton, 1999). Finite-scale stochastic models have limited correlation lengths and are considered short-memory models. In contrast, fractal models have significant correlation over very large durations and are considered long-memory models (Fenton, 1999). One of the most commonly used finite-scale models in engineering practice is the 1D Markov model. The popularity of the Markov process is due to its simplicity, as the "future" of the process is only dependant on the "present" and not the entire past history (Fenton and Griffiths, 2008). The Markov process has an exponentially decaying correlation function given as

$$\rho(\tau) = \exp\left(-\frac{2|\tau|}{\theta}\right) \tag{1.16}$$

where θ is the correlation length, and τ is the distance between the data points. The correlation length is the distance beyond which data points are largely uncorrelated (i.e., less than about 10%) (Fenton and Griffiths, 2008). The Markov process is considered a finite-scale model because the correlation decays rapidly enough for $\tau > \theta$ that the correlation length remains finite (Fenton, 1999). The variance reduction function of the Markov process is given as

$$\gamma(T) = \frac{\theta^2}{2T^2}\left[\frac{2|T|}{\theta} + \exp\left(-\frac{2|T|}{\theta}\right) - 1\right] \tag{1.17}$$

Fractal models, the second type of covariance model, are also known as statistically self-similar, long-memory, and $1/f$ noise models. Fractal models have an infinite correlation length and thus retain significant correlations even at very large distances (Fenton and Griffiths, 2008). Fractal processes are made up of a sum of successively smaller amplitude, higher frequency sinusoids. Therefore, fractal processes look the same, statistically, as one progressively "zooms" in on the random process, or out (Fenton and Griffiths, 2008). The one-sided spectral density function is often used to describe fractal processes and is given by

$$G(\omega) = \frac{G_O}{\omega^\zeta} \tag{1.18}$$

where ω is a given frequency, ζ defines how the spectral power varies across low and high frequencies, and G_O is the spectral intensity (Fenton and Griffiths, 2008). Fractional Gaussian noise results when $0 \leq \zeta \leq 1$. Fractional Gaussian noise is a stationary process with infinite high frequency spectral power. Fractional Brownian motion results when $\zeta > 1$. Fractional Brownian motion is a non-stationary process that has infinite spectral power in the lower frequencies and decays more rapidly at higher frequencies. Historical wind speeds, as well as future wind speeds over short time periods (e.g., within 1 day) can be considered a stationary process. Therefore, a fractional Gaussian noise model should be used for wind speeds. However, in practice neither fractional Gaussian noise nor fractional Brownian motion is physically realizable because variance cannot be infinite. Consequently, the spectral density function must be truncated such that the fractal process has a finite variance. Mandelbrot and Van Ness (1968) showed that by locally averaging over some distance δ, fractional Gaussian noise becomes physically realizable since local averaging damps out high frequency sinusoids, effectively truncating the spectral density function at the high end (Fenton, 1999). Mandelbrot and Van Ness (1968) determined the resulting correlation function to be

$$\rho(\tau) = \frac{1}{2\delta^{2H}} \left[|\tau + \delta|^{2H} - 2|\tau|^{2H} + |\tau - \delta|^{2H} \right] \tag{1.19}$$

where $H = \frac{1}{2}(\zeta+1)$ is the Hurst coefficient. The Hurst coefficient must be in the range $\frac{1}{2} \leq H \leq 1$, where $H = \frac{1}{2}$ corresponds to white noise, and $H = 1$ corresponds to perfect correlation (Fenton and Griffiths, 2008). The corresponding variance reduction

function of fractional Gaussian noise is (Fenton and Griffiths, 2008)

$$\gamma(T) = \frac{|T+\delta|^{2H+2} - |T|^{2H+2} + |T-\delta|^{2H+2} - 2\delta^{2H+2}}{T^2(2H+1)(2H+2)\delta^{2H}} \tag{1.20}$$

Note that local averaging causes eq. (1.20) to be only an approximation of fractional Gaussian noise, where the accuracy improves as δ approaches 0 (although the variance increases without limit).

Both the Markov and fractional Gaussian noise variance reduction functions were used to fit eq. (1.14) to the empirical wind speed variance for each location (e.g., the variance reduction curve shown in Fig. 1.3). The best-fit correlation length, θ, for the Markov process variance reduction function was found by minimizing the sum of squared errors (SSE) between the given Markov variance reduction function and the wind data variance. Similarly, for the fractal process, δ and H were estimated simultaneously as the values at which the SSE was minimized. The following steps were used to estimate σ_V^2 and the variance reduction function parameters (i.e., θ, δ and H):

1. The empirical variance reduction curve was normalized, such that $\overline{\hat{\sigma}^2_{V_T}} = \frac{\hat{\sigma}^2_{V_T}}{\hat{\sigma}^2_{V_2\ \min}}$, where $\hat{\sigma}^2_{V_T}$ is the empirical variance reduction curve, and T is the averaging duration

2. Both the Markov and fractal process variance reduction functions were fit to $\overline{\hat{\sigma}^2_{V_T}}$, and the best-fit parameters (i.e., $\overline{\theta}$, $\overline{\delta}$ and $\overline{H}$) were determined based on the SSE, as described above

3. The estimated variance, $\hat{\sigma}_V^2$, was determined for both the Markov and fractal process functions based on eq. (1.14) to be the average of $\frac{\hat{\sigma}^2_{V_T}}{\overline{\gamma}(W)}$ across all averaging durations, T. That is, $\hat{\sigma}_V^2 = \frac{1}{120}\sum_T \frac{\hat{\sigma}^2_{V_T}}{\overline{\gamma}(T)}$ for $T = 2, 4, 6, \ldots 240$. Note that $\overline{\gamma}(T)$ is either the best-fit Markov variance reduction function where $\theta = \overline{\theta}$, or the best-fit fractal process variance reduction function where $\delta = \overline{\delta}$ and $H = \overline{H}$

4. The Markov and fractal process variance reduction functions were then fit to the empirical variance reduction curve, $\hat{\sigma}^2_{V_T}$, using the corresponding estimated variance, $\hat{\sigma}_V^2$, found in step 3. That is, the best-fit parameters (i.e., θ, δ and H) of $\gamma(T)$ were determined based on the SSE between $\hat{\sigma}^2_{V_T}$ and $\hat{\sigma}_V^2\gamma(T)$

The results are shown in Fig. 1.4. The black lines show the empirical variance reduction curve at each location. The best-fit Markov and fractal process variance reduction functions are shown as the blue and orange lines, respectively. The variance reduction function parameters, and the SSE for each function are included in the legend.

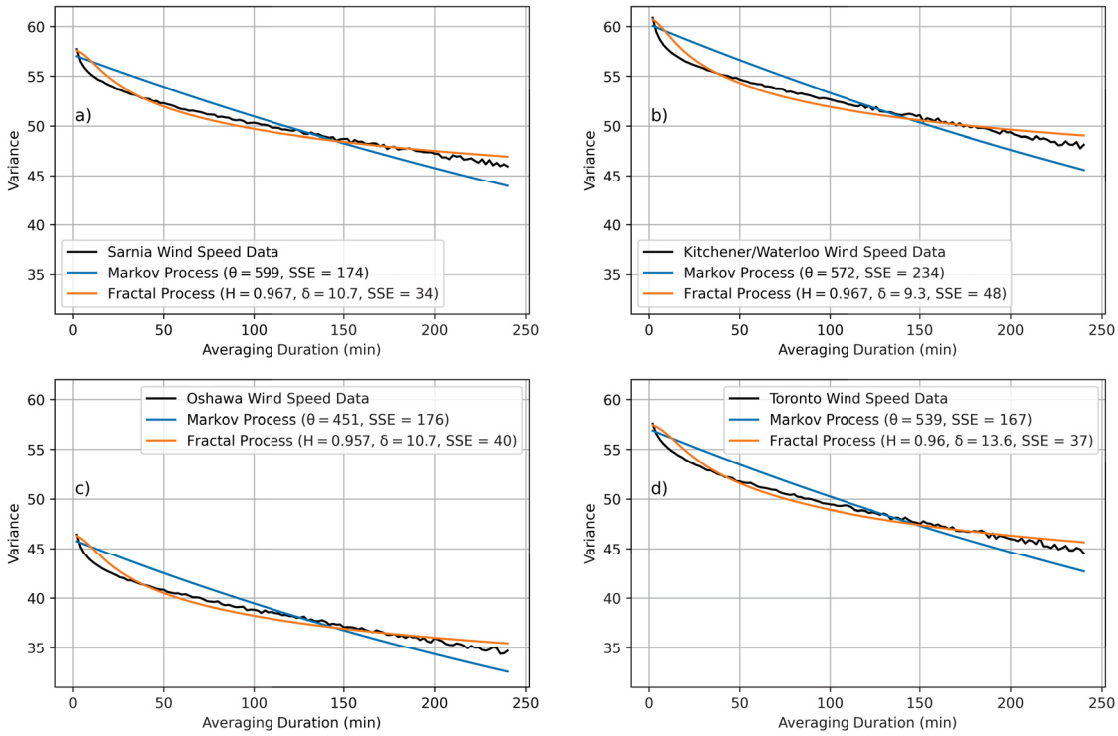

Figure 1.4: Estimate of wind speed variance reduction function using the Markov and fractal process for (a) Sarnia, (b) Kitchener/Waterloo, (c) Oshawa and (d) Toronto City Center.

Figure 1.4 demonstrates that the fractal process provides a significantly better fit to the data for all locations, based on the SSE. The average SSE for the Markov process was 372% higher than that of the fractal process. The results agree with the physical understanding of wind speeds, which is that wind speeds have long-range correlations and, therefore, should be represented by a fractal process (Feng et al., 2009). The average best-fit local averaging distance, δ, is 11.1, while the average best fit Hurst coefficient, H, is 0.963. A fractal process with these "average" coefficients is used as the wind speed variance reduction function in this thesis, and is assumed to be valid across Canada. Note that δ is relatively high for all locations, meaning that the model

is not an accurate approximation of fractional Gaussian noise. However, there is no physical reason to believe that wind speed variance should be represented by true fractional Gaussian noise (especially since wind speeds do not have infinite variance, in practice). Therefore, δ should be selected such that the model best fits the data, rather than constrained close to 0 to more accurately model fractional Gaussian noise.

This analysis of wind speed variance reduction functions also confirms Harper et al.'s (2010) recommendation, which states that the longest averaging duration that can be considered stationary should be used to estimate the mean wind speed since longer averaging durations are more reliable due to their lower variance. However, the importance of this claim, that is, how much the design wind speed changes as a function of averaging duration, should be investigated. As previously discussed a one hour averaging duration is used in the NBCC, while Harper et al. (2010) recommends a ten min average. To evaluate if the averaging duration used in the NBCC should be updated, the value of the design wind speed of longer term averaging duration W, where 2 min $\leq W \leq$ 4 hours, should be compared to the design wind speed with a one hour averaging duration. Let the design wind speed be denoted as

$$v_{AW,m} = \mu_{V_W} + z_m \sigma_{V_W} \tag{1.21}$$

where μ_{V_W} and σ_{V_W} are the mean and standard deviation, respectively, of W-average wind speed measurements over a given observation period, and z_m is the distance from μ_{v_W} to the m-year return period annual maximum W-average wind speed, $v_{AW,m}$, measured in standard deviation units. Given that wind speed is considered to be normally distributed, z_m = the point such that $\Pr[V_W > z_m] = \frac{1}{8760m} = \Phi^{-1}(1 - \frac{1}{8760m})$, since there are 8760 hours per year. Any averaging duration is an unbiased estimate of the mean, therefore, μ_{v_W} is assumed to be constant with respect to the averaging duration, W. This is a valid assumption as long as measurements are taken over a sufficiently long observation period, which is true for the NBCC. The following ratio can then be used to evaluate the effect of averaging duration on the design wind speed

$$\frac{v_{AW,m} - \mu_{v_W}}{v_{A1,m} - \mu_{v_{1\text{ hr}}}} = \frac{z_m \sigma_{V_W}}{z_m \sigma_{V_{1\text{ hr}}}} \tag{1.22}$$

where $v_{A1,m}$ is the m-year return period annual maximum one-hourly average wind

speed. Using eq. (1.21) and eq. (1.14), eq. (1.22) can be equivalently written as

$$\frac{z_m \sigma_{V_W}}{z_m \sigma_{V_{1\text{ hr}}}} = \frac{\sigma_{V_W}}{\sigma_{V_{1\text{ hr}}}} = \sqrt{\frac{\sigma_V^2 \gamma(W)}{\sigma_V^2 \gamma(1\text{ hr})}} = \sqrt{\frac{\gamma(W)}{\gamma(1\text{ hr})}} \tag{1.23}$$

Equation (1.23) demonstrates that the design wind speed ratio is only dependant on the shape of the variance reduction function, $\gamma(W)$, and not on the magnitude of the instantaneous wind speed variance, σ_V^2. The variance reduction functions of the four southern Ontario stations, shown in Fig. 1.4, as well as the average fractal process, are used to evaluate eq. (1.23). The results are shown in Fig. 1.5(a) and (b). Figure 1.5(b) has narrowed the vertical scale to more clearly illustrate the differences between locations.

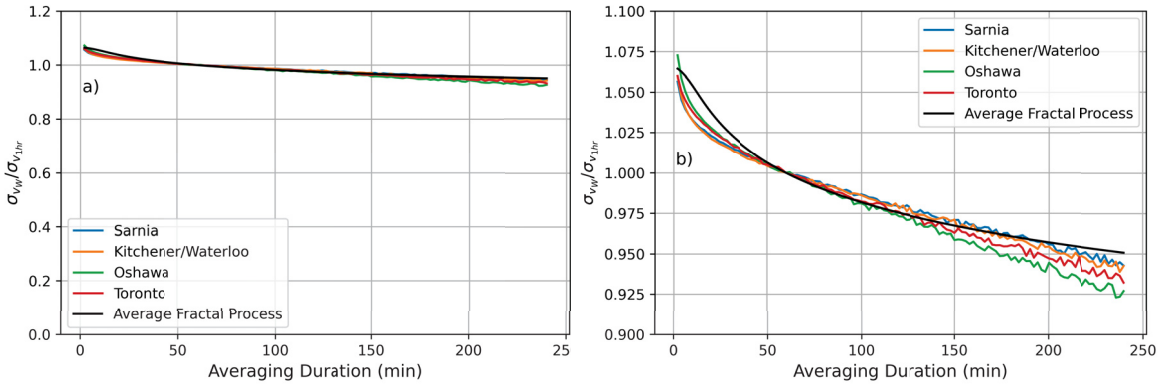

Figure 1.5: Effect of averaging duration on the ratio of W-average design wind speed residual to the one hour average design wind speed residual (eq. 1.22) with y-axis scaled from (a) 0 to 1.2 and (b) 0.9 to 1.1.

Figure 1.5 demonstrates that averaging duration does not have a large effect on the design wind speed. The average design wind speed ratio for the ten min average design wind speed relative to the one hour design wind speed for the four locations is 1.036, while the maximum ratio is 1.041 for Oshawa. The ratio of $\frac{v_{AW,m}}{v_{A1,m}}$ is actually of more interest since it gives a direct relationship from which design wind speeds for any averaging length can be determined. The ratio shown in Fig. 1.5 is not exactly equal to $\frac{v_{AW,m}}{v_{A1,m}}$. However, since the product of z_m and σ_{V_W} is large relative to the mean speed, μ_{V_W}, the ratio $\frac{v_{AW,m} - \mu_{v_W}}{v_{A1,m} - \mu_{v_{1\text{ hr}}}}$, shown in Fig. 1.5 is a reasonable and conservative estimate of $\frac{v_{AW,m}}{v_{A1,m}}$. For example, using the average instantaneous wind speed mean and standard deviation across the four locations, $\mu_V = 11.69\,\text{km}\,\text{h}^{-1}$ and

$\sigma_V = 7.48\,\mathrm{km\,h^{-1}}$, respectively, the average ratio of the ten min and one hour 50-year design winds speed without their means subtracted is

$$\frac{v_{A10\ \mathrm{min},50}}{v_{A1,50}} = \frac{7.48 + (4.584)(11.69)(1.036)}{7.48 + (4.584)(11.69)} = 1.032 \tag{1.24}$$

Therefore, the ten min average design wind speed is only 3.2% greater than the one hour design wind speed in southern Ontario, while Fig. 1.5 shows a ratio of 1.036. Figure 1.5(b) also demonstrates that the best-fit fractal process slightly overestimates the increase in the design wind speed due to averaging, especially for lower averaging durations. The design wind speed ratio of the ten min average relative to the one hour average for the fractal process is 1.054. In either case, this small discrepancy is considered to be negligible, and the one hour average wind speed is considered satisfactory for use in the NBCC. This conclusion is also supported by Hong et al. (2014*a*), who found that annual maximum one or two minute wind speed averages are valid estimates of the annual maximum one-hourly average wind speed.

For the design of small buildings, or building components such as windows, the peak gust must also be considered in addition to the m-year return period design wind speed. Most major structural design codes, including the NBCC, use the "gust factor" approach to estimate wind loads. The gust factor approach estimates the peak gust wind speed as the product of the W-averaged m-year return period design wind speed, $v_{AW,m}$, and a gust factor, G. The gust factor, G, is not to be confused with the gust effect factor, C_g, used in the NBCC (see eq. 1.4). The gust factor, G, is applied to wind speed, while the gust effect factor, C_g, is applied to wind pressure which is equal to wind speed squared. Therefore, $G = \sqrt{C_g}$.

The gust factor, G, is a function of the averaging duration used for the short-term gust wind speed, w, and the longer time period, W, which the design wind speed is averaged over. Durst (1960) first proposed the gust factor curve, which provides an estimate of the relationship between the peak gust wind speed averaged over w, and the one-hourly average wind speed (i.e., V_W where $W = 1$ hr). To develop the curve, Durst (1960) assumed that short-term averaged gust wind speeds are independent of each other and normally distributed about the longer term average wind speed (as reported by Miller, 2011). The estimated w-average peak gust wind speed is then given by (Miller, 2011)

$$\hat{v}_w = \mu_{V_W} + g(w, W)\sigma_u(w, W) \tag{1.25}$$

where $\hat{v}_w$ is a statistical measure of the w-averaged peak gust wind speed, μ_{V_W} is the mean of $V_W(t)$, $g(w, W)$ is the peak factor which is a function of w and W, and $\sigma_u(w, W)$ is the standard deviation of the gust fluctuations (i.e., the unsteady component $U(t)$). Dividing eq. (1.25) by v_W gives the gust factor, G, as

$$G(w, W) = 1 + g(w, W)\frac{\sigma_u(w, W)}{\mu_{V_W}} \tag{1.26}$$

Durst (1960) determined the variances, $\sigma_u(w, W)$, and averages, v_W, based on data from Giblett (1932), which contains 5 sec average wind speed data taken over observational periods of up to ten min. Durst (1960) defined the peak factor, $g(w, W)$, as the value of the standard normal distribution with a cumulative probability equal to $1-w/W$. For example, for $w = 3$ sec and $W = 3600$ sec, $g(w, W) = \Phi^{-1}(1-3/3600) = 3.142$.

The gust factor estimates developed by Durst (1960) are still commonly used today for non-hurricane winds. Krayer and Marshall (1992) developed an updated curve for hurricane winds, as they were found to have higher gust factors than extratropical storms. Krayer and Marshall's (1992) results were used to update the wind speed map in the ASCE-7-95 (Vickery and Skerlj, 2005). Krayer and Marshall (1992) determined the hurricane gust factor curve using data from four separate hurricanes by simply calculating the gust factor as

$$G(w, W) = \frac{1}{N}\sum_{i=1}^{N} \hat{v}_{w,i}/v_{W,i} \tag{1.27}$$

where $\hat{v}_{w,i}$ is the maximum w-averaged gust speed, $v_{W,i}$ is the corresponding longer term W-averaged wind speed, and N is the number of observations. Durst (1960) found that the gust factor for $w = 3$ sec and $W = 1$ hour is approximately 1.53, while that proposed by Krayer and Marshall (1992) is approximately 1.67. In comparison, the NBCC has adopted a gust effect factor, C_g, of "2.0 for the *building* as a whole and main structural members, or 2.5 for external pressures and suctions on secondary members, including cladding" (NRCC, 2015). Note that $C_g = 2.0$ correponds to a gust factor, G, of $\sqrt{2.0} \approx 1.41$, and $C_g = 2.5$ corresponds to $G = \sqrt{2.5} \approx 1.58$. The

NBCC gust factor (i.e., $G = 1.41$ for main strucutural members) is lower than that found by Durst (1960) (i.e., $G = 1.53$) because the gust factor found by Durst (1960) estimates the peak gust, while the NBCC gust factor is intended for the design of larger buildings, which are not affected by the peak gust (NRCC, 2015). Additionally, the NBCC used averaging durations of approximately 3 to 7 seconds to evaluate the peak gust (NRCC, 2015). At $w = 7$ sec and $W = 1$ hour, Durst (1960) found $G = 1.46$, which is closer to the NBCC gust factor ($G = 1.41$). The NBCC does not state the gust factor that should be used for the peak gust.

The gust factor, G, can also be derived analytically based on the variance reduction function results described above, as $\sigma_u(w, W)$ and μ_{V_W} are the only unknown values in the gust factor equation defined by Durst (1960) (see eq. 1.26). Let the longer term W-averaged wind speed and the short-term w-averaged wind speed be random variables, $V_W(t)$, and $V_w(t)$, respectively. These two wind speeds can be then be written in terms of their first and second moments as $V_w(t) = \mu_{V_w} + \sigma_{V_w} Y_w(t)$ and $V_W(t) = \mu_{V_W} + \sigma_{V_W} Y_W(t)$ where $Y_w(t), Y_W(t) \sim N(0, 1)$ and may be cross-correlated. Gust fluctuations can then be defined as $U(t) = V_w(t) - V_W(t)$, where $U(t)$ is instantaneous as $w \to 0$. The variance of $U(t)$ is then

$$\begin{aligned} \sigma_u^2(w, W) &= \mathrm{Var}[U(t)] \\ &= \mathrm{Var}[V_w(t) - V_W(t)] \\ &= \mathrm{Var}[(\mu_{V_w} + \sigma_{V_w} Y_w(t)) - (\mu_{V_W} + \sigma_{V_W} Y_W(t))] \end{aligned} \tag{1.28}$$

Since the mean wind speed is independent of averaging duration, as demonstrated in Fig. 1.3, it can be assumed that the mean wind speed of any averaging duration, i, μ_{V_i}, can be written as μ_V, which is the mean of the instantaneous wind speed. That is, $\mu_{V_w} = \mu_{V_W} = \mu_V$. Consequently, eq. (1.28) becomes

$$\begin{aligned} \sigma_u^2(w, W) &= \mathrm{Var}[\sigma_{V_w} Y_w(t) - \sigma_{V_W} Y_W(t)] \\ &= \sigma_{V_w}^2 \mathrm{Var}[Y_w(t)] + \sigma_{V_W}^2 \mathrm{Var}[Y_W(t)] - 2\sigma_{V_w}\sigma_{V_W}\mathrm{Cov}(Y_w, Y_W) \\ &= \sigma_{V_w}^2 + \sigma_{V_W}^2 - 2\sigma_{V_w}\sigma_{V_W}\mathrm{Cov}(Y_w, Y_W) \\ &= \sigma_V^2 \left[\gamma(w) + \gamma(W) - 2\sqrt{\gamma(w)\gamma(W)}\mathrm{Cov}(Y_w, Y_W)\right] \end{aligned} \tag{1.29}$$

where $\mathrm{Cov}(Y_w, Y_W)$ is the covariance between $Y_w(t)$ and $Y_W(t)$. Using the result of

eq. (1.29), the gust factor is then

$$\begin{aligned} G(w,W) &= 1 + g(w,W)\frac{\sqrt{\sigma_V^2\left[\gamma(w)+\gamma(W)-2\sqrt{\gamma(w)\gamma(W)}\mathrm{Cov}(Y_w,Y_W)\right]}}{\mu_{V_W}} \\ &= 1 + g(w,W)\frac{\sigma_V}{\mu_{V_W}}\sqrt{\gamma(w)+\gamma(W)-2\sqrt{\gamma(w)\gamma(W)}\mathrm{Cov}(Y_w,Y_W)} \\ &= 1 + g(w,W)\frac{\sigma_V}{\mu_V}\sqrt{\gamma(w)+\gamma(W)-2\sqrt{\gamma(w)\gamma(W)}\mathrm{Cov}(Y_w,Y_W)} \\ &= 1 + g(w,W)\mathrm{CV}_V\sqrt{\gamma(w)+\gamma(W)-2\sqrt{\gamma(w)\gamma(W)}\mathrm{Cov}(Y_w,Y_W)} \end{aligned} \tag{1.30}$$

where CV_V is the wind speed coefficient of variation.

The covariance, $\mathrm{Cov}(Y_w, Y_W)$, can be determined both analytically and empirically. The covariance, $\mathrm{Cov}(Y_w, Y_W)$, is found empirically by calculating the Pearson correlation coefficient using wind speed data from the NAV CANADA - TO2015 Pan and Parapan American Games dataset. While, $\mathrm{Cov}(Y_w, Y_W)$ is solved analytically based on the variance reduction function, $\gamma(T)$. First, $\mathrm{Cov}(Y_w, Y_W)$ is defined in terms of the covariance between the short-term w-averaged wind speed and the longer term W-averaged wind speed, $\mathrm{Cov}(V_w, V_W)$, as

$$\begin{aligned} \mathrm{Cov}(V_w,V_W) &= \mathrm{Cov}\left(\mu_{V_w}+\sigma_{V_w}Y_w(t), \mu_{V_W}+\sigma_{V_W}Y_W(t)\right) \\ &= \mathrm{Cov}\left(\sigma_{V_w}Y_w(t), \sigma_{V_W}Y_W(t)\right) \\ &= \sigma_{V_w}\sigma_{V_W}\mathrm{Cov}(Y_w,Y_W) \\ &= \sigma_V^2\sqrt{\gamma(w)\gamma(W)}\mathrm{Cov}((Y_w,Y_W) \end{aligned} \tag{1.31}$$

Therefore, $\mathrm{Cov}(Y_w, Y_W)$ is

$$\mathrm{Cov}(Y_w,Y_W) = \frac{\mathrm{Cov}(V_w,V_W)}{\sigma_V^2\sqrt{\gamma(w)\gamma(W)}} \tag{1.32}$$

The covariance, $\mathrm{Cov}(V_w, V_W)$, is then defined in terms of the correlation function corresponding to the average fractal process variance reduction function (see eq. 1.19)

$$\mathrm{Cov}(V_w,V_W) = \frac{\sigma_V^2}{wW}\int_0^w\int_0^W \rho(t_2-t_1)dt_2dt_1 \tag{1.33}$$

where $\rho(\tau)$ has the same parameters values as those of $\gamma(T)$ (i.e., $\delta = 11.1$ and $H = 0.963$). Substituting eq. (1.33) into eq. (1.32) gives the following analytical result for $\mathrm{Cov}(Y_w, Y_W)$

$$\mathrm{Cov}(Y_w,Y_W) = \frac{1}{wW\sqrt{\gamma(w)\gamma(W)}}\int_0^w\int_0^W \rho(t_2-t_1)dt_2dt_1 \tag{1.34}$$

For this thesis, $\mathrm{Cov}(Y_w, Y_W)$ is calculated for the range 0 min$< w \leq 60$ min with $W = 60$ min, hereinafter $\mathrm{Cov}(Y_w, Y_{1\text{ hr}})$, because the gust factor curve developed by Durst (1960) uses these same parameters, allowing for comparison. Note that the shortest averaging duration available in the dataset is two minutes. Consequently, the empirical results are not available for gust averaging durations less than $w = 2$ min. Figures 1.6(a) and (b) show the empirical and analytical results for $\mathrm{Cov}(Y_w, Y_{1\text{ hr}})$, where the integral in eq. (1.34) was solved numerically. The vertical scale is reduced in Fig. 1.6(b) to more clearly show the discrepancy between the results.

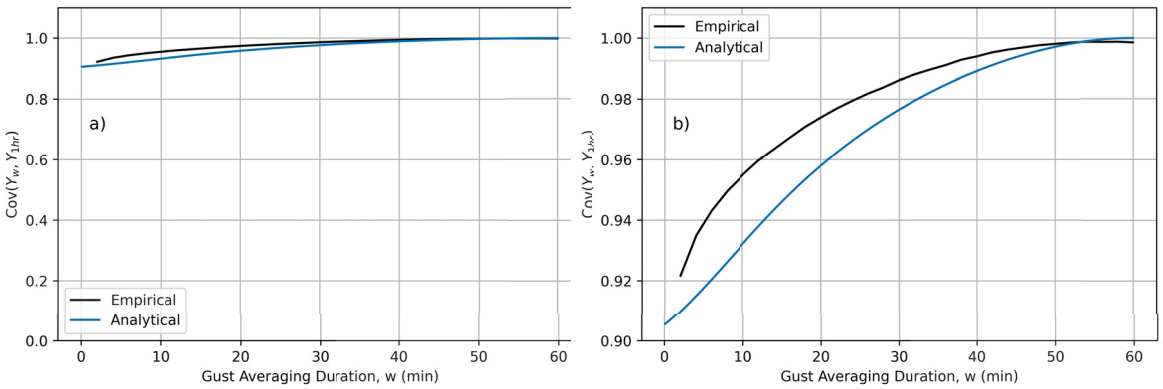

Figure 1.6: Analytical and empirical results for $\mathrm{Cov}(Y_w, Y_{1\text{ hr}})$ determined using eq. (1.34) and the average Pearson correlation coefficient across the four meteorological stations, respectively, with the vertical scale from (a) 0 to 1.1 and (b) 0.90 to 1.01

Figure 1.6 shows that $\mathrm{Cov}(Y_w, Y_{1\text{ hr}})$ approaches 1, as w approaches one hour in both the analytical and empirical cases. This is expected as the two time series (i.e., $V_w(t)$ and $V_W(t)$) are identical when averaged over the same duration, resulting in perfect correlation. Figure 1.6 also demonstrates that the results of the empirical and analytical solutions are very close, although, the analytical $\mathrm{Cov}(Y_w, Y_{1\text{ hr}})$ is slightly lower at shorter gust averaging durations. The analytical solution is used in this thesis, because it can be extended to gust averaging durations less than two min, and it is relatively consistent with the empirical result. This covariance function (i.e., eq. 1.34) can then be used to calculate the gust factor given in eq. (**??**). Meaning, G can be solved analytically based only on the parameters $g(w, W)$, CV_V, and $\gamma(T)$.

The final values required to determine G are the peak factor, $g(w, W)$, and the coefficient of variation, CV_V. The coefficient of variation was determined empirically, as the average CV_V across the four locations in the dataset, and was found to be

0.64. While, $g(w, W) = \Phi^{-1}(1 - w/W)$, which is equivalent to the mode of the $\frac{w}{W}$-return period extreme value distribution. However, Miller (2011) recommends that the mean of the $\frac{w}{W}$-return period extreme value distribution be used instead. The gust factor curve was determined using both peak factors, and the results are shown in Fig. 1.7. The black line shows the gust factor curve determined by Durst (1960), hereinafter referred to as the "Durst Curve". The orange and blue lines show the analytical results using the mode and mean of the extreme value (EV) distribution, respectively.

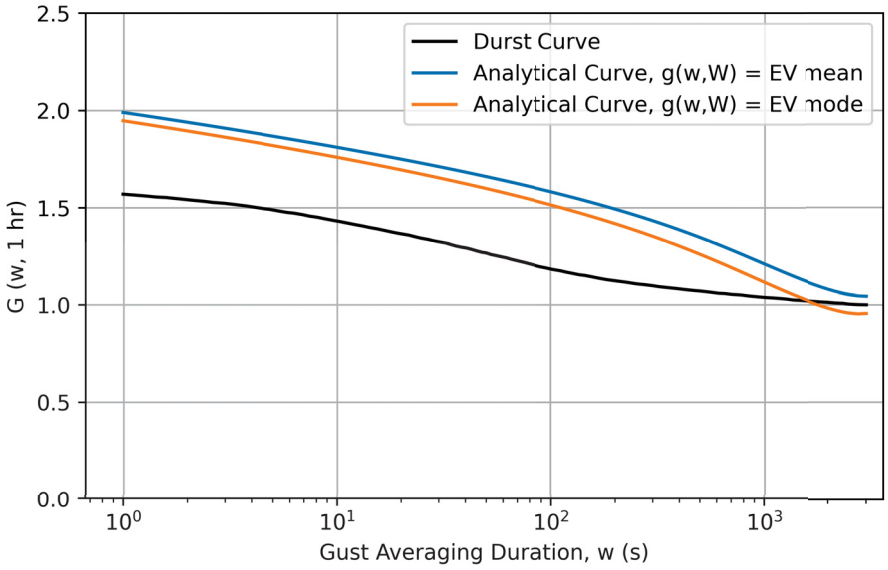

Figure 1.7: Comparison of the gust factor curves determined analytically and that determined by Durst (1960).

Figure 1.7 shows that the analytical gust factor curve determined using eq. (**??**) is significantly higher than the Durst Curve, particularly at lower gust averaging durations. For example, at $w = 3$ sec the analytical gust factor using the EV mode to determine $g(w, W)$ is 22% higher than that found by Durst (1960) (i.e., 1.86 compared to 1.53). These higher analytical gust factor values are caused by a higher value of CV_V (see Fig. 1.8), which is likely a result of the difference in the location where the data were recorded, and potentially the time period as well. Durst (1960) used data from the late 1920s recorded at Cardington, Bedforshire, England (as reported by Miller, 2011), while the analytical gust factor curve is based on southern Ontario data recorded almost a century later, in 2015. Figure 1.7 also demonstrates that using the

EV distribution mean to determine the peak factor, $g(w, W)$, results in gust factors 4.8% higher, on average, than those determined based on the EV distribution mode. This is consistant with the results of Miller (2011), who found that using the mode of the EV distribution underestimates the gust factor by 2%, relative to using the mean. The difference between using the mean and the mode is slightly greater in Fig. 1.7 compared to that found by Miller (2011) (i.e., 4.8% vs. 2%) because the CV_V value is also larger. To be conservative, the mean of the EV distribution will be used to determine $g(w, W)$ in this thesis.

Figure 1.8 demonstrates the effect of CV_V and the fractal process parameters (δ and H) on the difference between the analytical gust factor curve and the Durst Curve. The blue line in Fig. 1.8(a) is the analytical gust factor curve calculated using the empirical results of CV_V, δ and H, which were each determined as the average value across the four locations. This blue gust factor curve is the same as the blue line in Fig. 1.7, and uses the mean of the EV distribution for the peak factor. The dashed orange line in Fig. 1.8(a) uses the best-fit values of CV_V, δ and H, which were determined as the values that minimize the SSE with respect to the Durst Curve. The dashed orange gust factor curve, along with all analytical gust factor curves in Fig. 1.8(b) also use the mean of the EV distribution for the peak factor. The analytical curves in Fig. 1.8(b) use a combination of empirical and best-fit values for CV_V, δ and H. The red line shows the gust factor curve with the best-fit value of CV_V when δ and H are held at their empirical values. Conversely, the green line shows the gust factor curve with the best-fit values of δ and H when CV_V is held at its empirical value.

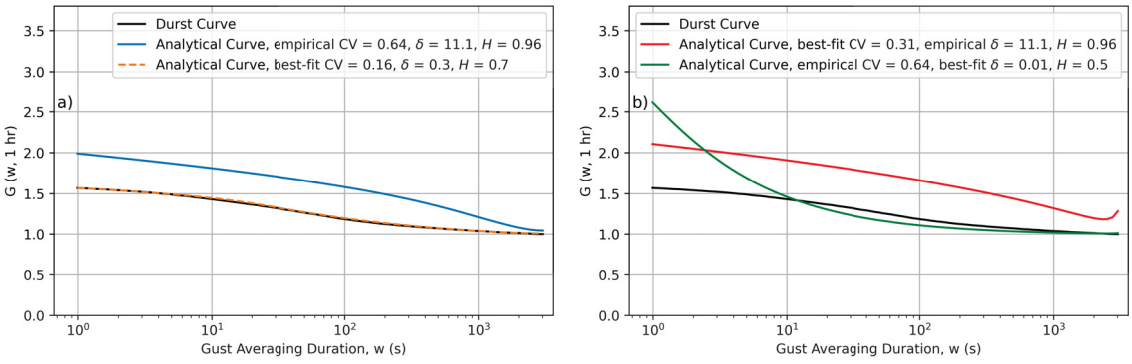

Figure 1.8: Comparison of the gust factor curve determined by Durst (1960) and analytical gust factor curves with varying CV_V, δ and H.

Figure 1.8 shows that the analytical gust factor curve with the best-fit values of CV_V, δ and H is equivalent to the Durst Curve, as the SSE between the Durst Curve and the dashed orange line is 0.00. Note that the SSE between the blue gust factor curve and the Durst Curve is 11.96. Figure 1.8 also demonstrates that the discrepancy between the empirical gust factor curve and the Durst Curve is mainly attributed to a difference in estimations of CV_V. The SSE between the Durst Curve and the red gust factor curve is 1.56, while that for green curve is 6.68. These red and green lines in Fig. 1.8(b) show that by adjusting CV_V the error between the analytical gust factor curve and the Durst Curve is reduced by 87% (from 11.96 to 1.56), while adjusting the fractal process parameters only reduces this same error by 44% (from 11.96 to 6.68).

To confirm the most appropriate value of CV_V for Canada, the empirical value CV_V (0.64) was validated against $\mathrm{CV_v}$ values determined by Hong et al. (2014*b*) using one-hourly average wind speed data from the Environment Canada (EC) HLY01 archive. Hong et al. (2014*b*) calculated the sample mean and standard deviation of the hourly-average wind speed for 14 stations across Canada which each had between 34 and 50 years of data. To determine CV_V based on Hong et al.'s (2014*b*) results, the hourly-average sample mean, $\mu_{V_{1\text{ hr}}}$, and standard deviation, $\sigma_{V_{1\text{ hr}}}$, must first be converted to the corresponding instantaneous values, σ_V and μ_V. Equation (1.14) is used to convert $\sigma_{V_{1\text{ hr}}}$ to σ_V, where $\gamma(1\text{ hr})$ is the value of the average fractal process variance reduction function from Fig. 1.4 at $T = 1$ hr. While, $\mu_V = \mu_{V_{1\text{ hr}}}$ since, as discussed, the sample mean is constant with averaging duration. The instantaneous coefficient of variation, CV_V, can then be written in terms of the one-hourly average wind speed sample mean and standard deviation as

$$\mathrm{CV}_V = \frac{\sigma_V}{\mu_V} = \frac{\sigma_{V_{1\text{ hr}}}}{\mu_{V_{1\text{ hr}}}\sqrt{\gamma(1\text{ hr})}} \tag{1.35}$$

Table 1.1 shows the wind speed statistics for the 14 selected meteorological stations. The data in columns 1 to 5 are from Hong et al. (2014*b*), while columns 6 and 7 are calculated based on eq. (1.14) and eq. (1.35), respectively.

Table 1.1 demonstrates that the empirical CV_V found based on the NAV CANADA - TO2015 Pan and Parapan American Games dataset (0.64) is very close to that for Toronto Int'l A based on the EC HLY01 dataset (0.69). Toronto Int'l A is used here

Location	Province	$\mu_{V_{1\text{ hr}}}$	$\sigma_{V_{1\text{ hr}}}$	$\text{CV}_{V_{1\text{ hr}}}$	σ_V	CV_V
Victoria Int'l A	BC	3.01	2.27	0.75	2.42	0.80
Whitehorse A	YT	3.74	2.85	0.76	3.04	0.81
Yellowknife A	NT	3.79	2.29	0.60	2.44	0.64
Iqaluit A	NU	4.13	3.46	0.84	3.69	0.89
Edmonton Int'l A	AB	3.47	2.39	0.69	2.55	0.73
Regina Int'l A	SK	5.32	3.06	0.58	3.26	0.61
Winnipeg Int'l A	MB	4.93	2.85	0.58	3.04	0.62
Ottawa Int'l A	ON	4.32	2.70	0.62	2.88	0.67
Toronto Int'l A	ON	4.76	3.10	0.65	3.30	0.69
Quebec Int'l A	QC	4.14	2.90	0.70	3.09	0.75
Fredericton A	NB	3.70	2.66	0.72	2.83	0.77
Halifax Int'l A	NS	5.14	2.90	0.56	3.09	0.60
Charlottetown A	PE	5.01	2.74	0.55	2.92	0.58
St. John's A	NL	6.87	3.86	0.56	4.11	0.60

Table 1.1: Wind speed statistics for selected Canadian meteorological stations. Adapted from Hong et al. (2014*b*).

for comparison because all the stations in the NAV CANADA dataset are located in southern Ontario. Table 1.1 also shows that the CV_V for the 14 locations varies between a minimum of 0.58 for Charlottetown A, and a maximum of 0.89 for Iqaluit A. The resulting variation in the gust factor between these locations caused by the difference in CV_V values is shown in Fig. 1.9. Note that Fig. 1.9 uses the EV distribution mean to determine $g(t, T)$, and assumes the variance reduction function is constant across locations.

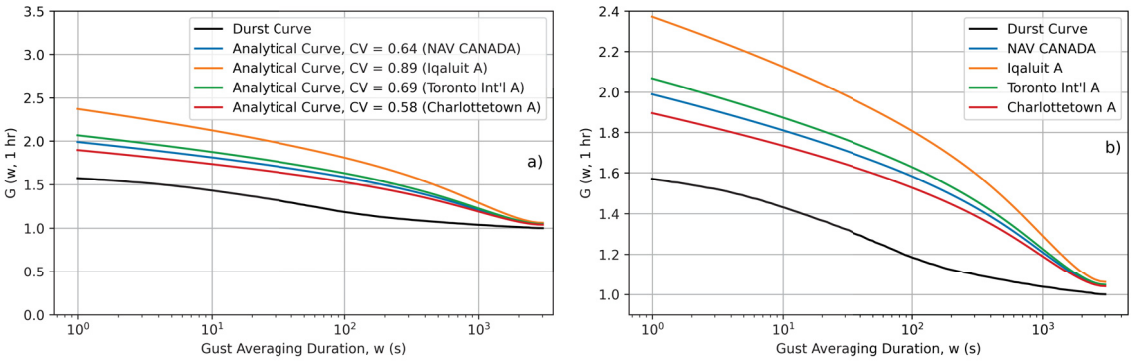

Figure 1.9: Comparison of analytical gust factor curves for various locations across Canada due to varying CV_V, shown in Table 1.1, with the vertical scale from (a) 0 to 3.5 and (b) 0.90 to 1.01

Figure 1.9 demonstrates that the gust factor varies significantly between locations. For example, $G(w = 3 \text{ sec}, W = 1 \text{ hour}) = 1.82$ for Charlottetown A, $G(w = 3 \text{ sec}, W = 1 \text{ hr}) = 1.98$ for Toronto Int'l A, and $G(w = 3 \text{ sec}, W = 1 \text{ hr}) = 2.26$ for Iqaluit A. While it is unclear how the values C_g currently used in the NBCC were determined, these results suggest that C_g may need to be updated in the NBCC to account for the higher wind speed variability levels in Canada than those estimated by Durst (1960). Additionally, the results demonstrate that the NBCC gust effect factor should vary by location to achieve consistent exceedance probabilities in cities such as Victoria, BC, Whitehorse, YT and Iqualuit, NU, that have high CV_V values relative to the rest of Canada.

Alternative models to that in eq. (**??**) above can also be developed based on slightly different assumptions. One modification is to assume that the longer term averaging duration value, $V_W(t)$, is not a random variable, and is instead, constant. That is, $V_W(t) = \mu_{v_W}$, or in other words, changes in longer term average wind speed are negligible. This assumption changes the variance of $U(t)$ to be defined as

$$\begin{aligned}
\sigma_u^2(w, W) &= \text{Var}[U(t)] \\
&= \text{Var}[V_w(t) - V_W(t)] \\
&= \text{Var}[(\mu_{V_w} + \sigma_{V_w} Y_w(t)) - \mu_{V_W}] \\
&= \text{Var}[\sigma_{V_w} Y_w(t)] \\
&= \sigma_{V_w}^2 \text{Var}[Y_w(t)] \\
&= \sigma_V^2 \gamma(w)
\end{aligned} \tag{1.36}$$

The second modification is to assume that $V_w(t)$ and $V_W(t)$ are independent. It is unlikely this assumption is true since the covariance results showed that $\text{Cov}(Y_w, Y_{1 \text{ hr}})$ is greater than 0.90 for $w > 0.1$ seconds. Regardless, it was tested as the variance of

$U(t)$ would change to

$$\begin{aligned}
\sigma_u^2(w,W) &= \mathrm{Var}[U(t)] \\
&= \mathrm{Var}[V_w(t) - V_W(t)] \\
&= \mathrm{Var}[(\mu_{V_w} + \sigma_{V_w} Y_w(t)) - (\mu_{V_W} + \sigma_{V_W} Y_W(t))] \\
&= \mathrm{Var}[\sigma_{V_w} Y_w(t) - \sigma_{V_W} Y_W(t)] \\
&= \sigma_{V_w}^2 \mathrm{Var}[Y_w(t)] + \sigma_{V_W}^2 \mathrm{Var}[Y_W(t)] - 0 \\
&= \sigma_V^2[\gamma(w) + \gamma(W)]
\end{aligned} \tag{1.37}$$

The results of the analytical gust factor curve using these two modified cases are compared to the original analytical gust factor curve (eq. **??**) to validate that the assumptions of the original analytical gust factor curve are correct. Figure 1.10 shows the Durst Curve, the original analytical gust factor curve, as well as the two modified analytical cuves. Note all analytical curves in Fig. 1.10 use the mean of the EV distribution to determine the peak factor.

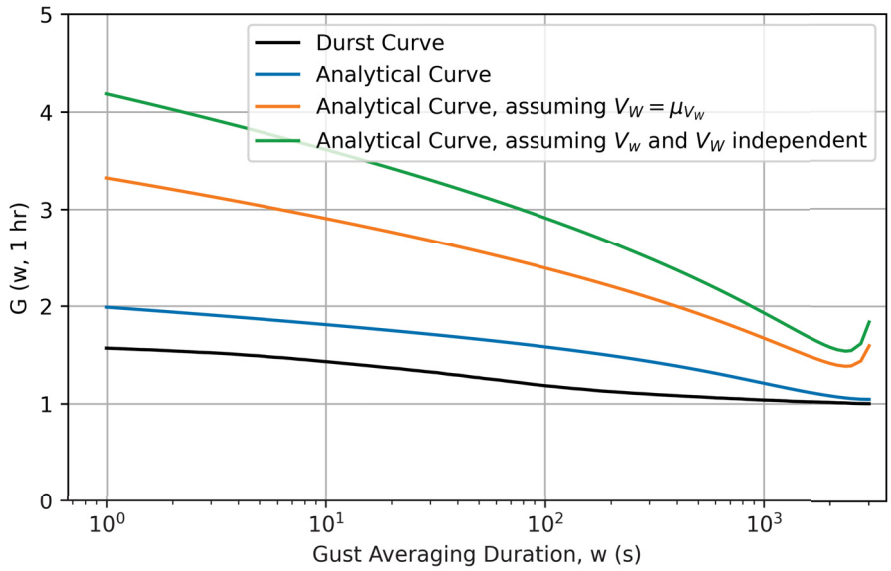

Figure 1.10: Comparison of the gust factor curve determined by Durst (1960) and analytical gust factor curves assuming $V_w(t)$ and $V_W(t)$ are independent, and assuming $V_W(t) = \mu_{V_W}$.

Figure 1.10 demonstrates that these two alternative models significantly overestimate the gust factor. For example, assuming $V_W(t) = \mu_{V_W}$, $G(w = 3\,\mathrm{sec}, W = 1\,\mathrm{hr}) = 3.14$, which is 64% higher than the original analytical curve ($G(w = 3\,\mathrm{sec}, W = 1\,\mathrm{hr}) = 1.91$

for the blue curve). Additionally, if $V_w(t)$ and $V_W(t)$ are assumed to be independent $G(w = 3 \text{ sec}, W = 1 \text{ hr}) = 3.92$, a 106% increase relative to the original analytical curve. The alternative models overestimate the gust factor because they neglect the variability in $V_W(t)$, and the correlation between $V_W(t)$ and $V_w(t)$. The variability in $V_W(t)$ and the correlation between $V_W(t)$ and $V_w(t)$ cause the peak gust to occur while the value of $V_W(t)$ is also relatively high, reducing the value of the gust factor (or increasing the gust factor when neglected). Therefore, Fig. 1.10 confirms that the original analytical gust factor curve (eq. **??**) is the most appropriate model for determining the gust factor.

1.4 Effect of Climate Change on Statistical Modelling of Extreme Wind Speeds

As mentioned above, a key assumption of both extreme value theory and return period values is that extreme wind speed distributions are stationary. Additionally, the gust factor is also defined under the assumption that the short- and long-term averaged wind speed, $V_t(t)$ and $V_T(t)$, respectively, are stationary stochastic processes. However, these assumptions may not remain true as human activity causes changes to the global climate. Climate change will probably affect wind speed distributions in the future, such that they are no longer stationary. Consequently, the current methods for determining the 50-year return period design wind speed, $v_{A1,50}$, may no longer satisfy structural reliability standards. For future building code development, it is important to assess the potential effects of non-stationarity on extreme wind speed distributions and return period, as well as the effect of changes in CV_V on the gust factor. Note that in this study, it is assumed that climate change will not significantly change the variance reduction function, $\gamma(T)$, and will only affect the mean and variance of wind speeds.

1.4.1 Effect of Non-Stationarity on Extreme Value Distributions

There has been a growing interest in developing non-stationary extreme value models, as the frequency and magnitude of extreme climatic events are likely to continue changing in the future. A general, pragmatic approach is to assume the data are still realizations of a given extreme value distribution family (e.g., GEVD, GPD,

etc.), but where the parameters may vary with time (Renard et al., 2013). For the block maxima method, which is used in this thesis, non-stationarity is introduced by expressing one or more of the parameters of the GEVD as a function of time (Katz, 2013). That is, $\mu(t)$, $\sigma(t)$, and $\xi(t)$, for $t = 1, 2, ...$ The parameter values at each time step are different, which makes them impossible to estimate based on a single series of observations (Renard et al., 2013). Consequently, the form of the non-stationarity model must be hypothesized for each parameter (Renard et al., 2013). For example, the GEVD with

$$\mu(t) = \mu(0)\left(1 + \Delta_\mu t\right), \qquad \sigma(t) = \sigma(0)\left(1 + \Delta_\sigma t\right), \qquad \xi(t) = \xi \tag{1.38}$$

where Δ_μ and Δ_σ are the rates of change in the mean and standard deviation, receptively, relative to their initial values. This model incorporates a linear trend in the location and scale parameters but no trend in the shape parameter, so the type of GEVD is constant over time. Alternative forms of each parameter model may also be used, including log-linear trends, polynomial trends, step changes, or some combination of them (Renard et al., 2013).

The non-stationary extreme value model used in this thesis for the annual maximum one-hourly average wind speed in year y, $V_{A1}(y)$, is similar to eq. (1.38), except time, t, is discretized into steps of length one year so that $y = 1, 2, ...$, allowing for numerical solutions. Additionally, $\xi(t) = 0$ because the Gumbel distribution was found to be most appropriate for extreme wind speeds (see Section 1.3.2). This non-stationary Gumbel distribution is assumed to have a linearly increasing mean and standard deviation with year y (i.e., $\mu_{v_{A1}}(y) = \mu_{v_{A1}}(0)\left(1 + \Delta_\mu y\right)$ and $\sigma_{v_{A1}}(y) = \sigma_{v_{A1}}(0)\left(1 + \Delta_\sigma y\right)$). Therefore, the CDF of the annual maximum one-hourly average wind speed in year y, $v_{A1}(y)$, is given by

$$F_{v_{A1}}(v; y) = \Pr(v_{A1}(y) \leq v(y)) = \exp\left(-\exp\left(-\frac{v(y) - u_{v_{A1}}(y)}{a_{v_{A1}}(y)}\right)\right) \tag{1.39}$$

where $a_{v_{A1}}(y) = \frac{\sigma_{v_{A1}}(y)\sqrt{6}}{\pi}$ and $u_{v_{A1}}(y) = \mu_{v_{A1}}(y) - 0.5772 a_{v_{A1}}(y)$ are the scale and location parameters for year y, respectively. A linear model is selected because it is useful for modelling the expected long-term trend in extreme wind speeds, even though the behaviour of extremes due to climate is unlikely to increase linearly. Recent mean temperature data shows periods of sharp increases followed by plateaus

(Cooley, 2013). Also note that eq. (1.38) assumes that the scale parameter increases with time, which ensures $\sigma_{v_{A1}}(y) \geq 0$. This is a reasonable assumption because uncertainties in extreme events are increasing as a result of climate change (Seneviratne et al., 2017).

Estimating the parameters, Θ, of the non-stationary Gumbel distribution (i.e., Δ_μ, and Δ_σ for eq. 1.38) can be done using several techniques. Katz (2013) describes a straightforward approach using the MML. The MML estimates the Gumbel distribution parameters, Θ, by minimizing the negative log likelihood (NLLH) function, $-\ln L(b_1, b_2, ..., b_n; \Theta)$, with respect to Θ. The NLLH function measures how probable the n observed block maxima, b_i, are as a function of Θ. Bayesian techniques, while more complex than the MML, are also used for non-stationary GEVD parameter estimation (Renard et al., 2013; L. Cheng et al., 2014). Bayesian inference has become increasingly popular due to the ability to quantify estimation and predictive uncertainties (Renard et al., 2013). However, as usual, the Bayesian results are highly dependent on the assumed prior, which can very much decrease its accuracy.

After the model parameters are estimated, several candidate models can be quantitatively assessed to determine the model that best represents the observations. These candidate models may include the linear trend model given in eq. (1.38), as well as models with various alternative forms for each parameter, including log-linear trends, polynomial trends, etc. Two common criteria used to evaluate the model of best-fit based on the MLL framework are the AIC and the Bayesian information criterion (BIC) (e.g. Friedman et al., 2001). Both criteria aim to select the model with the minimum NLLH function value, while also penalizing the number of parameters used to prevent over fitting (Katz, 2013). Bayesian inference may also be used for model selection as described by Renard et al. (2013).

1.4.2 Effect of Non-Stationarity on Return Period

Under non-stationary conditions, the equations for return period provided in Section 1.3.3 do not remain valid, as the annual exceedance probability, p, changes with time. Consequently, the two interpretations of return period, (1) expected time to the next exceedance event and (2) expected number of exceedance events (discussed in Section 1.3.3), are no longer equivalent, leaving the definition of return period

ambiguous. This subsection examines the effect of non-stationarity on these two interpretations of return period and provides an example to demonstrate the difference in results.

To define the non-stationary exceedance probability for year y, $p(y)$, let M_y denote the random variable representing the annual maximum for year y, and let $F(x;y) = \Pr(M_y \leq x)$ denote the CDF of M_y. The exceedance probability $p(y)$ then is the probability M_y exceeds a threshold r during year y, given by

$$p(y) = \Pr(M_y > r) = 1 - F(r;y) \tag{1.40}$$

where $F(x;y)$ is a non-stationary extreme value distribution (e.g., eq. 1.39).

Given the yearly exceedance probability $p(y)$, the definition of return period m_1, which is the expected number of years until the next exceedance event, can be defined. The distribution of the waiting time, N_n (from $y = 0$), until an exceedance over r occurs is given by (Cooley, 2013; Olsen et al., 1998)

$$\begin{aligned} \Pr(N_n = n) &= \Pr(M_1 \leq r)\Pr(M_2 \leq r)...\Pr(M_{n-1} \leq r)\Pr(M_n > r) \\ &= p(n)\prod_{y=1}^{n-1}\left[1 - p(y)\right] \end{aligned} \tag{1.41}$$

The expected time to the next exceedance event is therefore (Cooley, 2013)

$$\begin{aligned} m_1 = \mathrm{E}[N_n] &= \sum_{n=1}^{\infty} n\, p(n) \prod_{y=1}^{n-1}(1 - p(y)) \\ &= 1 + \sum_{i=1}^{\infty}\prod_{y=1}^{i}\left[1 - p(y)\right] \end{aligned} \tag{1.42}$$

where m_1 is the return period corresponding to the threshold r.

Next, the return period m_2, which has an expected number of exceedances above the threshold r in m_2 years equal to one is considered. Let N_{m_2} be the number of exceedances in m_2 years, and I be an indicator variable. The number of exceedances in m_2 years is defined as (Cooley, 2013)

$$N_{m_2} = \sum_{y=1}^{m_2} I(M_y > r) \tag{1.43}$$

The expected number of exceedance events is therefore

$$\begin{aligned} \mathrm{E}[N_{m_2}] &= \sum_{y=1}^{m_2} \mathrm{E}[I(M_y > r)] \\ &= \sum_{y=1}^{m_2} p(y) \end{aligned} \tag{1.44}$$

The m_2-year return period can then be solved numerically by computing the upper limit of the summation, m_2, such that (Cooley, 2013; Read and Vogel, 2015)

$$1 = \sum_{y=1}^{m_2} p(y) \tag{1.45}$$

The following example investigates the potential effects of non-stationarity on extreme wind speed return periods in Toronto, Ontario. As discussed in Section 1.4.1, under climate change, the annual maximum hourly-average wind speed is assumed to follow a non-stationary Gumbel distribution with linearly increasing mean and standard deviation, and the CDF of the annual maximum one-hourly average wind speed in year y is given by eq. (1.39). The initial mean and standard deviation used in this example are $\mu_{v_{A1}}(0) = 76.7\,\mathrm{km\,h^{-1}}$ and $\sigma_{v_{A1}}(0) = 7.27\,\mathrm{km\,h^{-1}}$, respectively, which are the current mean and standard deviation of v_{A1} for Toronto, Ontario found by Hong et al. (2014*b*). Hong et al. (2014*b*) determined these results by fitting the Gumbel distribution to 47 years of hourly-average wind speed data recorded at Toronto Pearson Int'l Airport. The expected change in $\mu_{v_{A1}}(0)$ and $\sigma_{v_{A1}}(0)$ due to climate change is currently poorly known, therefore, this example provides a parametric analysis for $0 \leq \Delta_\mu = \Delta_\sigma \leq 0.01$, where Δ_μ and Δ_σ, are the annual rates of change in $\mu_{v_{A1}}$ and $\sigma_{v_{A1}}$, respectively, relative their initial values.

The probability of exceedance over a threshold r, in year y is then defined as

$$p(y) = 1 - \Pr(v_{A1}(y) \leq r) = 1 - F_{v_{A1}}(r; y) \tag{1.46}$$

where, in this example r is the current 50-year return annual maximum wind speed for Toronto, Ontario given by $r = F^{-1}_{v_{A1}}(1 - \frac{1}{50}; 0) = 95.5\,\mathrm{km\,h^{-1}}$. Figure 1.11(a) demonstrates three cases of how the non-stationary probability of exceedance, $p(y)$, changes over 50 years for $\Delta_\mu = \Delta_\sigma = 0.005$ in Toronto, Ontario. Figure 1.11(b) shows the probability of exceedance in year 50, $p(50)$, for the same three cases for $0 \leq \Delta_\mu = \Delta_\sigma \leq 0.01$.

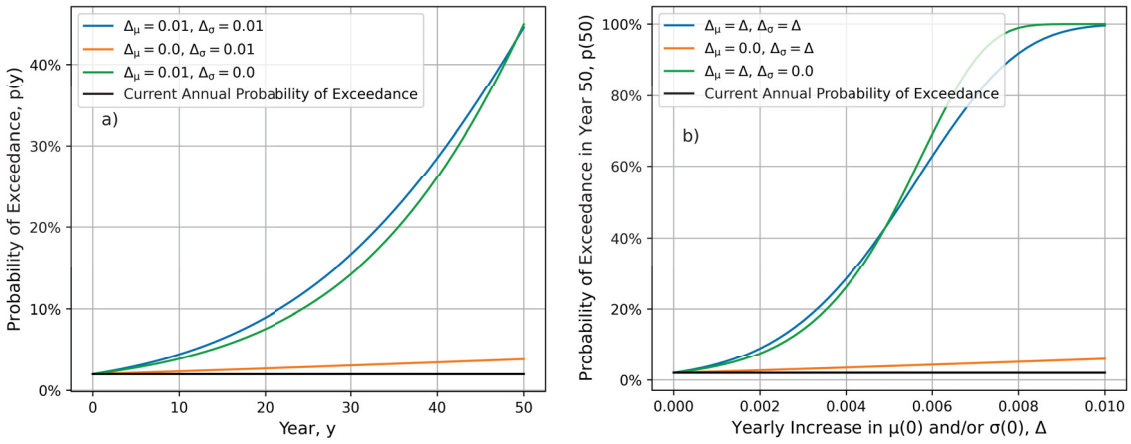

Figure 1.11: Non-stationary probability of exceeding $r = 95.5\,\mathrm{km\,h^{-1}}$, $p(y)$, for Toronto, Ontario when (a) $0 \leq y \leq 50$ for $\Delta_\mu = \Delta_\sigma = 0.005$, and (b) $0 \leq \Delta_\mu = \Delta_\sigma \leq 0.01$ for $y = 50$.

In Fig. 1.11(a), case 1 (green line) shows that when $\mu_{v_{A1}}(y)$ linearly increases by 0.5% each year (25% over 50 years) and $\sigma_{v_{A1}}(y)$ is constant, $p(y)$ increases from 2% to 44.8%. In comparison, case 2 (orange line) shows that when $\sigma_{v_{A1}}(y)$ linearly increases by 0.5% each year and $\mu_{v_{A1}}(y)$ is constant, $p(y)$ only increases to 3.8%. Finally, case 3 (blue line) demonstrates that linearly increasing both $\mu_{v_{A1}}(y)$ and $\sigma_{v_{A1}}(y)$ by 0.5% each year results in $p(y)$ increasing to 44.5%. The figure demonstrates that for the same annual increase, Δ, increasing the mean of the annual maximum wind speed results in approximately a ten times greater increase in $p(50)$, compared to increasing the standard deviation of v_{A1}. This is expected as $\mu_{v_{A1}}(0)$ is also approximately ten times greater than $\sigma_{v_{A1}}(0)$, resulting in the absolute value of the increase in $\mu_{v_{A1}}(y)$ being significantly larger than that of $\sigma_{v_{A1}}(y)$. Figure 1.11(b) demonstrates that for the entire range $0 \leq \Delta_\mu = \Delta_\sigma \leq 0.01$, increases in the mean have a more significant impact on $p(50)$ than those in the standard deviation. Case 1 consistently has a higher exceedance probability in year 50 than case 2, although, the difference between $p(50)$ for case 1 and case 2 is lower for smaller values of Δ. Figure 1.11(b) also shows that as Δ approaches 0.01, $p(50)$ approaches 100% for case 1 and case 3, meaning if the mean of v_{A1} increases by 50% (1% increase per year over 50 years) it is almost certain the current 50-year return annual maximum wind speed will be exceeded in any given year. Additionally, note that $p(50)$ for case 1 exceeds that of case 3 for $\Delta \geq 0.005$, resulting from the increase in standard deviation having a more dominant

effect on decreasing location parameter than on increasing the scale parameter (recall $u(y) = \mu(y) - 0.5772a(y)$ and $a(y) = \frac{\sigma(y)\sqrt{6}}{\pi}$).

Given the non-stationary probability of exceedance, both definitions of return period can be solved numerically. The return period, m_1 (eq. 1.42), which is the expected number of years until the next exceedance event, is solved by truncating the infinite sum when the solution to m_1 converges to within some tolerance, here assumed to be 10^{-7}. For this example, an upper limit of 10^5 is used, as the solution to m_1 for the range $0 \leq \alpha \leq 0.5$ is constant within 10^{-7} from an upper limit of 10^5 to 10^6. The second definition of return period, m_2 (eq. 1.45), which has an expected number of exceedances above the threshold r in m_2 years equal to one, is solved by determining m_2, where $1 = \sum_{y=1}^{m_2} p(y)$. Linear interpolation is used between the points where the sum of $p(y)$ is just less than 1 and just greater than 1 to solve for m_2. Figure 1.12(a) shows the expected number of years until next exceedance event (m_1) over $r = 95.5\,\mathrm{km\,h^{-1}}$ in Toronto, Ontario, while Fig. 1.12(b) shows the solution to m_2 for the same conditions.

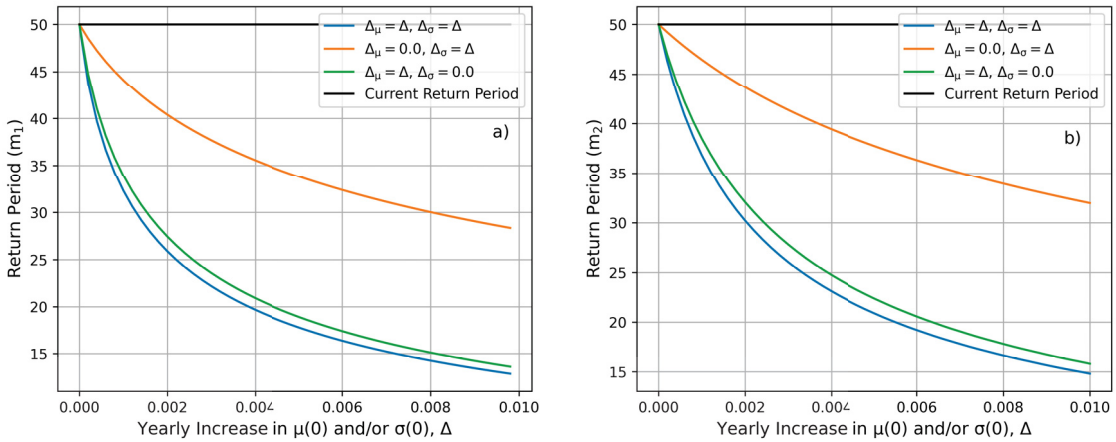

Figure 1.12: Return period for exceedance event over $r = 95.5\,\mathrm{km\,h^{-1}}$ vs. the yearly rates of increase, Δ_μ and Δ_σ, in $\mu_{v_{A1}}(0)$ and $\sigma_{v_{A1}}(0)$, respectively, for Toronto, Ontario when return period is defined as (a) m_1 and (b) m_2.

Figure 1.12 shows both m_1 and m_2 are significantly reduced even with a small increase in mean and standard deviation if the current design wind speed continues to be used in the future. For example, a 0.2% yearly increase in $\mu_{v_{A1}}$ and $\sigma_{v_{A1}}$ causes the expected return period of the current design wind speed to be reduced from 50 years to 30 years for m_2, or less for m_1. Figure 1.12 also demonstrates that m_1 is slightly smaller than

m_2 for the same increase, Δ. In other words, the expected time to the next exceedance event is less than the expected number of years with one exceedance event.

Figures 1.11 and 1.12 show the effects of non-stationarity on the probability of exceedance and return period, respectively, in the scenario where the current design wind speed continues to be used in the future (i.e., r is constant). Conversely, Fig. 1.13 shows the increase in the current design wind speed, $v_{A1,50}$, required to maintain a 50-year return period. Figures 1.13(a) and (b) are based on return period definitions m_1 and m_2, respectively. The required increase in $v_{A1,50}$ shown on the y-axis is defined as the factor, c, such that $cv_{A1,50}$ is the design wind speed required to maintain a 50-year return period.

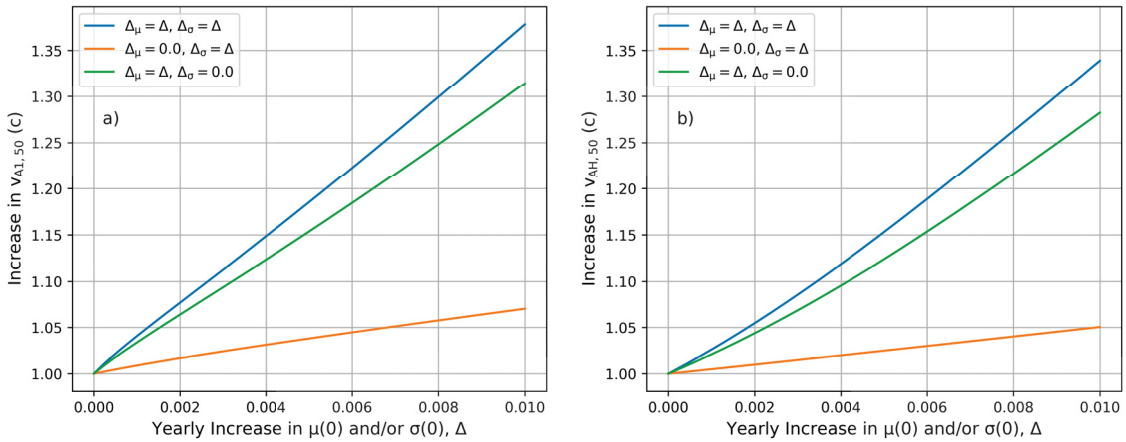

Figure 1.13: Increase in design wind speed ($r = 95.5\,\mathrm{km\,h^{-1}}$) required to maintain 50-year return period vs. the yearly rates of increase, Δ_μ and Δ_σ, in $\mu_{v_{A1}}$ and $\sigma_{v_{A1}}$, respectively, for Toronto, Ontario when return period is defined as (a) m_1 and (b) m_2.

Figures 1.13(a) and 1.13(b) demonstrate that relatively small increases in the design wind speed can have a significant effect on achieving a constant return period (50 years). As previously mentioned, the return period m_2 was reduced by 40%, from 50 to 30 years, when both $\mu_{v_{A1}}(y)$ and $\sigma_{v_{A1}}(y)$ are increased at $\Delta = 0.002$. However, increasing the design wind speed by only 5.5% ($c = 1.055$) results in the return period (m_2) remaining at 50 years. Similar results are also found using return period m_1. Note that the maximum difference between the magnitude of the design wind speed based on m_1 and m_2 is 3.9% at $\Delta = 0.01$. This corresponds to a $3.7\,\mathrm{km\,h^{-1}}$ difference in Toronto, Ontario.

While m_1 is slightly more conservative, m_2 is more logical in the context of structural design, as the year of occurrence is less important than ensuring the structure can withstand all expected loads over the design lifetime. This is confirmed by assessing the 50-year lifetime exceedance probability, p_{50}, defined as

$$\begin{aligned} p_{50} &= \Pr(N_{m_2=50} \geq 1) \\ &= 1 - \Pr(N_{m_2=50} = 0) \\ &= 1 - \prod_{y=1}^{50} \left[1 - p(y)\right] \end{aligned} \tag{1.47}$$

where $N_{m_2=50}$ is the number of exceedance events in 50 years. Under stationary conditions $p(y) = 0.02$ for all y. Therefore, the current 50-year lifetime exceedance probability is $p_{50} = 1 - 0.98^{50} = 0.64$. The 50-year lifetime exceedance probability for non-stationary $p(y)$ is calculated based on the scenario that the mean and standard deviation of V_{A1} increase by $\Delta_\mu \mu_{v_{A1}}(0)$ and $\Delta_\sigma \sigma_{v_{A1}}(0)$, respectively, each year. Additionally, the design wind speed, r, used to calculate p_{50} is also based on these same changes (Δ_μ and Δ_σ) in $\mu_{v_{A1}}(y)$ and $\sigma_{v_{A1}}(y)$, shown in Fig. 1.13. In other words, the calculation of p_{50} assumes the model used to determine the design wind speed, r, is actually realized in the future. The current value of p_{50} as well as the results based on the design speed required to maintain a 50-year return period for m_1 and m_2 are shown in Fig. 1.14(a) and (b), respectively.

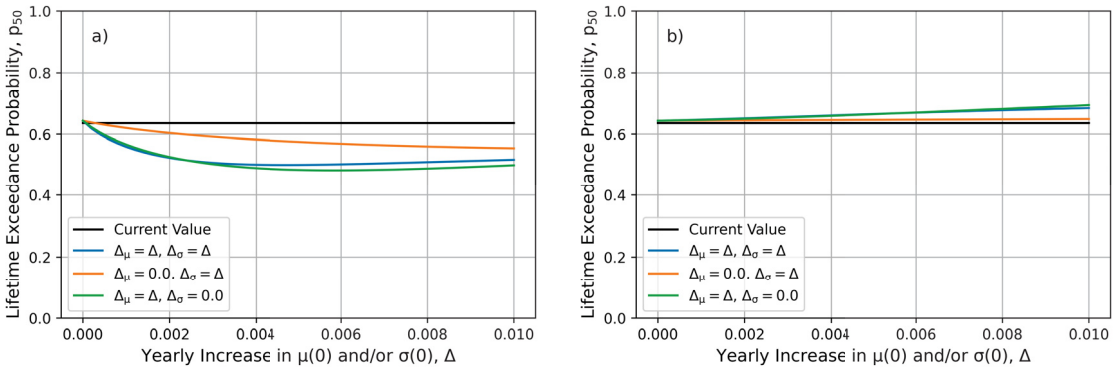

Figure 1.14: Fifty-year lifetime exceedance probability for Toronto, Ontario vs. the yearly rates of increase, Δ_μ and Δ_σ, in $\mu_{v_{A1}}(0)$ and $\sigma_{v_{A1}}(0)$, respectively. The design wind speed, r, is also calculated assuming the same yearly rates of increase, Δ_μ and Δ_σ, and r is the wind speed required to maintain a 50-year return period when return period is defined as (a) m_1 and (b) m_2.

Figure 1.14 shows that p_{50} is lower when the design wind speed is determined based on m_1, but that m_2 results in a lifetime exceedance probability that is much closer to the current value of p_{50}. This demonstrates that m_1 results in slight over design, therefore, m_2 is used in this thesis.

1.4.3 Effect of Non-Stationarity on the Gust Factor

The analytical gust factor model developed in Section 1.3.4 was developed assuming that instantaneous wind speeds follow a stationary stochastic process. However, it is likely that climate change will effect the instantaneous wind speed distribution such that the mean and variance are no longer stationary, resulting in changes to CV_V. Therefore, eq. (**??**) is no longer valid. To account for the future non-stationary wind speed distribution, the coefficient of variation, CV_V, is redefined for year y as

$$\mathrm{CV}_V(y) = \frac{\sigma_V(y)}{\mu_V(y)} \tag{1.48}$$

where $\mu_V(y)$ and $\sigma_V(y)$ are the mean and standard deviation of the instantaneous wind speed in year y. For this study, the variance reduction function, $\gamma(T)$, used to determined G in eq. (**??**) is assumed to be constant with time. The non-stationary gust factor is then

$$G_y(w,W) = 1 + g(w,W)\mathrm{CV}_V(y)\sqrt{\gamma(w) + \gamma(W) - 2\sqrt{\gamma(w)\gamma(W)}\mathrm{Cov}(Y_w, Y_W)} \tag{1.49}$$

where $g(w,W)$ remains as the mean of the $\frac{w}{W}$-return period extreme value distribution.

The non-stationary gust factor, G_y, was evaluated at a short-term averaging duration $w = 3$ sec and long-term averaging duration $W = 1$ hour for a range of values of $\mathrm{CV}_V(y)$ to evaluate the effect of $\mu_V(y)$ and $\sigma_V(y)$. Figure 1.15(a) shows the gust factor at year 50 when $\mu_V(y)$ increases by Δ_μ each year, and $\sigma_V(y)$ is constant. That is, $\mu_V(y) = \mu_V(0)\left(1 + \Delta_\mu y\right)$, and $\sigma_V(y) = \sigma_V(0)$ for all y. Conversely, Fig. 1.15(b) shows the gust factor at year 50 when $\sigma_V(y)$ increases by Δ_σ each year, and $\mu_V(y)$ is constant (i.e., $\sigma_V(y) = \sigma_V(0)\left(1 + \Delta_\sigma y\right)$, and $\mu_V(y) = \mu_V(0)$ for all y). The initial mean and standard deviation of the instantaneous wind speed were determined empirically as the average of that of the four locations in Fig. 1.4, and were found to be $\mu_V(0) = 11.69$ and $\sigma_V(0) = 7.45$, respectively.

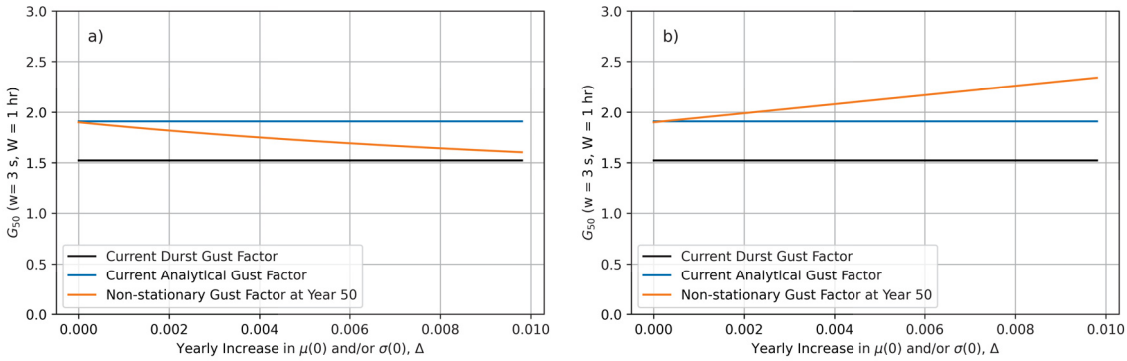

Figure 1.15: Non-stationary gust factor, $G_y(w = 3\text{ sec}, W = 1\text{ hr})$, at $y = 50$ where (a) $\mu_V(y) = \mu_V(0)\left(1 + \Delta_\mu y\right)$ and $\sigma_V(y) = \sigma_V(0)$ for all y, and (b) $\sigma_V(y) = \sigma_V(0)\left(1 + \Delta_\sigma y\right)$ and $\mu_V(y) = \mu_V(0)$ for all y.

Figure 1.15 demonstrates that a 1% increase in the instantaneous wind speed variance each year for 50 years results in $\mathrm{CV}_V(50) = 0.95$, and $G_{50}(w = 3\text{ sec}, W = 1\text{ hr})$ increasing from 1.90 to 2.34. While, a 1% yearly increase in the instantaneous wind speed mean for 50-years results in $\mathrm{CV}_V(50) = 0.43$, and $G_{50}(w = 3\text{ s}, W = 1\text{ hr})$ decreasing from 1.90 to 1.60. Note that if the wind speed mean and variance increase at the same rate (i.e., $\Delta_\mu = \Delta_\sigma = \Delta$) there is no change the coefficient of variation since

$$\begin{aligned} \mathrm{CV}_V(y) &= \frac{\sigma_V(y)}{\mu_V(y)} = \frac{\sigma_V(0)\left(1 + \Delta_\sigma y\right)}{\mu_V(0)\left(1 + \Delta_\mu y\right)} \\ &= \frac{\sigma_V(0)\left(1 + \Delta y\right)}{\mu_V(0)\left(1 + \Delta y\right)} \\ &= \frac{\sigma_V(0)}{\mu_V(0)} = \mathrm{CV}_V(0) \end{aligned} \tag{1.50}$$

1.5 Organization of Thesis

The aim of this thesis is to understand the potential effects of climate change on wind loading structural design requirements, and to develop an updated wind loading design method that not only accounts for the projected increases in wind speeds and uncertainties due to climate change, but also improves exceedance probability consistency across Canada. In the following chapters, three new wind loading design methods that can be used under climate change are developed. The three methods,

proposed herein, are based on the "ultimate return period" and the Load and Resistance Factor Design methods. An analysis consisting of quantitative metrics and practical considerations is completed to determine which of the three wind loading design methods best achieves the objectives of this thesis. Wind loading design parameters are recommended for three exceedance probability target levels and three design lifetime durations under four climate change scenarios, with the intent of providing structural engineers with the flexibility to use their knowledge and experience to select the design parameters that are most appropriate for future use.

Chapter 2 is comprised of a literature review of state-of-the-art climate change models; the results of which are used to reformulate the statistical distributions typically used to model speeds. The sources of uncertainty in these climate change model projections, and the associated magnitudes of uncertainty, are also assessed.

Chapter 3 expands on the discussion of the traditional wind loading design method used in the NBCC, the LRFD method. Current design wind speed statistical parameters are introduced, and the current design wind speed exceedance probabilities are investigated. An updated LRFD method that accounts for climate change is then proposed. New LRFD-based design parameters and the corresponding design wind speeds to be used under four climate change scenarios are presented. The 50-year exceedance probabilities of these updated design wind speeds are then evaluated under a range of climate change scenarios. Further analysis of the effect of climate change on the gust effect factor is also completed in Chapter 3.

Chapter 4 explores the application of the "ultimate return period" design method, an alternative wind loading design method, under current climate conditions and under climate change. An analysis comparing the ultimate return period method to the LRFD method under current climate conditions is performed, which presents the LRFD and ultimate return period design wind speeds. The advantages and disadvantages of each method are also discussed. Two alternative ultimate return period-based methods that account for climate change are then proposed. Similar to Chapter 3, the design parameters and the corresponding design wind speeds are presented for each of the two new methods under four climate change scenarios. The 50-year exceedance probabilities of these design wind speeds are then evaluated under a range of climate change scenarios.

Chapter 5 compares the three design methods, proposed herein, for wind loading under climate change, and further analyzes the design method found to perform best overall, the "Hybrid Ultimate Return Period" (HURP) method. The three wind loading design methods are compared based on their ability to achieve the target 50-year lifetime exceedance probability under climate change at all the locations across Canada assessed in this thesis as consistently as possible. The sensitivity of the HURP design parameters and wind speeds to the exceedance probability target is then evaluated. Additionally, the effects of design lifetime on the HURP design wind speeds and corresponding exceedance probabilities are investigated because in practice the real lifetime of a well-maintained structure is significantly larger than the design working life defined by structural codes (which is 50 years in the NBCC).

Chapter 6 presents conclusions and suggestions for future work.

Chapter 2

Climate Change Models

2.1 General

Climate models are used to make long-term predictions of the Earth's climate system, and are the primary tool for investigating the effects of various forcing scenarios over the next century and beyond (Flato et al., 2018). The Intergovernmental Panel on Climate Change (IPCC) developed several future forcing scenarios, called Representative Concentration Pathways (RCPs), which indicate different levels of radiative forcing caused by anthropogenic factors. For example, RCP2.6 represents a low emission pathway with a change in radiative forcing of $2.6\,\mathrm{W\,m^{-2}}$ (Seneviratne et al., 2017). These RCPs enable standardization of conditional climate models for projections of parameters such as wind speeds.

Climate models range in complexity from simple energy balance models to earth system models (ESMs), the latter of which represent the climate system through mathematical equations that describe thermodynamics and fluid dynamics (Asch et al., 2016). ESMs expand upon their predecessor, general circulation models, to include physical, chemical and biological processes, while general circulation models only represent physical processes in the atmosphere, ocean and cyrosphere (Asch et al., 2016). Both general circulation models and earth system models can be considered global climate models, hereinafter referred to as GCMs. The disadvantage of these highly complex GCMs is the enormous computational power required, limiting models to coarse spatial scale projections.

Extreme weather events are generally difficult to realistically represent in climate models because they are realizations of the tail of the distribution for a climate variable (Flato et al., 2018). Additionally, extreme events often have smaller scale spatial structures which are difficult to accurately represent in a model (Flato et al., 2018). Extreme wind speeds are particularly challenging to model since wind flow is nonlinear and dependent on complex terrain (Goyette, 2008). Due to these complexities,

wind speeds are typically modelled using GCMs combined with downscaling techniques to increase the spatial resolution of the GCM. Downscaling techniques are often applied to GCM results to provide climate projections at a finer spatial scale because the resolution of GCMs is very low, typically around 1 to 3 degrees (100 to 300 km) (Vandal et al., 2017).

2.2 Global Climate Models

Global Climate Models (GCMs) are physics-based numerical models that simulate the Earth's response to various greenhouse gas emissions scenarios. GCMs represent the fundamental laws of nature (e.g., energy, mass and momentum conservation) through mathematical equations, which are developed based on theoretical and observational work (Flato et al., 2018). These equations are then discretized using numerical methods, and implemented on a grid (e.g., latitude-longitude-height) (Flato et al., 2018). Processes that cannot be represented by discretized equations due to their complexity (e.g., biochemical processes in vegetation) or spatial and/or temporal scale (e.g., cloud processes and turbulence) are implemented using conceptual models that are based on observations and comprehensive process models (Flato et al., 2018).

The disadvantage of GCMs over simple energy balance models is the enormous computational resources required for GCMs. Limitations on supercomputer resources results in three main areas where model accuracy may be compromised due to computational constraints. These three areas include spatial and/or temporal model resolution, complexity of climate system processes, and understanding of uncertainties. Spatial or temporal model resolution may be reduced to decrease the required computational resources. Higher resolution models are generally more mathematically accurate, but may not be feasible. It should be noted that higher resolution models do not always lead to more reliable simulations (Flato et al., 2018). In addition to decreasing model resolution, certain processes or components in the highly complex climate system may be excluded, typically also reducing model accuracy while reducing computational resources. These trade-offs are generally made based on the relative importance of the process or component, which is dependent on the time scale of interest (Flato et al., 2018). Limited computational resources has also led to

poor knowledge of uncertainties in climate change models (see Section 2.4). Quantifying uncertainties requires running several simulations, and consequently, immense computational resources. Therefore, limited studies have been completed to date, resulting in a deficient understanding of uncertainties in climate model projections.

2.3 Downscaling Techniques

Downscaling techniques are applied to GCMs to provide climate projections at finer spatial scales, necessary for understanding climate change effects at the regional and local scale. Downscaling is particularly important for understanding changes to extremes. The two main downscaling technique classes are dynamical and statistical downscaling. Dynamical downscaling, or regional climate models (RCMs), are similar to GCMs but are on a finer spatial scale and use the GCM results for boundary conditions. Alternatively, the objective of statistical downscaling is to determine a statistical relationship between historical GCM results and high-resolution observations. This relationship is then applied to future GCM results to produce high-resolution climate projections. Statistical downscaling methods range from linear models to neural networks.

Dynamical downscaling is often regarded as more accurate since the intricate RCMs are better equipped to account for complex terrain and the non-linear behaviour of wind flow (Goyette, 2008). However, the value of RCMs has been questioned. Racherla et al. (2012) found that the most important factor in the skill of the RCM is the credibility of the driving GCM, and that the RCM did not add significant value beyond downscaling through simple interpolation.

The benefit of statistical downscaling techniques is that they are computationally efficient, relative to dynamical downscaling methods. Computational efficiency is particularly important when downscaling multi-model ensembles to understand uncertainties, as RCMs can be prohibitively expensive.

2.4 Sources of Uncertainty

There are several sources of uncertainty in climate change models that make predicting climatic variables, such as wind speeds, challenging. The major sources of

uncertainty include the emissions scenario realized in the future, model formulation (i.e., GCM and RCM architecture) and internal (or natural) variability in the Earth's climate. Assessing the uncertainty associated with the emissions scenarios can be estimated by running identical models for various RCPs. While the amount of radiative forcing emitted in the future is very uncertain, as it dependent on human behaviour, it is important to assess how a range of plausible forcing scenarios will impact the Earth's climate system. That is, it is important to estimate how climatic variables change as a function of uncertain radiative forcing.

Model uncertainty is the uncertainty associated with the GCM and RCM architecture and resolution, which can be estimated by running different models for the same RCP. GCM architecture and resolution uncertainty involves differences in techniques used to discretize equations and represent sub-grid effects within various GCMs (Pryor et al., 2012*a*). Differences in these techniques results in variations in the lateral boundary conditions applied to the RCM. Therefore, GCM architecture uncertainty is also referred to as boundary uncertainty. RCM architecture uncertainty is estimated as the difference in projections between various RCMs that have the same lateral boundary conditions but differing architecture and/or resolution (Pryor et al., 2012*a*).

Finally, internal variability, which may also be referred to as sampling uncertainty, is the variation in outcomes resulting from insufficient temporal windows (i.e., 20 vs. 50 years, 50 years being more accurate) (Pryor et al., 2012*a*). Assessing future climate conditions based on a short time period can lead to errors in conclusions since there is currently significant decadal variability in the climate. For example, the wind climate varies with the North Atlantic Oscillation, which is a weather phenomenon resulting in fluctuations in the atmospheric pressure at sea level (SLP) over the North Atlantic Ocean.

The order of importance of these sources of uncertainty varies by the prediction lead time (i.e., 10 vs. 50 years from present), the spatial and temporal averaging scale of the predicted values, and the quantile of the distribution being predicted (i.e., mean vs. extreme events). Regarding sources of uncertainty, Hawkins and Sutton (2009) studied twenty-first-century surface air temperatures and found that internal variability was most important for the first decade, then model uncertainty

dominated out to 50 year lead time, after which the emissions scenario uncertainty dominated. It is important to note that, while the relative importance of some sources of uncertainty may decrease with time (e.g., internal variability) the total uncertainty in mean temperature predictions increases with time (Hawkins and Sutton, 2009). Hawkins and Sutton (2009) also found that, in general, internal variability uncertainty was more significant for smaller spatial and temporal scales. Although Hawkins and Sutton (2009) only studied surface air temperature, it is likely that their results are transferrable to wind speed projections. S. C. Cheng et al. (2014) studied the magnitude of uncertainty in wind gust predictions and found that model formulation and emissions scenario uncertainty accounted for less than half the projected increase in wind gust magnitude for wind gusts $\geq 28\,\mathrm{km\,h^{-1}}$. However, the model formulation and emissions scenario uncertainty were greater than the projected increase in wind gust magnitude for wind gusts $\geq 90\,\mathrm{km\,h^{-1}}$, partially due to rare cases of extreme gusts (S. C. Cheng et al., 2014). S. C. Cheng et al.'s (2014) results demonstrate that uncertainties are larger for more extreme wind speed events.

Studies that aim to quantify the magnitude of the sources of uncertainty are limited, as they require immense computational resources. Quantifying uncertainty is challenging because there are over 40 GCMs that are currently part of the Coupled Model Intercomparison Project Phase 5 (CMIP5), which the IPCC recognizes as consistent and well-documented climate model experiments (Flato et al., 2018). Quantifying uncertainties in model formulation, initial conditions and between-emissions scenarios requires running several simulations across all these models, increasing computational cost. Consequently, comprehensive studies of uncertainties have yet to be completed. Nonetheless, smaller studies have been completed which provide some insight into the magnitudes of the various sources of uncertainty in extreme wind speed projections.

Emissions scenario projections are highly uncertain as future radiative forcing is dependent on human behaviour. Accordingly, the IPCC has not attributed likelihoods to the various emissions scenarios (i.e., RCPs). Regardless, it is important to evaluate the difference in wind speed projections based on the various emissions scenarios to understand the range in which climatic variables may change in the future. S. C. Cheng et al. (2014) analysed interscenario uncertainties between the Special Report

on Emissions Scenarios (SRES) A2 (slightly below RCP 8.5) and B1 (similar to RCP 4.5) in future hourly wind gust event projections based on eight GCMs and quantitatively evaluated the region-averaged absolute difference between scenarios A2 and B1. They found that the mean difference between scenarios in hourly wind gust projection magnitudes for hourly wind gust events $\geq 28\,\mathrm{km\,h^{-1}}$ was 3 to $5\,\mathrm{km\,h^{-1}}$, while that for wind gusts $\geq 40\,\mathrm{km\,h^{-1}}$ was 3 to $12\,\mathrm{km\,h^{-1}}$, and wind gusts $\geq 70\,\mathrm{km\,h^{-1}}$ had a mean difference of 4 to $28\,\mathrm{km\,h^{-1}}$. Therefore, a reasonable range for interscenario uncertainty is 15% to 50%, as hourly wind gusts $\geq 28\,\mathrm{km\,h^{-1}}$ have an uncertainty of approximately 18%, while wind gusts $\geq 70\,\mathrm{km\,h^{-1}}$ are approximately 40% uncertain. Note that uncertainty increases for more extreme wind speed events, as previously mentioned.

Nikulin et al. (2011) and Pryor et al. (2012*b*) both completed studies that analyse model formulation uncertainty in wind speed predictions across small ensembles of climate change models. Nikulin et al. (2011) studied the effect of the GCM architecture on extreme wind speeds, by analysing a single RCM driven by six GCMs under the SRES A1B scenario. Their study showed a high degree of dependency on the GCM as the 20-year return period daily maximum wind gust differed by more than $10\,\mathrm{m\,s^{-1}}$ amongst individual simulations – that is, the 20-year return period wind gust was found to vary from 18 to $50\,\mathrm{m\,s^{-1}}$ across simulations. Therefore, it appears that GCM architecture uncertainty can range up to about 60% for wind gust projections. Pryor et al. (2012*b*) completed a similar analysis, assessing the magnitude of GCM and RCM architecture uncertainty seperately, for 90th percentile wind speeds. They analysed an ensemble of thirteen climate simulations based on five RCMs and four GCMs for the A2 emissions scenario (slightly below RCP 8.5) and found that the root mean squared difference (RMSD) between simulations with a common RCM but varying lateral boundary conditions (i.e., GCM) was 0.56 to $1.16\,\mathrm{m\,s^{-1}}$. They also found that the RMSD for models with a common lateral boundary conditions but varying RCM was 0.53 to $1.73\,\mathrm{m\,s^{-1}}$. Therefore, the uncertainty due to the GCM architecture was suggested to be less than that due to the RCM architecture. Based on Pryor et al.'s (2012*b*) results the maximum total model formulation uncertainty is $2.89\,\mathrm{m\,s^{-1}}$. Taking the mean annual 90th percentile wind speed to be $10\,\mathrm{m\,s^{-1}}$, the model formulation uncertainty is then suggested to be approximately 29% (17% from

the GCM, and 12% from the RCM). While there is currently limited knowledge of model formulation uncertainty, the above results demonstrate that model formulation uncertainty may range from approximately 30 to 75% for extreme wind speeds, providing a range that can used for parametric analysis.

Internal variability is the only main source of uncertainty in climate change models that has also existed historically. Consequently, the magnitude of internal variability is relatively conclusive in the literature. The wind energy industry often characterizes the inter-annual variability of the annual average wind speed as having a normal distribution with a coefficient of variation of 6% (Pryor et al., 2018). This variability may also be accounted for by assessing wind data over a sufficient time period. The wind speed projections used for this thesis are based on 30 years of simulated data, therefore, the sampling uncertainty caused by internal variability is considered to be accounted for.

2.5 Extreme Wind Speed Projections Under Climate Change

Advancements in computational resources have enabled researchers to employ state-of-the-art climate change models to study the effects of future emissions scenarios on wind speeds. These studies have been published with increasing frequency, particularly over the past decade, due to an increasing urgency to understand the potential negative effects of climate change. Currently, there are several published studies that forecast changes in wind speeds using combinations of various GCMs and RCMs, as well as other statistical downscaling techniques (e.g., Xu, 2019; Nikulin et al., 2011; Pryor et al., 2012*b*,). However, to the author's knowledge there are currently only three studies that use GCMs to predict the effects of climate change on future extreme wind speeds across Canada. Jeong and Sushama (2018) and Jeong and Sushama (2019) studied changes in the 50-year return period wind speed across Canada and North America, respectively. Both studies applied dynamical downscaling techniques to two GCMs under RCP 4.5 and 8.5, but used different RCMs. Meanwhile, S. C. Cheng et al. (2014) employed a statistical downscaling method on eight GCMs to predict changes in the frequency of wind gust events under SRES A2 and B1 across Canada. Details of these three studies are summarized below. Other analyses have mainly focussed on Europe and the contiguous United States, although some global

studies have been completed (e.g., Kumar et al., 2015). The disadvantage of using a global analysis is that the computational resources required to downscale GCM results over the entire globe are still prohibitively expensive. Without downscaling, the larger spatial scale may result in unreliable wind speed forecasts. However, the value addition of downscaling has been questioned, as a full ensemble of GCMs is rarely run in a single analysis, increasing the uncertainty in the results (Kumar et al., 2015). For this reason, a summary of Kumar et al.'s (2015) global study on wind extremes under climate change, which did not implement any downscaling method, is also included in this section for comparison.

To the author's knowledge, the first Canadian future extreme wind speed analysis was completed by S. C. Cheng et al. (2014), who analyzed the impacts of climate change on the frequency of future wind gust events. S. C. Cheng et al. (2014) used eight GCMs to simulate hourly wind gust data under SRES A2 and B1. They then employed a statistical model to downscale the results of each GCM. The downscaling function used three regression techniques including: multiple stepwise regression, stepwise orthogonal regression, and autocorrelation correction regression. A leave-one-year-out cross-validation procedure was used to calibrate the model, and the downscaled results were then validated by comparison with observed data. S. C. Cheng et al. (2014) found that for hourly wind gust events $\geq 90\,\mathrm{km\,h^{-1}}$, the absolute difference between the simulated and observed wind gusts was within 20% for 62% to 85% of locations, varying across different regions of Canada. The simulation projections showed that the frequency of wind gust events is expected to increase later in the 21st century, especially for more severe wind gusts (S. C. Cheng et al., 2014). The percent increase in the frequency of wind gust events ≥ 28 and $\geq 70\,\mathrm{km\,h^{-1}}$ across most regions of Canada is expected to be 10% and 20-30%, respectively (S. C. Cheng et al., 2014). Meanwhile, the percent increase in the frequency of wind gust events $\geq 90\,\mathrm{km\,h^{-1}}$ is expected to be more than 100% (S. C. Cheng et al., 2014).

Jeong and Sushama (2018) completed the first detailed study on extreme wind projections under climate change using RCM simulations for Canada. They evaluated the projected changes to the annual maximum 3-hourly wind speed for the future 2071–2100 period, with respect to the current 1981–2010 period. The authors used four different simulations from the fifth-generation Canadian Regional Climate Model

(CRCM5). The CRCM5 simulations considered in the study were driven by two GCMs (i.e., Canadian Earth System Model 2 (CanESM2) and Max-Planck-Institute Earth System Model (MPI-ESM)) for two RCPs, 4.5 and 8.5. The annual maximum wind speed time series, based on 3-hourly wind speed observations, was then used to estimate changes in the annual maximum wind speed distribution for all grid points over Canada. Note that "3-hourly" refers to observations taken on a 3-hourly basis, and does not refer to a 3 hour average. The distribution of the annual maximum wind speed based on the 3-hourly instantaneous observations, v_{A0}, was estimated by fitting the Gumbel distribution using the method of moments (MOM). This distribution was then used to determined the percent change in the mean and standard deviation of v_{A0}, as well as that of the corresponding 50-year return period annual maximum wind speed, $v_{A0,50}$. To validate the climate models, Jeong and Sushama (2018) compared the mean and 50-year return period annual maximum wind speed for the current 1981-2010 period to that determined by Hong et al. (2014*a*), who used observed hourly-average wind speed data from 235 meteorological stations. The spatial distributions of the two studies are mostly consistent, but the wind speed magnitudes of Jeong and Sushama (2018) are smaller. Jeong and Sushama (2018) presume the lower wind speed magnitudes are due to the estimates being based on 3-hourly observations, compared to hourly-average observations used by Hong et al. (2014*a*). The wind speed underestimation should not effect Jeong and Sushama's (2018) estimations of future changes because the future wind speed projections are presented as the percent change between the two time periods, and the underestimation should be consistent across both time periods. Jeong and Sushama's (2018) climate change projection results are shown in Fig. 2.1.

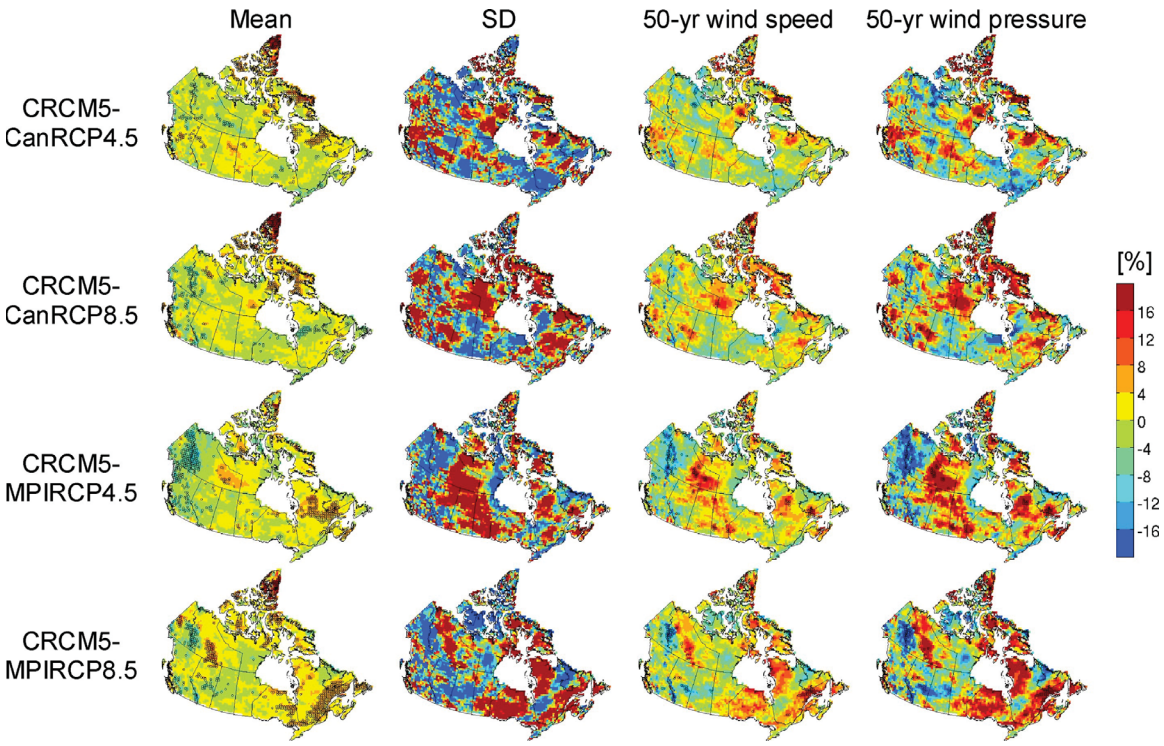

Figure 2.1: Projected changes to the mean and SD of the annual maximum wind speed, v_{A0}, (columns 1 and 2) and 50-year return period annual maximum wind speed, $v_{A0,50}$, and wind pressure (columns 3 and 4) for the future 2071–2100 period with respect to the current 1981–2010 period (Jeong and Sushama, 2018).

Figure 2.1 shows that changes in the mean annual maximum wind speed are within -4% to +4% across most regions of Canada for all four simulations. Meanwhile, changes in the standard deviation are approximately -20% to +20%. The 50-year return period annual maximum wind speed, $v_{A0,50}$, is also expected to change between -20% to +20% in some areas of Canada, but most regions are within -8% to +8%. Strong spatial consistancy between the projected changes in the standard deviation and $v_{A0,50}$ is also evident. This demonstrates that the main cause of changes in $v_{A0,50}$ is the inter-annual variability of the annual maximum wind speed. Additionally, there is significant variation in the expected changes to the standard deviation both spatially and amongst the different simulations, which is also reflected in the 50-year return levels. This variation demonstrates that the driving GCM and the emissions scenario cause significant uncertainty in the results. There is notably less spatial variability in the mean wind speed, which leads Jeong and Sushama (2018) to conclude that "extreme wind speed might be influenced more by regional-scale features associated

with instantaneous surface temperature and air pressure gradients and many other similar effects". Although the results of the simulations are inconsistent, general increases in $v_{A0,50}$ are evident in central and eastern Canada. Simulations of the future mean sea level pressure (MSLP), not shown in the figure, demonstrate that these increases in $v_{A0,50}$ are caused by changes in MSLP and assocatiated changes in the MSLP gradient, which "can increase/decrease intensities of low/high pressure systems", leading to changes in future wind speeds (Jeong and Sushama, 2018). While an increasing trend in $v_{A0,50}$ is evident, projected changes in the annual maximum wind speed are generally statistically insignificant based on the two sample t-test at the 10% significance level (Jeong and Sushama, 2018). Jeong and Sushama (2018) also contribute to the ongoing debate on the value addition of downscaling, finding that downscaling did add some value in reproducing historical observed magnitudes and spatial patterns of seasonal and annual mean wind speed.

Jeong and Sushama (2019) completed a similar study to Jeong and Sushama (2018), but enhanced their analysis to cover all of North America using a different RCM, the Global Environmental Multiscale (GEM) model, which is used by Environment and Climate Change Canada (ECCC). Jeong and Sushama (2019) also expanded their analysis to include a study on future changes in the mean, coefficient of variation (CV), and 50-year return period annual maximum wind gust, in addition to that of the annual maximum wind speed. The GEM model uses a physical approach to estimate wind gusts, which assumes wind gusts occur due to the transportation of air particles to the surface of the boundary layer through turbulent eddies (Jeong and Sushama, 2019). Similar to Jeong and Sushama (2018), Jeong and Sushama (2019) used 3-hourly simulation observations to evaluate the annual maximum wind speed. However, hourly data were used for the wind gust analysis because a higher temporal resolution is required for robust wind gust results. Jeong and Sushama (2019) estimated the 50-year return period annual maximum wind speed and gust by fitting the Gumbel distribution using the MOM. They evaluated the simulation results over the period 2011-2100, but found relatively small changes for the near future periods, and therefore mainly present results for the future 2071-2100 period with respect to the current 1981-2010 period. The same time periods are used by Jeong and Sushama

(2018). Figure 2.2 shows Jeong and Sushama's (2019) simulation results of the projected changes in the mean, CV, and 50-year return period of the annual maximum wind speed, as well as the MSLP gradient. Note that "Can" and "MPI" denote using the CanESM2 and MPI-ESM as the GCM in the given simulation, respectively.

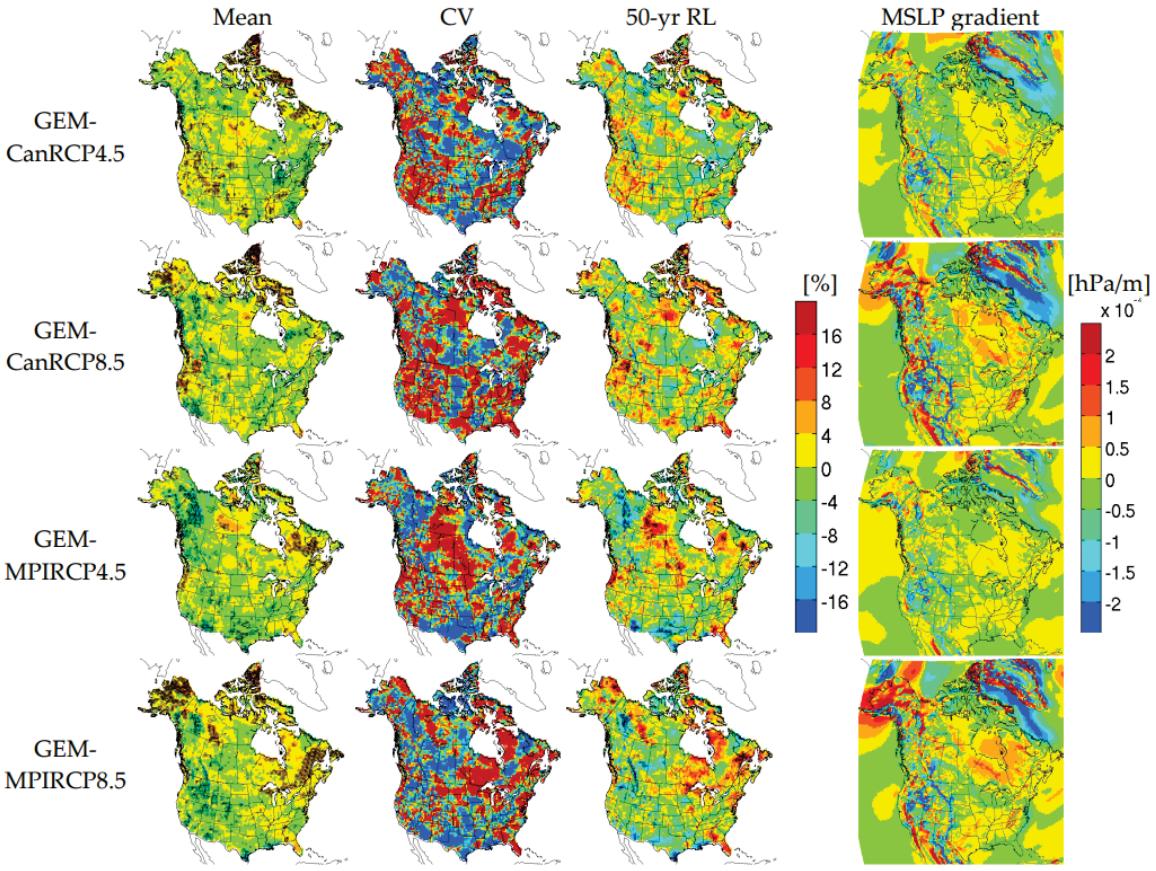

Figure 2.2: Projected changes to the mean, coefficient of variation (CV), and 50-year return period of the annual maximum wind speed for the future 2071–2100 period with respect to the current 1981–2010 period. Projected changes to annual MSLP gradient are provided in the fourth column (Jeong and Sushama, 2019).

As Fig. 2.2 demonstrates, the results over Canada are almost identical to the results of Jeong and Sushama (2018). This suggests that the RCM has less of an effect on the variability between simulations than the GCM and emissions scenario. The results also further emphasize Jeong and Sushama's (2018) conclusion that increased inter-annual variability, as demonstrated by the CV, is the main cause of increases in $v_{A0,50}$. The right column in Fig. 2.2 shows that changes in the MSLP gradient coincide with extreme wind speeds, specifically in GEM-CanRCP8.5 and GEM-MPIRCP8.5 over

western Alaska and Hudson Bay coastal regions (Jeong and Sushama, 2019). These cases reiterate Jeong and Sushama's (2018) hypothesis that changes in the MSLP gradient may lead to future extreme wind speeds (Jeong and Sushama, 2019). Although, the increased inter-annual variability may also be due to quasi-periodic internal variability in the climate system, which is caused by large-scale climate oscillations (e.g., the North Atlantic Oscillation) (Jeong and Sushama, 2019).

Figure 2.3 shows the mean, CV, and 50-year return period of the annual maximum wind gust, as well as the gust factor. In Jeong and Sushama's (2019) analysis, the gust factor is defined as the ratio of the 50-year return period annual maximum wind gust speed to the 50-year return period annual maximum wind speed. This is considered a valid estimate because the wind gust varies according to a stationary normal distribution about the longer duration average wind speed (see Section 1.3.4). Therefore, the annual maximum wind gust is likely to occur at the same time as the annual maximum wind speed. Recall from Section 1.3.4 that this gust factor defined by Jeong and Sushama (2019) is equal to G, and not the gust effect factor, C_g. The first row in Fig. 2.3 shows the observations, while rows two and three show two GEM simulations for the 1981-2010 period, driven by the ERA-Interim reanalysis dataset, and CanESM2 (i.e., GEM-ERA and GEM-CanHist, respectively). Rows four and five show the percent increases for the future 2071-2100 period with respect to the current 1981-2010 period.

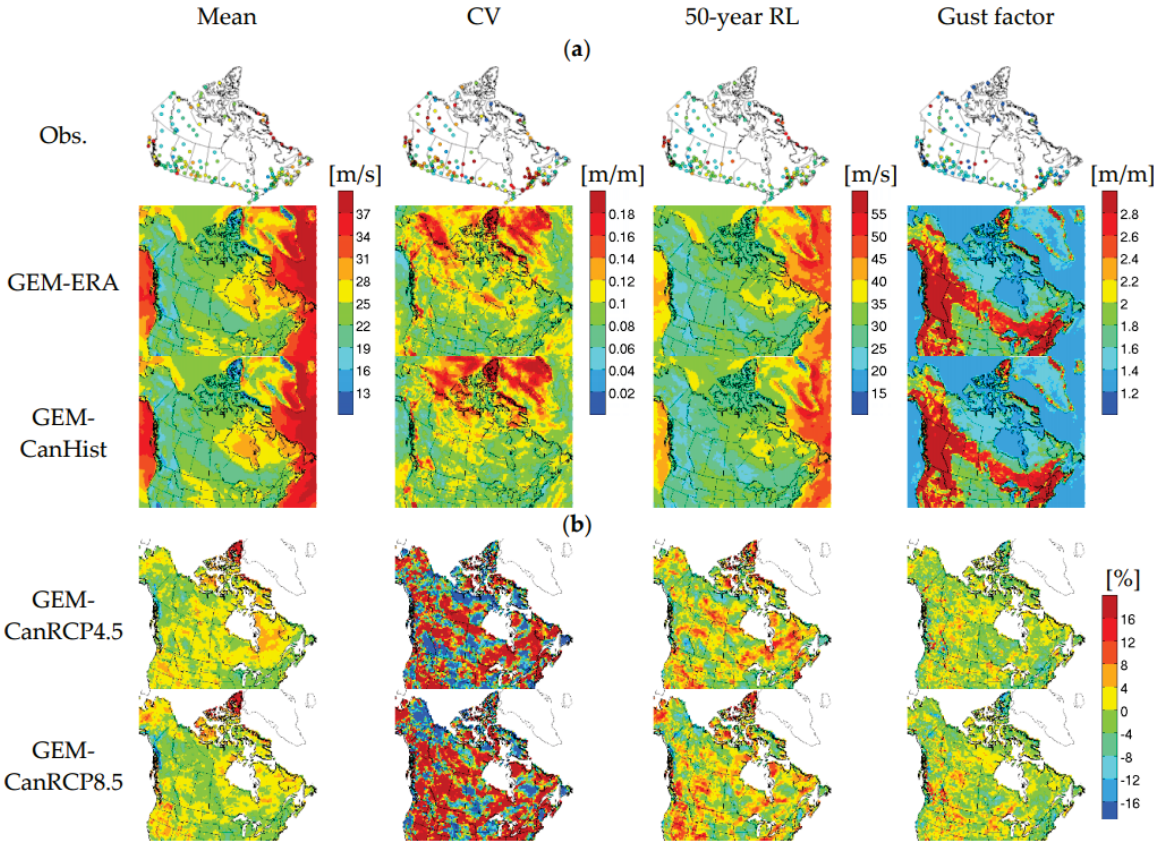

Figure 2.3: (a) Mean, coefficient of variation (CV), and 50-year return period annual maximum wind gust, as well as gust factor (the ratio of the 50-year return period annual maximum wind gust to the 50-year return period annual maximum wind speed), for observations and two GEM model simulations (i.e., GEM-ERA and GEM-CanHist), for the 1981–2010 period. (b) Projected changes to the same characteristics as shown in (a) for the future 2071–2100 period with respect to the current 1981–2010 (Jeong and Sushama, 2019).

The current period results (i.e., GEM-ERA and GEM-CanHist) demonstrate that the spatial distribution of the mean annual maximum wind gust is simulated well relative to the observed data (Jeong and Sushama, 2019). Meanwhile, the simulated CV magnitude and spatial variability are underestimated relative to the observed data for the same time period, especially in southern Canada (Jeong and Sushama, 2019). Jeong and Sushama (2019) attribute this underestimated spatial variability to missing data and observation error in the observation dataset, while underestimated CV values may be due to "underrepresented inter-annual variability in the model". The 50-year return period wind gusts are also underestimated as a consequence of the low CV values (Jeong and Sushama, 2019). The gust factor is notably higher in the

western mountainous and boreal forest regions compared to the rest of Canada (Jeong and Sushama, 2019). This may be caused by lower wind speeds due to a higher canopy height and roughness length in forested areas, or general underestimation of $v_{A0,50}$ in these areas (Jeong and Sushama, 2019). The value of the gust factor in western mountainous and boreal forest regions is approximately 2.8, which is significantly higher than the gust factor used by the NBCC (i.e., $\sqrt{2} \approx 1.41$). However, the gust factor over the rest of Canada is generally below 2, as well as the majority of the observed data gust factors. This suggests that the model is likely underestimating the wind speed in these forested areas, leading to overestimated gust factors. Despite the overestimation, projected percent changes in the gust factor should still be valid, as the error should be consistent across both time periods. Projected changes in the gust factor due to the climate change are in the range of -12% to +12%, and show similar results under both RCP 4.5 and 8.5.

Kumar et al. (2015) completed a global analysis using GCMs included in the CMIP5 to assess changes in extreme wind speeds under RCP8.5. As discussed, Kumar et al. (2015) chose not to downscale the GCM results because the authors believe there is a higher value-addition in using a larger ensemble of GCMs to encapsulate the variability in projections, than in downscaling a few GCMs to model climate change effects at the regional and local scale. Outputs of 15 GCMs were used for the analysis, but the results were mainly presented for the multimodel ensemble (MME) mean (Kumar et al., 2015). Kumar et al. (2015) assessed future changes for the 2074-2100 period relative to the historical 1979-2005 reference period (Kumar et al., 2015). Figure 2.4 shows the MME mean 25-, 50-, and 100-year annual maximum wind speed for the 1979-2005 period, as well as the projected change in the MME mean 25-, 50-, and 100-year return period for the 2074-2100 period relative to the reference period. The results are presented in $\mathrm{m\,s^{-1}}$.

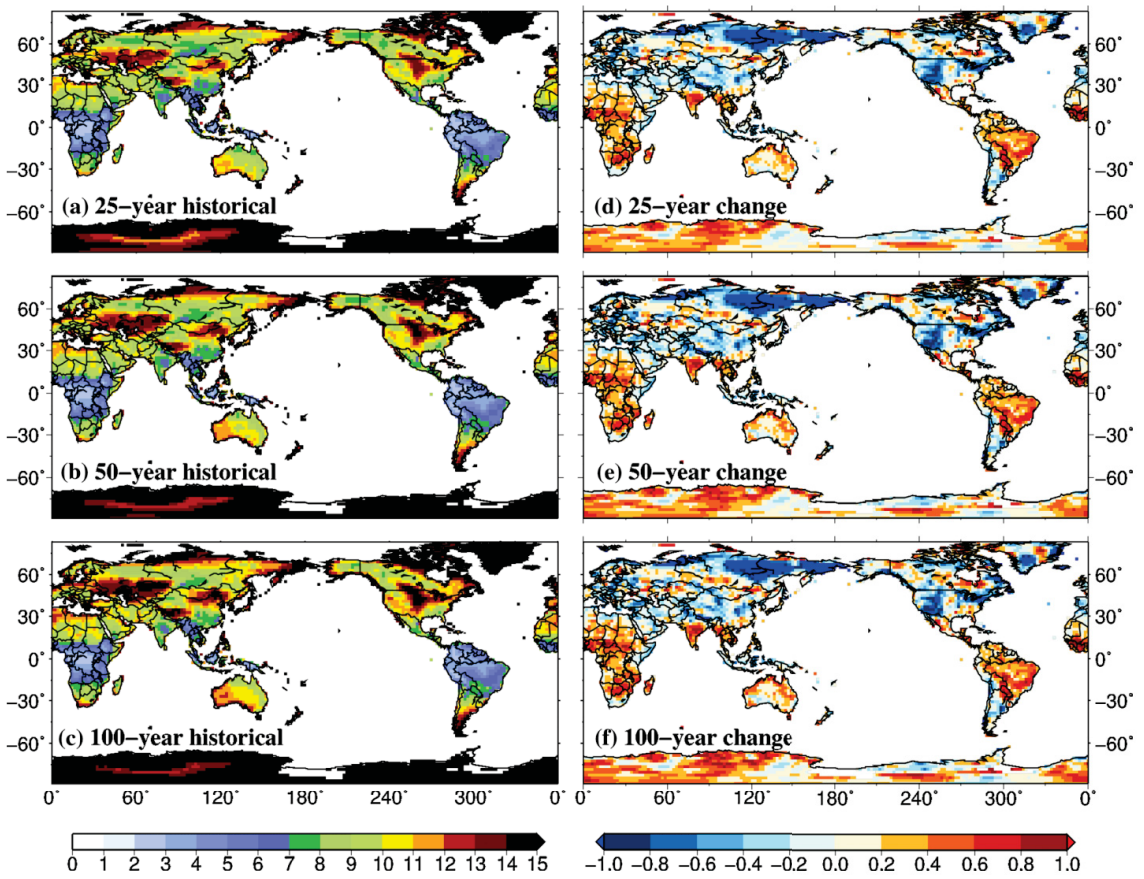

Figure 2.4: (a)–(c) The multimodel ensemble mean of annual maximum wind speeds at 25, 50, and 100-year return periods for the period of 1979– 2005. (d)–(f) MME change in projected extreme wind speeds at 25–100 year return periods (in $\mathrm{m\,s^{-1}}$) (Kumar et al., 2015).

Figure 2.4 shows that the reference period values across Canada are underestimated relative to the values determined by Hong et al. (2014*a*) for the NBCC. This is consistent with what Kumar et al. (2015) found when validating the models. Kumar et al. (2015) compared the results to the ERA reanalysis dataset, as a reliable observed global dataset does not exist. They found a small negative bias in the simulated annual maximum wind speed relative to that of ERA across most regions. This negative bias may be due to the lack of downscaling. In contrast, a relatively strong positive bias, approximately $5\,\mathrm{m\,s^{-1}}$, was found for the mountainous regions of the Himalayas, the Rocky Mountains, the Andes, and Siberia (Kumar et al., 2015). This contradicts Jeong and Sushama (2019), who found that the annual maximum wind speed was underestimated in mountainous regions and this contradiction highlights

the variability in GCM projections. Additionally, Fig. 2.4 shows that the projected change in the 50-year change in the annual maximum wind speed is within -10% to +10% across Canada, which is similar to what Jeong and Sushama (2018) and Jeong and Sushama (2019) found. Although, modelling uncertainties cause the results to be spatially inconsistent (i.e., the same location shows an increase and decrease in different models).

Given the uncertainty in extreme wind speed projections, it is difficult to determine the effects of climate change on the wind speed parameters used for structural design (i.e., the annual maximum wind speed distribution and the gust factor). Nonetheless, the above studies provide good estimates that can be combined with the uncertainties provided in Section 2.4 to model how structural design values should be updated to account for the effects of climate change. Based on the above studies it can be concluded that for most regions of Canada the annual maximum wind speed mean is likely to increase 4% over the next 50 years, although, in some locations the mean may increase up to 8%. The maximum change in annual maximum wind speed standard deviation is estimated to be 20% over the next 50 years across all regions. Meanwhile, the gust factor, G, is expected to increase 12% over the same time period across most regions of Canada, and up to 20% for some regions of the west coast. The total uncertainty in each of these estimates is between 45% and 125%, as the emissions scenario uncertainty is approximately 15-50% and the model formulation uncertainty is approximately 30-75% (see Section 2.4). Therefore, to be conservative the projected changes in the mean and standard deviation of the annual maximum wind speed should be increased by between 50 and 125%. Since the projected changes are poorly known, a parametric analysis is completed in this thesis, which demonstrates the change in the structural design parameters for various cities across Canada based on a range of possible increases in the mean and standard deviation of the current annual maximum hourly-average wind speed.

Chapter 3

Load Factor Design Methodology

3.1 General

The objective of Chapter 3 is to assess the current structural design methods used in Canada for buildings under wind loading, and to update the wind loading parameters such that the current exceedance probability level is maintained under climate change. The effect climate change on the gust effect factor is also analysed. As discussed in Section 1.2, both the CHBDC and the NBCC currently use the Load and Resistance Factor Design (LRFD) methodology. The LRFD methodology is a probabilistic approach to structural design that aims to achieve a target level of reliability, or probability of failure, across all loading scenarios. Each type of load/resistance is considered separately, and an individual factor is applied to each load/resistance that accounts for the uncertainty in the given component. The load factors are calibrated based on the statistical distributions of each load, as well as the target reliability level. Consequently, more variable load components, such as wind loads, have higher load factors. The current wind load factor used in the NBCC is $\alpha_W = 1.4$, see eq. (1.2) (NRCC, 2015). The wind load factor was calibrated using a 50-year design life and target reliability index of 3.0 (i.e., a target probability of failure of 1.35×10^{-3}) (Hong et al., 2016). As discussed in Section 1.3, the characteristic wind load, $\hat{F}_W$ (see eq. 1.4), used in the NBCC is equal to the product of the 50-year return period annual maximum one-hourly average wind pressure, $q_{A1,50}$, the gust effect factor, C_g, and several other factors relating to the size, shape, location and importance of the building.

The current wind load design values specified in the NBCC have been developed to account for current wind loading uncertainties including those of the wind speed, pressure coefficient, exposure factor, gust effect factor, and topographic factor. Wind speed is by far the most important parameter in estimating $\hat{F}_W$, as it contributes to 70-80% of the uncertainty in $\hat{F}_W$ (Vickery et al., 2010). Wind speed uncertainty

is significantly higher than other sources of uncertainty since $\hat{F}_W \propto q_{A1,50} \propto v^2_{A1,50}$, and so the uncertainty in the design wind speed, $v_{A1,50}$ is doubled (using a first-order approximation). Additionally, there is significant uncertainty in estimates of $v_{A1,50}$ due to uncertainty in the data and in the probabilistic modelling process. Sources of uncertainty in the data include sampling errors due to relatively short records, low spatial resolution due to limited meteorological stations, and changes in sampling procedures over time, the latter of which might have been quite arbitrary (Lombardo and Ayyub, 2017). Uncertainties resulting from the probabilistic modelling process include using short data records to estimate much longer return period wind speeds, using a single extreme value model across several locations, and disregarding the phenomenological cause of extreme winds (e.g., tornado, thunderstorm, extra-tropical storm, etc.), which are represented by different probability distributions (Lombardo and Ayyub, 2017).

All current sources of wind loading uncertainties, excluding climate change, are considered to be accounted for in the NBCC wind loading parameters, α_W and $\hat{F}_W$, as the current NBCC is deemed acceptable by society. The aim of this chapter then is not to adjust the current target reliabilities, but to find wind loading design values which achieve the same target reliabilities over the design lifetime in the face of climate change. Specifically, the objective of this chapter is to determine updated values of α_W and $\hat{F}_W$ such that the exceedance probability remains constant in the future under climate change. The exceedance probability is the probability that the factored design wind load, $\alpha_W \hat{F}_W$, is exceeded over the design life of the structure. Note that if the factored design wind load is selected to have a constant exceedance probability, and if the distributions of the resistance and other load types are independent of the design wind load, then the actual reliability index will be maintained at current levels. Therefore, as stated in Section 1.2.1, the load factor calibration based on exceedance probability is assumed to achieve target system reliability levels as determined by Bartlett et al. (2003*a*).

3.2 Current Design Wind Speed Statistical Information

As discussed in Section 3.1, the most important parameter used to determine the characteristic wind load, $\hat{F}_W$, is the 50-year return period annual maximum one-hourly average wind speed, $v_{A1,50}$. The design wind speeds used in the NBCC were most recently updated for the 2010 edition of the building code, and were determined by fitting the Gumbel distribution to the annual maximum one-hourly average wind speed using the method of moments (MOM) (NRCC, 2015). The dataset used to determine $v_{A1,50}$ consisted of one-hourly average wind speed data from 135 stations, as well as one or two minute average wind speeds, or ten minute average wind speeds recorded once per hour at the top of each hour from 465 stations (NRCC, 2015). Each station had between 10 and 54 years of data, and the wind speed measurements were adjusted to represent a one hour average at 10 m above ground (the standard anemometer height), and to account for differences in surface roughness (NRCC, 2015). The methods used to adjust the wind speed records were not provided by NRCC (2015).

While the design wind speeds used in the NBCC have not been updated since 2010, Hong et al. (2014*a*) determined values of $v_{A1,50}$ based on wind speed records from the Environment Canada (EC) HLY01 archive, which consists of one, two or ten minute average wind speed measurements recorded just before the top of the hour at 235 stations across Canada. They found that the annual maximum of these short duration wind speed averages is a "reasonable conservative" estimate of the annual maximum one-hourly average wind speed (Hong et al., 2014*a*). This conclusion is consistant with the results in Fig. 1.5, which show that the variance of the two min average wind speed is only approximately 6.4% greater than the variance of one hour average wind speed. Hong et al. (2014*a*) only used stations with a minimum of 20 years of data, and found that fitting these annual maximum one-hourly average wind speed estimates to the Gumbel distribution using the generalized least-squares (GLS) method provided the best estimate of $v_{A1,50}$. Columns 1-5 of Table 3.1 show the scale and location parameters of the Gumbel distribution, as well as $v_{A1,50}$ for 14 Canadian cities determined by Hong et al. (2014*a*). Column 6 of Table 3.1 shows the 50-year return period annual maximum one-hourly average wind speed given in the NBCC, v_{NBCC}, at the closest location to that in column 1. Finally, column 7 shows the percent

difference between $v_{A1,50}$ and v_{NBCC}, $\%D_v$. That is, $\%D_v = \frac{v_{A1,50} - v_{NBCC}}{v_{NBCC}} \cdot 100\%$.

Table 3.1: Wind speed statistics for 14 Canadian meteorological stations (i.e.,$u_{v_{A1}}$, $a_{v_{A1}}$ and $v_{A1,50}$) determined by Hong et al. (2014a) (Hong, H. P. 2020, personal communication, 5 May), as well the 50-year return period annual maximum one-hourly average wind speed given in the NBCC (v_{NBCC}) and the percent difference between $v_{A1,50}$ and v_{NBCC}, $\%D_v$.

Location	Province	$u_{v_{A1}}$	$a_{v_{A1}}$	$v_{A1,50}$	v_{NBCC}	$\%D_v$
Victoria Int'l A	BC	57.2	6.94	84.3	106.9	26.8
Whitehorse A	YT	52.5	7.09	80.2	124.9	55.8
Yellowknife A	NT	48.7	5.59	70.5	87.1	23.6
Iqaluit A	NU	71.8	12.05	118.8	97.2	-18.2
Edmonton Int'l A	AB	58.5	5.92	81.6	108.0	32.4
Regina Int'l A	SK	71.9	6.85	98.6	95.0	-3.6
Winnipeg Int'l A	MB	63.9	5.56	85.6	99.0	15.7
Ottawa Int'l A	ON	62.7	6.80	89.2	95.0	6.5
Toronto Int'l A	ON	73.1	6.58	98.8	90.7	-8.2
Quebec Int'l A	QC	64.9	6.80	91.4	94.0	2.8
Fredericton A	NB	57.0	4.81	75.8	90.7	19.7
Halifax Int'l A	NS	69.3	9.26	105.4	87.1	-17.4
Charlottetown A	PE	67.6	6.71	93.8	108.0	15.2
St. John's A	NL	87.0	8.40	119.8	105.8	-11.6

Table 3.1 shows that there is a relatively large difference between $v_{A1,50}$ and v_{NBCC} for some locations. Hong et al. (2014a) found this large discrepancy to be a concern, "especially if a location in the NBCC table is within 5 km from a meteorological station whose [$v_{A1,50}$] can be estimated with confidence". The parameters determined by Hong et al. (2014a) are considered by the author to be more accurate than the NBCC values due to lower sampling error resulting from a higher minimum number of years of data (i.e., 20 years vs. 10 years), and because the GLS method was employed which results in a more accurate estimate of $v_{A1,50}$ relative to using the MOM (Hong et al., 2014a). Therefore, $u_{v_{A1}}$, $a_{v_{A1}}$ and $v_{A1,50}$, derived from Hong et al. (2014a) and as reported in Table 3.1, are the parameters used in this thesis.

3.2.1 Factored Design Wind Speed Exceedance Probabilities

The NBCC provides site-specific 1-in-50 year reference wind velocity pressures, $q_{A1,50}$, that are to be used with a calibrated load factor of 1.4. Wind pressure is proportional

to wind velocity squared, therefore, the factored design wind speed is given as, $v_{FD} = \sqrt{1.4}v_{A1,50}$. The annual probability that v_{FD} is exceeded, $p_{v_{FD}}$, is then

$$p_{v_{FD}} = P[V_{A1} > v_{FD}] = 1 - F_{V_{A1}}(v_{FD}) = 1 - F_{V_{A1}}(\sqrt{1.4}v_{A1,50}) \tag{3.1}$$

The design wind speeds given in Table 3.1 were used to determine the factored design wind speed and the annual probability that v_{FD} is exceeded. The results are given in Table 3.2

Table 3.2: Factored design wind speed and annual probability that v_{FD} is exceeded for 14 Canadian cities under current (2015) design assumptions.

City	**Province**	v_{FD}	$p_{v_{FD}}$
Victoria Int'l A	BC	99.7	2.2e-03
Whitehorse A	YT	94.9	2.5e-03
Yellowknife A	NT	83.4	2.0e-03
Iqaluit A	NU	140.6	3.3e-03
Edmonton Int'l A	AB	96.5	1.6e-03
Regina Int'l A	SK	116.7	1.4e-03
Winnipeg Int'l A	MB	101.3	1.2e-03
Ottawa Int'l A	ON	105.6	1.8e-03
Toronto Int'l A	ON	116.9	1.3e-03
Quebec Int'l A	QC	108.2	1.7e-03
Fredericton A	NB	89.6	1.1e-03
Halifax Int'l A	NS	124.7	2.5e-03
Charlottetown A	PE	111.0	1.6e-03
St. John's A	NL	141.7	1.5e-03

Table 3.2 demonstrates that there is significant variability in $p_{v_{FD}}$ between locations. For example, the minimum $p_{v_{FD}}$ is 1.1e-03 in Fredericton, NB, while the maximum $p_{v_{FD}}$ is three times greater at 3.3e-03 in Iqaluit, NU. Consequently, the structural reliability levels also likely vary between locations across Canada under current conditions.

While there is significant variability in the current exceedance probabilities across Canada, all $p_{v_{FD}}$ results given in Table 3.2 are considered acceptable by society. Therefore, the range of $p_{v_{FD}}$ values in Table 3.2 is used to define three annual exceedance probability targets that are used in this thesis to determine updated wind loading design parameters that account for climate change. The three target annual exceedance probabilities, p_e, are 1e-03, 2e-03 and 3e-03, where 3e-03 is considered

to be the maximum acceptable exceedance probability, 1e-03 is considered to be a conservative target, and 2e-03 is a mid-level exceedance probability target.

The variation in exceedance probabilities between locations is further emphasized by analysing the 50-year lifetime exceedance probability, p_{50}. Assuming independence between years, the probability that a wind speed speed with a given annual exceedance probability, p, is exceeded over a 50-year lifetime is

$$p_{50} = 1 - (1 - p)^{50} \tag{3.2}$$

The blue bars in Figure 3.1 show p_{50} evaluated at each of the 14 locations included in Table 3.1 (i.e., $1 - (1 - p_{v_{FD}})^{50}$). The green, orange, and red lines show the value of p_{50} evaluated at the three annual exceedance probability targets, 1e-03, 2e-03 and 3e-03, respectively.

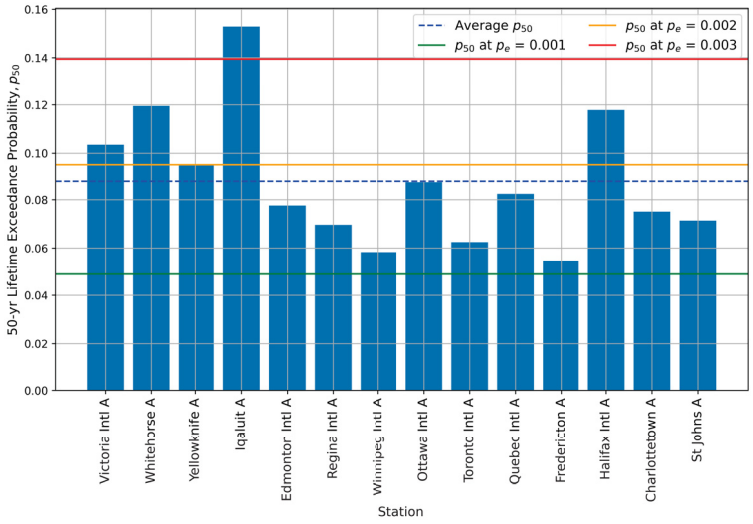

Figure 3.1: Probability that the factored design wind speed, v_{FD}, is exceeded in the 50-year lifetime for 14 Canadian cities.

Figure 3.1 shows that the majority of the 14 locations have exceedance probabilities well under the maximum and mid-level target exceedance probabilities. However, at the Victoria, Whitehorse, Yellowknife, Iqaluit and Halifax stations p_{50} is significantly higher than that of the other locations. Iqaluit even exceeds the maximum target value for p_{50} (i.e., p_{50} evaluated at $p_e = 3e-3$). Inconsistent exceedance probabilities across the 14 locations is a result of a constant load factor (1.4) being used for all locations across Canada, while the variability of the annual maximum wind speed changes. This problem along with the proposed solution is discussed in Chapter 4.

3.3 Effect of Climate Change on Wind Design Requirements

The mean and standard deviation of the annual maximum one-hourly average wind speed are expected to increase in the future due to climate change, as discussed in Chapter 2. Additionally, the uncertainty in these distribution parameters is also expected to increase. This section analyses how α_W and $\hat{F}_W$ need to be updated to account for these changes. Determining updated design values for the NBCC is important because, as shown in Section 1.4.2, the current value of $v_{A1,50}$ will almost certainly be exceeded in any given year if the mean annual maximum one-hourly average wind speed increases by 50% relative to the current value. Note that the exceedance probability for the factored design wind speed is somewhat lower than that of $v_{A1,50}$ since $v_{FD} = \sqrt{1.4} v_{A1,50}$.

The method proposed in this chapter for updating the NBCC design wind speeds under the LRFD methodology is to increase both α_W and $\hat{F}_W$. The updated value of α_W will account for all current sources of uncertainty, as well as the increased variability in the annual maximum one-hourly average wind pressure, q_{A1}, due to climate change. Meanwhile, $\hat{F}_W$ is increased by adding a climate change effect factor, C_c (proposed herein), to eq. (1.4). The climate change effect factor, C_c, accounts for the projected increase in the mean of q_{A1} due to climate change. The resulting characteristic wind load is then given as

$$\hat{F}_W = I_W q_{A1,50} C_e C_t C_g C_p C_c \tag{3.3}$$

where all parameters except C_c are as defined in eq. (1.4). Note that, in this approach, the design wind pressure, $q_{A1,50}$, remains the same as in the current NBCC (2015). The updated factored design wind speed, accounting for climate change, is then

$$v_{FD,CC} = \sqrt{\alpha_W C_c} v_{A1,50} \tag{3.4}$$

where $v_{A1,50}$, remains at the current value.

Under climate change, the annual maximum one-hourly average wind speed is assumed to follow a non-stationary Gumbel distribution with a linearly increasing mean and standard deviation (see eq. 1.39), where the initial means and standard deviations are determined based on the current scale and location parameters for the 14 Canadian cities given in Table 3.1. The non-stationary mean and standard deviation

of the annual maximum one-hourly average wind speed, V_{A1}, can be written in terms of the projected annual change in the mean and standard deviation of V_{A1}, Δ_μ and Δ_σ, respectively, relative to their current values. That is, $\mu_{v_{A1}}(y) = \mu_{v_{A1}}(0)\left(1 + \Delta_\mu y\right)$ and $\sigma_{v_{A1}}(y) = \sigma_{v_{A1}}(0)\left(1 + \Delta_\sigma y\right)$.

Increases in the mean and variance of V_{A1}, due to climate change, are accounted for separately by C_c and α_W, respectively. Therefore, to determine C_c the scenario where only the mean of V_{A1} increases with time, and the variance of V_{A1} remains constant is considered. Let the design wind speed, $v_{A1,50,CC}$, be the 50-year return period annual maximum one-hourly average wind speed under a given climate change scenario defined by $\Delta_\mu > 0$ and $\Delta_\sigma = 0$. The climate change effect factor, C_c, is then defined in terms of $v_{A1,50,CC}$ as

$$C_c = \left(\frac{v_{A1,50,CC}}{v_{A1,50}}\right)^2 \tag{3.5}$$

where $v_{A1,50,CC}$ is evaluated based on the return period m_2, as defined in Section 1.4.2 (recall that m_2, which has an expected number of exceedances above the threshold r in m_2 years equal to one, was deemed to be the best measure of return period). Since ρ_{air} is assumed constant under climate change at any specific elevation, C_c, which is squared ratio of $v_{A1,50,CC}$ to $v_{A1,50}$, can be interpreted as the increase in $q_{A1,50}$ due to the projected increase in the mean of V_{A1} under climate change.

Similarly, to determine the updated value of α_W, the scenario where the variance of V_{A1} increases with time, and the mean of V_{A1} remains constant can be used. The design wind speed, $v_{A1,50,CC}$, is now evaluated based on a given climate change scenario with $\Delta_\mu = 0$ and $\Delta_\sigma > 0$. The load factor, α_W, can then also be defined in terms of $v_{A1,50,CC}$ as

$$\alpha_W = 1.4\left(\frac{v_{A1,50,CC}}{v_{A1,50}}\right)^2 \tag{3.6}$$

where $v_{A1,50,CC}$ is again evaluated using the return period m_2, as defined in Section 1.4.2. The squared ratio of $v_{A1,50,CC}$ to $v_{A1,50}$ accounts for the increase in $q_{A1,50}$ due to the projected increase in the standard deviation of V_{A1} under climate change, while, the factor 1.4 accounts for the current sources of uncertainty.

Figure 3.2(a) shows C_c evaluated at each of the 14 Canadian cities listed in Table 3.1 for $\Delta_\mu = 0.001$, 0.002, 0.003, and 0.004 and $\Delta_\sigma = 0$. The corresponding

dashed lines show the average value of C_c over the 14 locations for each scenario. Figure 3.2(b) shows the average value over the 14 locations for $0.0 \leq \Delta_\mu \leq 0.005$ and $\Delta_\sigma = 0$. The values of Δ_μ used to determine C_c in Fig. 3.2 were selected based on the studies described in Section 2.5.

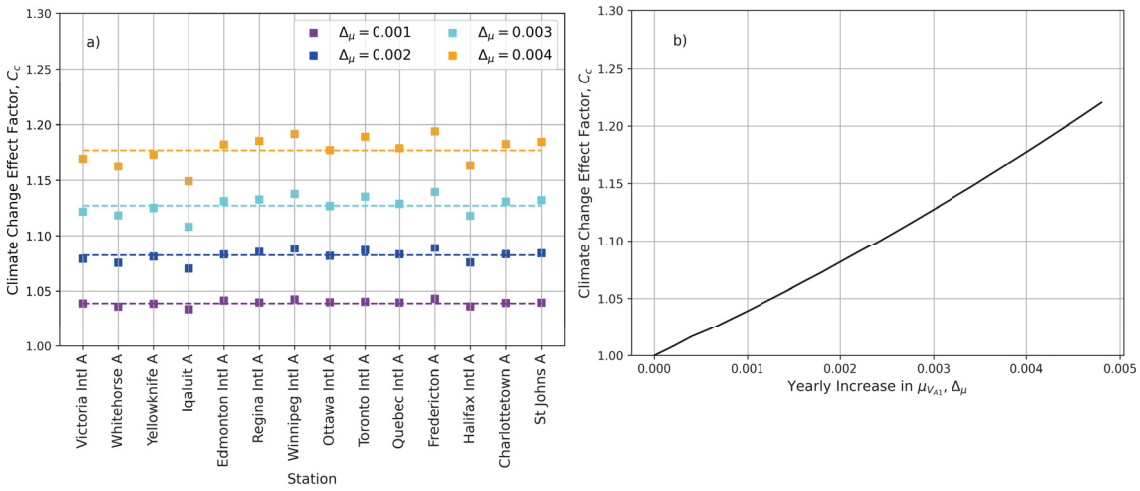

Figure 3.2: Climate change effect factor, C_c, required to maintain the current exceedance probability under climate change for varying Δ_μ and $\Delta_\sigma = 0$ (a) at each of the 14 Canadian cities and (b) on average, over the 14 stations.

Similarly, Fig. 3.3(a) shows α_W evaluated at each of the 14 Canadian cities in Table 3.1 for $\Delta_\mu = 0$ and $\Delta_\sigma = 0.004$, 0.006, 0.008, and 0.01. The average values of α_W over the 14 locations are shown as the corresponding dashed lines in Fig. 3.3(a), and Fig. 3.3(b) shows the average value of α_W for $\Delta_\mu = 0$ and $0.0 \leq \Delta_\sigma \leq 0.01$. The values of Δ_σ used to determine α_W in Fig. 3.3 were also selected on the basis of the results presented in Section 2.5.

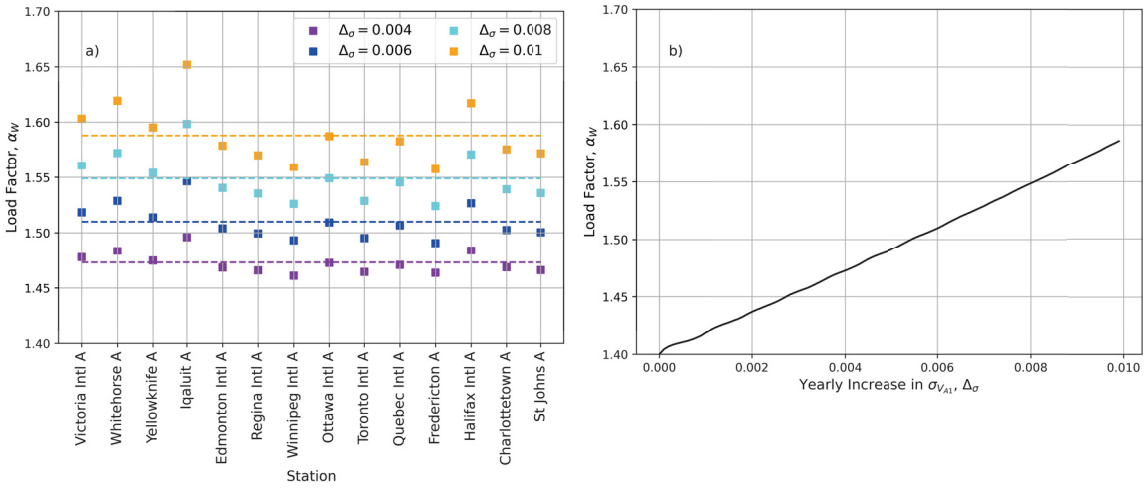

Figure 3.3: Load factor, α_W, required to maintain the current exceedance probability under climate change for varying Δ_σ and $\Delta_\mu = 0$ (a) at each of the 14 Canadian cities and (b) on average, over the 14 stations.

Figures 3.2 and 3.3 demonstrate that, for small increases in μ_{VA1} and σ_{VA1}, C_c and α_W are relatively consistent across all 14 Canadian cities. However, as Δ_μ and Δ_σ increase, the variability in C_c and α_W between locations also increases (i.e., the variance of the yellow dots is greater than that of the purple dots). This observation suggests that constant C_c and α_W design values cannot achieve constant reliability targets across the country. While reliability is inconsistent across Canada under current conditions, Figs. 3.2 and 3.3 demonstrate that the variation between locations will increase under climate change if constant values of C_c and α_W are adopted across Canada. As mentioned above, this problem and the proposed solution is discussed in Chapter 4.

To determine the most appropriate values for C_c and α_W, studies of state-of-the-art extreme wind speed projections in Canada under climate change (see Section 2.5) must be considered. Jeong and Sushama (2018) showed that for most regions of Canada the annual maximum wind speed mean is likely to increase by about 4% over the next 50 years, although, in some locations the mean may increase by up to about 8%. The maximum change in annual maximum wind speed standard deviation is estimated to be about 20% over the next 50 years across all regions. Two climate change cases are considered in this section based on these conclusions: case 1, $\Delta_\mu = 0.04/50 = 0.0008$ and $\Delta_\sigma = 0.20/50 = 0.004$, and case 2, $\Delta_\mu = 0.08/50 = 0.0016$

and $\Delta_\sigma = 0.004$. Note that there is significant uncertainty in these projections due to model formulation and uncertainty in the emissions scenario, the latter of which is dependent on human behaviour (see Section 2.4). Based on the studies discussed in Section 2.4, the expected uncertainty in these annual maximum wind speed projections is between 50% and 125%. Meaning that, the true values of Δ_μ and Δ_σ could be as much as 125% greater than the proposed values. A climate change model uncertainty factor, u_{CC}, is introduced to adjust the Δ_μ and Δ_σ values to account for this uncertainty. That is, $\Delta_\mu = 0.0008u_{CC}$ for case 1, $\Delta_\mu = 0.0016u_{CC}$ for case 2, and $\Delta_\sigma = 0.004u_{CC}$ for both cases, where, for example, if there is a 50% model uncertainty in the wind speed projections then $u_{CC} = 1.5$. Note that, in this example, Δ_μ is increased by 50% to include model uncertainty, therefore, $\Delta_\mu = 0.0008(1.5)$, for climate change case 1.

Considering the results of climate change case 1 first: the lower bound of the uncertainty range, 50% (i.e., $u_{CC} = 1.5$ resulting in $\Delta_\mu = 0.0008(1.5) = 0.0012$ and $\Delta_\sigma = 0.004(1.5) = 0.006$), led to $\alpha_W = 1.510$ (see Fig. 3.2b), and $C_c = 1.047$ (see Fig. 3.3b). The upper bound of the uncertainty range, 125% (i.e., $u_{CC} = 2.25$, resulting in $\Delta_\mu = 0.0008(2.25) = 0.0018$ and $\Delta_\sigma = 0.004(2.25) = 0.009$), led to $\alpha_W = 1.568$ (see Fig. 3.2b), and $C_c = 1.072$ (see Fig. 3.3b).

Under climate change case 2, α_W is equivalent to that of case 1, since Δ_σ is the same in both scenarios. For an uncertainty of 50% (i.e., $\Delta_\mu = 0.0016(1.5) = 0.0024$), $C_c = 1.099$, while $C_c = 1.157$ assuming 125% uncertainty (i.e., $\Delta_\mu = 0.0016(2.25) = 0.0036$).

For simplicity, the wind loading design parameters, C_c and α_W, are determined by considering increases in $\mu_{V_{A1}}$ and $\sigma_{V_{A1}}$ separately (see Figs. 3.2 and 3.3). However, it is likely that the mean and variance of V_{A1} will increase simultaneously under climate change, resulting in a discrepancy between $v_{FD,CC}$ calculated using C_c and α_W as defined in Figs. 3.2 and 3.3, and $v_{FD,CC}$ determined when increases in $\mu_{V_{A1}}$ and $\sigma_{V_{A1}}$ are considered simultaneously. The magnitude of this discrepancy is assessed by calculating the difference between $\alpha_W C_c$ and $1.4\left(\frac{v_{A1,50,CC}}{v_{A1,50}}\right)^2$, where $v_{A1,50,CC}$ is determined for $\Delta_\mu > 0$ and $\Delta_\sigma > 0$, and the same values of Δ_μ and Δ_σ are used to determine $v_{A1,50,CC}$, α_W and C_c. The maximum difference was found for case 2, assuming 125% uncertainty (i.e., $u_{CC} = 2.25$), where $\alpha_W C_c$ was 0.007 (or 0.4%) less

than $1.4\left(\frac{v_{CC,A1,50}}{v_{A1,50}}\right)^2$. The minimum difference was found for case 1, assuming 50% uncertainty, where $\alpha_W C_c$ was 0.002 (or 0.15%) less than $1.4\left(\frac{v_{A1,50,CC}}{v_{Asimultaneously1,50}}\right)^2$. In other words, considering increases in $\mu_{V_{A1}}$ and $\sigma_{V_{A1}}$ separately, instead of simultaneously, results in the factored design wind load, $\alpha_W \hat{F}_W$, being underestimated by or 0.4% under the most extreme climate change case used in this thesis. Therefore, this discrepancy is considered negligible for the purpose of determining C_c and α_W.

Based on these results, four sets of values of C_c and α_W are proposed; values of C_c and α_W are proposed for a model uncertainty of both 50% and 125%, under both climate change cases 1 and 2. For climate change case 1, which is appropriate for most regions of Canada, $C_c = 1.05$ and $\alpha_W = 1.55$ should be implemented to maintain the current reliability levels over the next 50 years, assuming 50% model uncertainty in extreme wind speed projections, while $C_c = 1.1$ and $\alpha_W = 1.6$ should be implemented if 125% model uncertainty assumed.

Under climate change case 2, which includes regions expecting a greater increase in the mean annual maximum wind speed, such as Quebec and Nunavut (see Fig. 2.1), $C_c = 1.15$ and $\alpha_W = 1.55$ should be implemented assuming 50% model uncertainty. In these regions, increased values of $C_c = 1.2$ and $\alpha_W = 1.6$ might be appropriate if model uncertainty is as high as 125%.

The updated factored design wind speed accounting for climate change, $v_{FD,CC}$ (see eq. 3.4), in the LRFD format can be determined using the aforementioned values of C_c and α_W. Figure 3.4 shows a comparison of the current factored design wind speed, v_{FD}, and the future factored design wind speed under climate change, $v_{FD,CC}$. Figure 3.4(a) shows the proposed case 1 design values for 50% and 125% model uncertainty, and Fig. 3.4(b) shows the same for case 2.

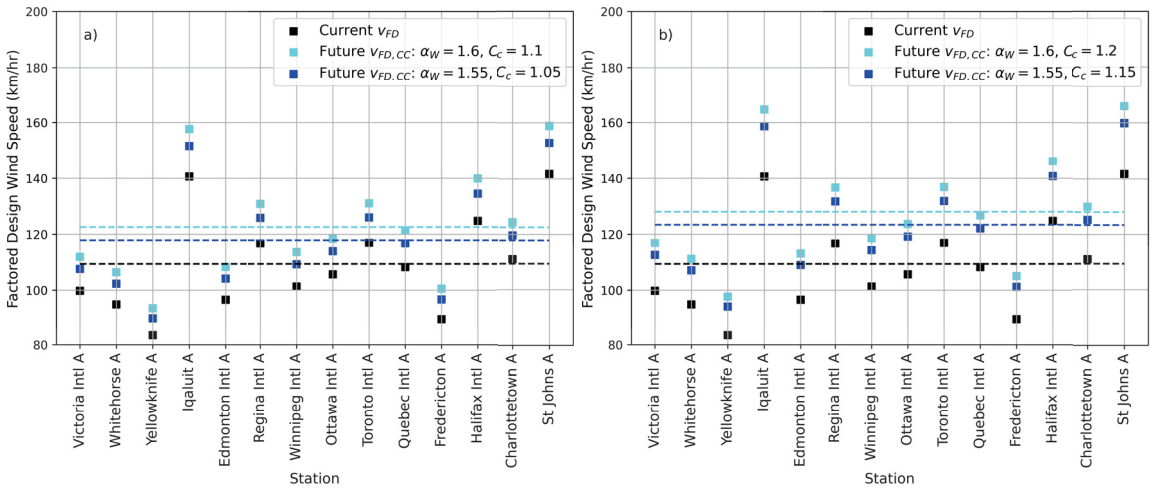

Figure 3.4: Current and future climate change factored design wind speeds, v_{FD} and $v_{FD,CC}$, respectively, for 50% and 125% model uncertainty (u_{CC}) in (a) case 1 ($\Delta_\mu = 0.0008u_{CC}$, $\Delta_\sigma = 0.004u_{CC}$) and (b) case 2 ($\Delta_\mu = 0.0016u_{CC}$, $\Delta_\sigma = 0.004u_{CC}$) for 14 Canadian cities.

Figure 3.4 demonstrates that, on average, the factored design wind speed will increase 8.6 km h^{-1} for case 1, and 14 km h^{-1} for case 2, relative to the current value of v_{FD}, if the model uncertainty is assumed to be only 50%. By adopting the proposed values of C_c and α_W for 125% uncertainty, the average factored design wind speed will increase 13 km h^{-1} for case 1, and 19 km h^{-1} for case 2, relative to v_{FD}.

The probability that $v_{FD,CC}$ is exceeeded in a given year can then be determined using eq. (1.46), where $F_{v_{A1}}(r; y)$ is the non-stationary Gumbel distribution defined by Δ_μ and Δ_σ, and the threshold, $r = v_{FD,CC}$. The 50-year exceedance probability, p_{50}, of $v_{FD,CC}$ can then be found using eq. (1.47). Figures 3.5(a) and (b) show p_{50} of $v_{FD,CC}$ evaluated under climate change case 1 assuming (a) 50% uncertainty ($u_{CC} = 1.5$) and (b) 125% uncertainty ($u_{CC} = 2.25$) in Δ_μ and Δ_σ. The cyan squares show p_{50} when $u_{CC} = 2.25$ (i.e., $C_c = 1.1$ and $\alpha_W = 1.6$). While, the blue squares show p_{50} when $u_{CC} = 1.5$ (i.e., $C_c = 1.05$ and $\alpha_W = 1.55$). The purple squares show p_{50} if no change is made to the NBCC (i.e., $C_c = 1.0$ and $\alpha_W = 1.4$). The current values of p_{50} for v_{FD} (black circles), as shown in Fig. 3.1, are also included for reference, as well as the value of p_{50} evaluated at the three target exceedance probabilities, p_e = 1e-3, 2e-3 and 3e-3, shown by the green, orange and red lines, respectively.

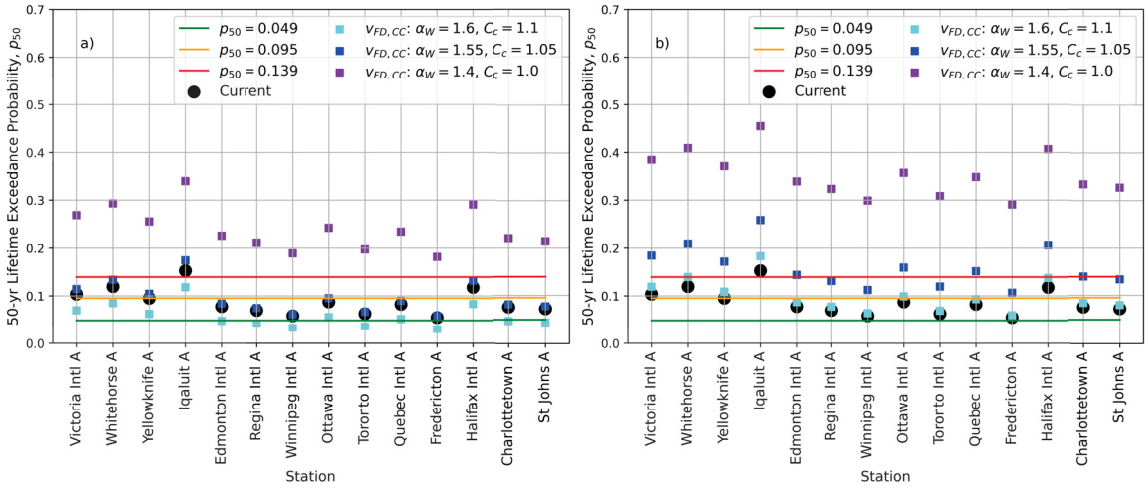

Figure 3.5: Fifty-year lifetime exceedance probability for $v_{FD,CC}$, under climate change case 1 ($\Delta_\mu = 0.0008u_{CC}$, $\Delta_\sigma = 0.004u_{CC}$) assuming (a) 50% model uncertainty ($u_{CC} = 1.5$) and (b) 125% model uncertainty ($u_{CC} = 2.25$) for 14 Canadian cities.

Figures 3.6(a) and (b) are similar to Figs. 3.5(a) and (b), but show the results under climate change case 2. The cyan squares are based on case 2 design values for 125% uncertainty (i.e., $C_c = 1.2$ and $\alpha_W = 1.6$), and the blue squares use the case 2 design values for 50% uncertainty (i.e., $C_c = 1.1$ and $\alpha_W = 1.55$).

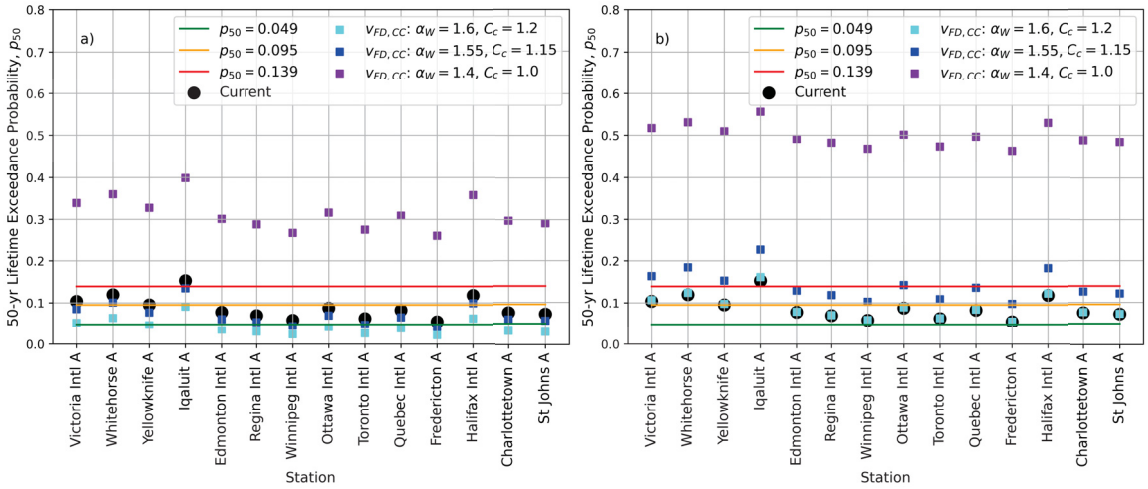

Figure 3.6: Fifty-year lifetime exceedance probability for $v_{FD,CC}$, under climate change case 2 ($\Delta_\mu = 0.0008u_{CC}$, $\Delta_\sigma = 0.004u_{CC}$) assuming (a) 50% uncertainty ($u_{CC} = 1.5$) and (b) 125% uncertainty ($u_{CC} = 2.25$) for 14 Canadian cities.

Figures 3.5(b) and 3.6(b) show that in both climate change cases, if the realized

future scenario is that based on $u_{CC} = 2.25$ (i.e., 125% uncertainty), assuming the wind design values C_c and α_W for 125% uncertainty will result in the 50-year lifetime exceedance probability being close to the current value at each location. While adopting wind design values C_c and α_W for 50% uncertainty causes p_{50} to be greater than, or very close to the maximum lifetime exceedance probability (red line) for all locations under the same future scenario (125% uncertainty). However, if the realized future scenario is that based on $u_{CC} = 1.5$ (i.e., 50% uncertainty), the current reliability level will be maintained using the suggested design values C_c and α_W for 50% uncertainty, and the suggested design values C_c and α_W for 125% uncertainty will result in over design.

Figure 3.7 shows the average 50-year lifetime exceedance probability over the 14 cities for climate change (a) case 1 and (b) case 2 for uncertainty factors $1.0 \leq u_{CC} \leq 2.25$. The wind loading design values, C_c and α_W, used to determine $v_{FD,CC}$ are the same as those used in Figs. 3.5 and 3.6.

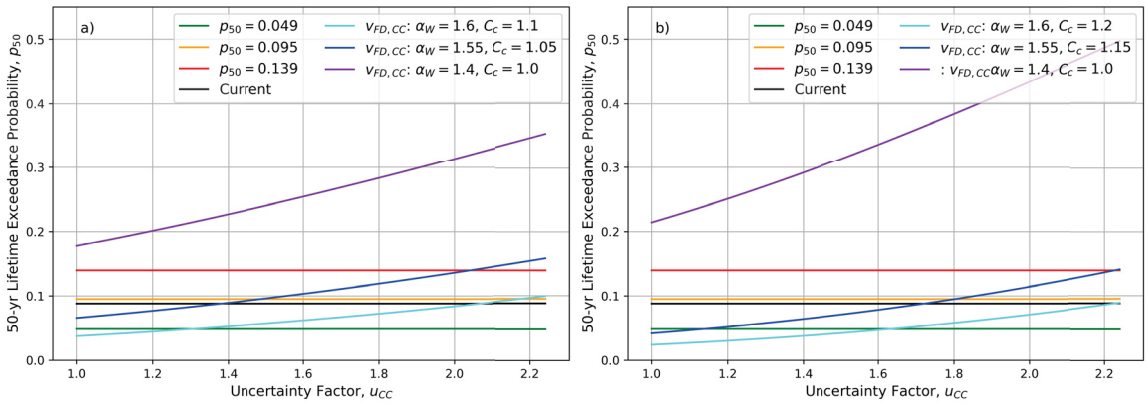

Figure 3.7: Average probability that $v_{FD,CC}$ is exceeded over a 50-year lifetime, where the uncertainty factor, u_{CC}, ranges from 1.0 to 2.25, for 14 Canadian cities under climate change (a) case 1 and (b) case 2.

Figure 3.7 demonstrates that if the new values of C_c and α_W are not adopted (i.e., the design values remain as $C_c = 1.0$ and $\alpha_W = 1.4$) the probability that the factored design wind speed is exceeded during a 50-year lifetime will significantly increase. Consequently, the probability that structures will fail under wind loading will also increase if the design load and resistance factors are not increased. Figure 3.7 also shows that adopting the suggested values of C_c and α_W for 50% uncertainty may result in the average value of p_{50} being greater than the maximum target exceedance

probability (i.e., p_{50} at p_e = 3e-3). For example, using $C_c = 1.05$ and $\alpha_W = 1.55$ under climate change case 1, p_{50} exceeds the maximum target exceedance probability when $u_{CC} \geq 2.05$. Similarly, for climate change case 2, when $C_c = 1.1$ and $\alpha_W = 1.55$, p_{50} is greater the NBCC maximum 50-year lifetime exceedance probability when $u_{CC} \geq 2.23$. Note that at $u_{CC} = 2.05$ for case 1, $\Delta_\mu = 0.0008(2.05) = 0.00164$ and $\alpha_\sigma = 0.004(2.05) = 0.0082$. While at $u_{CC} = 2.23$ for case 2, $\Delta_\mu = 0.0016(2.23) = 0.00357$ and $\Delta_\sigma = 0.004(2.23) = 0.00892$. If the realized future scenario is that based on $u_{CC} = 2.25$ (i.e., 125% uncertainty) and the suggested values of C_c and α_W for 50% uncertainty are adopted, the average probability that $v_{FD,CC}$ is exceeded over a 50-year lifetime will increase by 44% relative to the current value under case 1, and by 38% relative to the current value under case 2.

3.3.1 Effect of Climate Change on the Gust Factor

As shown in Section 1.4.3, the gust factor, G, and consequently, the gust effect factor, C_g, will increase in the future if the instantaneous wind speed coefficient of variation, CV_V, increases. Recall that C_g is applied to wind pressure, while G is applied to wind speed, therefore, $G = \sqrt{C_g}$. It is important to update the gust effect factor because climate change is expected to cause an increase in the magnitude and frequency of wind gust events (see Section 2.5).

The results of Section 1.3.4 found that even under the current, stationary climate conditions the value of C_g in the NBCC may need to be increased because the CV_V values found across Canada are higher than CV_V estimated based on the Durst Curve. Additionally, Section 1.3.4 showed that under current conditions C_g should vary with location because CV_V varies across Canada. Section 1.4.3 then assessed the effect of non-stationarity on the gust factor. That is, the change in the gust factor when the instantaneous wind speed coefficient of variation, CV_V, changes over time. As expected, Fig. 1.15 showed that if CV_V increases over time the gust factor will also increase.

To the author's knowledge, there are no studies to date on the effect of climate change on CV_V, however, the effect of climate change on the gust factor itself has been studied. Jeong and Sushama (2019) used simulations to determine the expected percent increase in the gust factor for the future 2071-2100 period relative to the

current 1981-2010 period, where the gust factor was defined as the ratio of the 50-year return period annual maximum wind gust to the 50-year return period annual maximum wind speed. Jeong and Sushama (2019) found that a maximum increase of 12% is expected across most regions of Canada, while the gust factor may increase up to 20% in a few regions on the west coast. Given that model uncertainty may be up to 125%, it is possible that the gust factor may increase by up to 27% ($12\% * 2.25$) across most regions of Canada, and up to 45% ($20\% * 2.25$) on the west coast.

The non-stationary gust factor was evaluated over a range of CV_V values to determine the relative increases in CV_V that result in the gust factor increasing by up to 45%. In this analysis, the non-stationary gust factor, G_y, is defined in terms of the total relative increase in CV_V over y years, η_{CV_y}, instead of the annual rate of increase (Δ). That is, the coefficient of variation at year y is defined as $\mathrm{CV}_V(y) = \mathrm{CV}_V(0)\left(1 + \eta_{CV_y}\right)$. Figure 3.8 shows $G_y(w = 3 \text{ sec}, W = 1 \text{ hr})$ evaluated using eq. (1.49) for the range $0 \leq \eta_{CV_y} \leq 1$, where $\mathrm{CV}_V(0) = 0.64$ which is the average CV_V of the four locations in Fig. 1.4. The left y-axis label shows the relative increase in G_y, that is, $(G_y - G_0)/G_0$, while, the right y-axis label shows the magnitude of G_y.

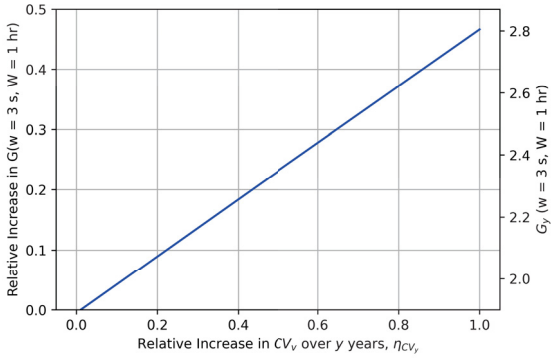

Figure 3.8: Non-stationary gust factor, $G_y(w = 3 \text{ s}, W = 1 \text{ hr})$, evaluated based on a total relative increase in CV_V over y years, η_{CV_y}, for the range $0 \leq \eta_{CV_y} \leq 1$. Note that $G_y(w = 3 \text{ s}, W = 1 \text{ hr}) = 1.90$ when $\eta_{CV_y} = 0$.

Figure 3.8 demonstrates that a 58% increase in CV_V results in the gust factor increasing by 27%, from 1.90 to 2.42, which is the expected increase in G across most areas of Canada, assuming 125% model uncertainty. While, when CV_V increases 97% the gust factor increases by 45%, from 1.90 to 2.77, which is the expected increase in G for some regions of the west coast based on 125% model uncertainty. Note

that the expected increases in the CV of instantaneous wind speeds (i.e., 58% and 97%) are significantly higher the expected increase in the CV of the annual maximum one-hourly average wind speed, $\mathrm{CV}_{V_{A1}}$. Assuming 125% model uncertainty, $\mathrm{CV}_{V_{A1}}$ is expected to increase approximately 36% across most regions of Canada (i.e., $1-\frac{1+\Delta_\sigma}{1+\Delta_\mu}$, where $\Delta_\sigma = 0.20 * 2.25 = 0.45$ and $\Delta_\mu = 0.04 * 2.25 = 0.09$). However, there is no reason to believe that CV_V and $\mathrm{CV}_{V_{A1}}$ should increase at the same rate under climate change.

The results of Fig. 3.8 provide a range of possible values of C_g to be used under climate change, but selection of the most appropriate future gust effect factor is considered outside of the scope of this thesis. The future gust effect factor should be determined such that the current peak gust speed lifetime exceedance probability is equal to the peak gust speed lifetime exceedance probability under climate change, which should account for increases in CV_V, as well as the frequency of wind gust events. Further climate change simulations and analysis are therefore required to determine these lifetime exceedance probabilities.

Chapter 4

Ultimate Return Period Design Methodology

4.1 General

The load factor method, used in the NBCC, results in inconsistent exceedance probability levels across Canada, as demonstrated in Section 3.2.1. The load factor method defines the factored design wind load as the product of the wind load factor, $\alpha_W = 1.4$, and the characteristic wind load, $\hat{F}_W$. The problem with this method is that only $\hat{F}_W$ varies with location, while $\alpha_W = 1.4$ is constant across Canada. Figure 3.1 shows that this method results in exceedance probabilities near the minimum target (i.e., $p_e =$ 1e-3) for locations such as Toronto, ON and Winnipeg, MB, while the exceedance probability for other places in Canada, including Iqaluit, NU, exceeds the maximum target (i.e., $p_e =$ 3e-3) because the variance of the annual maximum wind speed is higher in these locations.

To illustrate the cause of inconsistent exceedance probability levels across Canada, the relationship between the 50-year exceedance probability and wind speed is assessed at various locations across Canada. The distribution of the 50-year return period annual maximum wind speed, $v_{A1,50}$ is first determined using the exact extreme value distribution. Assuming each year is independent, the CDF of $v_{A1,50}$ is given as

$$\begin{aligned} F_{v_{A1,50}}(v) &= \left[F_{v_{A1}}(v)\right]^{50} = \left[\exp(-\exp(-(v-u_{v_{A1}})/a_{v_{A1}}))\right]^{50} \\ &= \exp(-50\exp(-(v-u_{v_{A1}})/a_{v_{A1}})) \end{aligned} \tag{4.1}$$

Alternatively, the CDF of $v_{A1,50}$ can be determined using the asymptotic extreme value distribution of v_{A1}. Since v_{A1} follows a Gumbel distribution, which has an unlimited exponentially decaying tail, the 50-year extreme value distribution of v_{A1} also follows a Gumbel distribution (Fenton and Griffiths, 2008). The CDF of $v_{A1,50}$

is then given as

$$F_{v_{A1,50}}(v) = \exp(\exp(-(v - u_{v_{A1,50}})/a_{v_{A1,50}})) \tag{4.2}$$

where the location parameter $u_{v_{A1,50}}$ is given as $u_{v_{A1,50}} = F^{-1}_{v_{A1}}\left(1 - \frac{1}{50}\right)$ and the scale parameter is defined as $a_{v_{A1,50}} = \left[50 f_{v_{A1}}(u_{v_{A1,50}})\right]^{-1}$. Note that $f_{v_{A1}}(v)$ denotes the PDF of v_{A1}.

The CDF, $F_{v_{A1,50}}(v)$, was evaluated for the 14 Canadian cities given in Table 3.1 for wind speeds $v = 1, 2, ...250$ using both the exact and the asymptotic CDF (i.e., eq. 4.1 and eq. 4.2, respectively). The error between the two CDFs was then evaluated. The average SSE over the 14 locations was 0.0011, and the maximum SSE was 0.0018. Therefore, the two methods of determining $F_{v_{A1,50}}(v)$ are considered equal. The asymptotic extreme value distribution (i.e., eq. 4.2) is used in this thesis.

The 50-year exceedance probability, p_{50}, of a given wind speed, v, can then be determined using the CDF of $v_{A1,50}$, as

$$p_{50} = 1 - F_{v_{A1,50}}(v) \tag{4.3}$$

The 50-year exceedance probability was calculated for Fredericton, the city with the lowest exceedance probability, and Iqaluit, the city with the highest exceedance probability using the parameters given in Table 3.1. Figures 4.1(a) and (b) show the results for Fredericton and Iqaluit, respectively. The factored design wind speed, v_{FD}, and 1-in-50 year value, $v_{A1,50}$, are also included on the graph for comparison. Note that the mode of $F_{v_{A1,50}}(v)$ is $u_{v_{A1,50}}$, which is equal to $v_{A1,50}$.

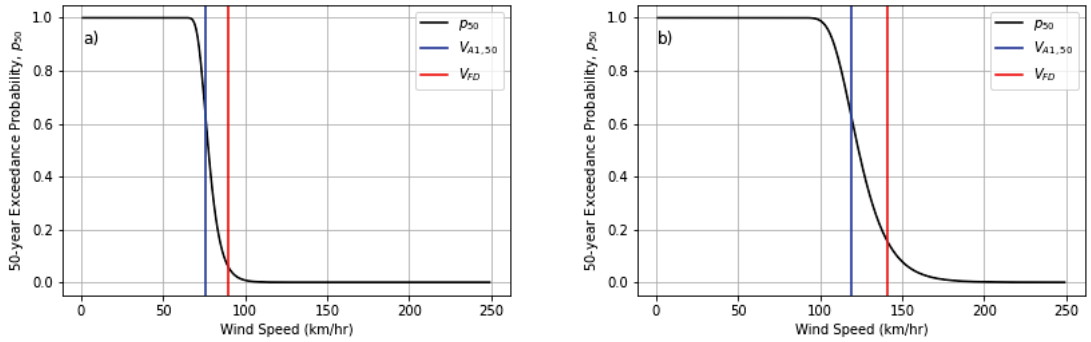

Figure 4.1: Fifty-year exceedance probability for (a) Fredericton A and (b) Iqaluit A.

Figure 4.1 shows that the 50-year probability of exceeding v_{FD} (red line) in (a) for

Fredericton is 0.06, while in (b) for Iqaluit it is 0.16. The current method for calculating the factored design wind speed, v_{FD}, multiplies $v_{A1,50}$ by a constant load factor of $\sqrt{1.4} \approx 1.18$. The constant load factor does not account for the changes in variance of the distribution at different locations in Canada. It can be seen from Fig. 4.1 that the width of the wind speed distribution is much wider (higher variance) in (b) Iqaluit than in (a) Fredericton. Consequently, Iqaluit has a larger probability of exceeding v_{FD}, $p_{v_{FD}}$, than Fredericton due to its larger variance.

An alternative to the load factor method is the so-called ultimate return period method, which has been adopted in the United States in the *ASCE-7 Minimum Design Loads For Buildings and Other Structures* (ASCE-7), beginning in the 2010 edition. The ultimate return period method defines the factored design wind speed, v_{FD}, as the product of a wind load factor of 1.0 and a much larger return period annual maximum wind speed, v_{A1,m_U}, where m_U is the "ultimate" return period, typically several hundred years. In other words, the factored design wind speed in the NBCC, $v_{FD} = \sqrt{1.4}v_{A1,50}$ is replaced by $v_{FD} = v_{A1,m_U}$, where $m_U = 1/p_{v_{FD}}$, where $p_{v_{FD}}$ is the annual exceedance probability of v_{FD}. Recall that under stationary conditions, the m-year return period has an annual exceedance probability $p = 1/m$ (see Section 1.3.3). Since $p_{v_{FD}}$ currently varies by location, as shown in Table 3.2, the current corresponding value of the ultimate return period also varies by location. However, adopting a constant m_U across Canada will, by definition, result in consistent exceedance probabilities. The most appropriate value of m_U can then be determined based on a given target annual exceedance probability, p_e, as

$$m_U = \frac{1}{p_e} \tag{4.4}$$

Using eq. (4.4), the ultimate return periods corresponding to the three target annual exceedance probabilities defined in Section 3.2.1 (i.e., p_e = 1e-3, 2e-3, and 3e-3) are 1000 years, 500 years and 333 years, respectively.

The advantage of improved exceedance probability consistency prompted the ASCE (American Society for Civil Engineers) to adopt the ultimate return period method beginning in the 2010 edition of the ASCE-7 (ASCE-7-10). The ultimate return period method improves exceedance probability consistency because it eliminates the need for load factors, which may not accurately reflect the variability of the extreme wind speeds across various regions (Vickery et al., 2010). The current

ASCE-7 uses an ultimate return period of 700 years for nonhurricane prone regions of the United States, which was calibrated based on a wind load factor of 1.6 and return period of 50 years used in editions of the ASCE-7 prior to 2010 (Vickery et al., 2010). Note that the current NBCC load factor accounts for uncertainty in all parameters of eq. (1.4), including C_g and C_t, as well as the wind speed, while, the ultimate return period only accounts for variability in the wind speed. Vickery et al. (2010) found that it is valid to switch to the ultimate return period method because wind speed uncertainty contributes 70-80% of the total uncertainty in the characteristic wind load, as discussed in Section 3.1.

The possible disadvantage of the ultimate return period method is that there is more uncertainty in estimates of v_{A1,m_U} than in estimates of $v_{A1,50}$, when $m_U \gg 50$, due to lack of historical records and sampling error. For the NBCC, the distribution model parameters of $F_{v_{A1}}$ are estimated based on only 10 to 54 years of data. Consequently, estimates of $v_{A1,700}$, for example, are more uncertain than estimates of $v_{A1,50}$. Hong et al. (2016) studied uncertainty in Canadian factored design wind speeds using both the load factor and ultimate return period method. They found that the load factor method is preferred for a "statistically homogeneous wind climate", meaning that the distribution of v_{A1} is constant in both time and space (Hong et al., 2016). However, the ultimate return period method is preferred for Canada because the range of $\mathrm{CV}_{v_{A1}}$ values across Canada causes significant variation in $p_{v_{FD}}$, as shown in Fig. 3.1. Hong et al. (2016) found that the variation in $p_{v_{FD}}$ caused by the range of $\mathrm{CV}_{v_{A1}}$ values across Canada was more than twice as large as that due to sample size effect. Based on these findings Hong et al. (2016) concluded that the ultimate return method should be used in future editions of the NBCC with m_U between 500 and 700 years if the target reliability index remains at 3.0 for a 50-year service period.

Similar to Chapter 3, the objective of this chapter is to update the ultimate return period wind loading parameters such that a target exceedance probability level is consistently achieved across Canada under climate change.

4.2 Current Ultimate Return Period Design Wind Speeds

First the ultimate return period design wind speeds under current climate conditions are considered. The ultimate return period design wind speed for a given return

period, m_U, is given as

$$v_{A1,m_U} = u_{v_{A1}} - a_{v_{A1}} \ln\left(-\ln\left(1 - \frac{1}{m_U}\right)\right) \tag{4.5}$$

assuming the annual maximum one-hourly average wind speed follows a Gumbel distribution. Using the scale and location parameters for the 14 Canadian cities listed in Table 3.1, the ultimate return period design wind speeds were calculated using eq. (4.5), and compared to the current factored design wind speeds in Fig. 4.2. The ultimate return period design wind speeds were calculated based on the maximum, mid-level and conservative target exceedance probabilities (i.e., 1e-3, 2e-3 and 3e-3), which correspond to ultimate return periods of 1000, 500 and 333 years, respectively. Figure 4.2 shows the current factored design wind speed, v_{FD}, as well as the 1000-, 500- and 333-year ultimate return period design wind speeds.

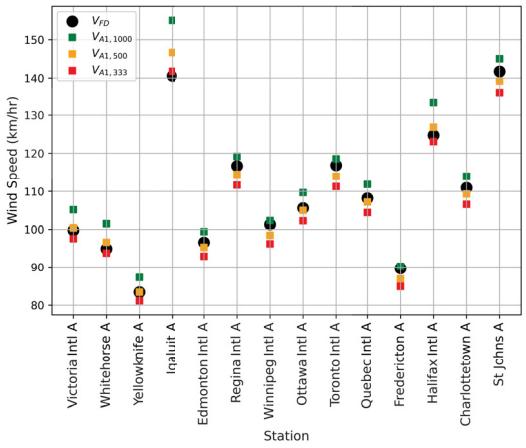

Figure 4.2: Current factored design wind speeds, v_{FD}, compared to ultimate return period design wind speeds values for 14 Canadian cities when m_U = 1000, 500 and 333 years.

Figure 4.2 demonstrates that the current factored design wind speed is closest to the 500-year return period design wind speed for most locations. However, as expected, the current factored design wind speed for Victoria, Whitehorse, Yellowknife, Iqaluit and Halifax is closer to the 333-year return period wind speed. The average 1000-year return period design wind speed over the 14 locations is approximately 4% greater than the average current value of v_{FD}. While, $v_{A1,500}$ and $v_{A1,333}$ are 0.5% and 3% less than v_{FD}, on average, respectively. Therefore, to achieve a target exceedance

probability equal to the current average exceedance probability, a 500-year return period should be adopted, if the current climate conditions remain stationary. Although the average difference between the factored design wind speed and ultimate return period design wind speed is small, adopting an ultimate return period design wind speed means the 50-year lifetime exceedance probability for all locations across Canada will be equal to the target.

4.3 Effect of Climate Change on the Ultimate Return Period

Similar to Section 3.3, an updated wind loading design methodology is proposed in this section that accounts for future increases in the mean and standard deviation of the annual maximum one-hourly average wind speed due to climate change. Two alternative methods are presented in this section that are based on the ultimate return period method. The design parameters in both methods are selected such that the 50-year exceedance probability, p_{50}, is approximately equal to a target 50-year exceedance probability under a given climate change scenario. Note that a 50-year target exceedance probability is used instead of an annual exceedance probability target, since the annual exceedance probability is non-stationary under climate change. The annual exceedance probability is non-stationary because the distribution of V_{A1} changes with time under climate change. In the future, the annual maximum one-hourly average wind speed, V_{A1}, is assumed to follow a non-stationary Gumbel distribution with a linearly increasing mean and standard deviation. That is, $\mu_{v_{A1}}(y) = \mu_{v_{A1}}(0)\left(1 + \Delta_\mu y\right)$ and $\sigma_{v_{A1}}(y) = \sigma_{v_{A1}}(0)\left(1 + \Delta_\sigma y\right)$, where Δ_μ and Δ_σ are the annual rates of change in the mean and standard deviation of V_{A1} relative to $\mu_{v_{A1}}(0)$ and $\sigma_{v_{A1}}(0)$, which are the initial mean and standard deviation.

4.3.1 Investigation of Possible Ultimate Return Period Methods Under Climate Change

The first method proposed in this section will be called the "All-Inclusive Ultimate Return Period" (AURP) method, which defines the AURP design wind speed under climate change as $v_{AU,CC} = v_{A1,m_{AU}}$. The "all-inclusive ultimate return period", m_{AU}, is an updated value of m_U that accounts for increases in both the mean and standard deviation of V_{A1} due to climate change (note that currently $m_U = 500$, as discussed

in Section 4.2). The updated ultimate return period under climate change, m_{AU}, is determined such that the m_{AU}-return period annual maximum one-hourly average wind speed, $v_{A1,m_{AU}}$, has a 50-year exceedance probability, p_{50}, equal to a given target 50-year exceedance probability. The probability that $v_{AU,CC}$ is exceeded over 50 years is determined using eq. (1.47). For example, if the target 50-year exceedance probability is 0.049, $v_{A1,m_{AU}}$, is obtained from

$$0.049 = 1 - \prod_{y=1}^{50} \left[F_{v_{A1}}(v_{A1,m_{AU}}; y) \right] \tag{4.6}$$

where $F_{v_{A1}}(v; y)$ is the non-stationary Gumbel distribution defined in eq. (1.39) with $\mu_{v_{A1}}(y) = \mu_{v_{A1}}(0)\left(1 + \Delta_\mu y\right)$ and $\sigma_{v_{A1}}(y) = \sigma_{v_{A1}}(0)\left(1 + \Delta_\sigma y\right)$. Since $v_{A1,m_{AU}}$ accounts for increases in both the mean and standard deviation of V_{A1}, $\Delta_\mu > 0$ and $\Delta_\sigma > 0$. In this thesis the solution to eq. (4.6) is found using trial and error, and linear interpolation. Also, note that three 50-year exceedance probability targets are used in this thesis: $p_{50} = 0.049$, 0.095 and 0.139. These exceedance probability targets are the values of $p_{50} = 1 - (1 - p_e)^{50}$, calculated based on the annual exceedance probability targets introduced in Chapter 3 (i.e., p_e = 1e-3, 2e-3 and 3e-3).

Using the AURP method, the characteristic wind load is then given as

$$\hat{F}_W = I_W q_{A1,m_{AU}} C_e C_t C_g C_p \tag{4.7}$$

where $q_{A1,m_{AU}} = \frac{1}{2}\rho_{air} v^2_{A1,m_{AU}}$. Note that for this method the load factor is $\alpha_W = 1.0$.

Figure 4.3 shows the all-inclusive ultimate return period, m_{AU}, required to achieve the mid-level 50-year exceedance probability target, $p_{50} = 0.095$, for 14 Canadian cities. Although in practice the mean and standard deviation of V_{A1} will likely increase simultaneously, Figure 4.3(a) shows the m_{AU} for various $\Delta_\mu > 0$ with $\Delta_\sigma = 0$, and Fig. 4.3(b) shows the m_{AU} for $\Delta_\mu = 0$ with various $\Delta_\sigma > 0$. Figure 4.3 shows the results for increases in the the mean and standard deviation of V_{A1} separately to demonstrate how a given annual rate of change $\Delta = \Delta_\sigma = \Delta_\mu$ impacts m_{AU} differently when the change is in the mean compared to when the change is in the standard deviation of V_{A1}. The effect of simultaneous increases in $\mu_{v_{A1}}$ and $\sigma_{v_{A1}}$ on m_{AU} are assessed later in Section 4.3.2.

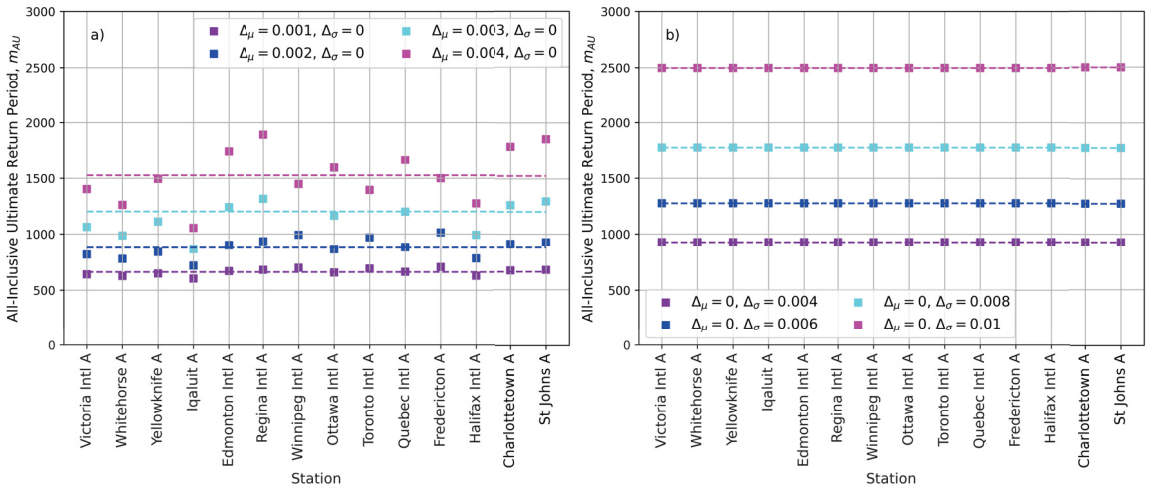

Figure 4.3: All-inclusive ultimate return period, m_{AU}, required to achieve 50-year exceedance probability target $p_{50} = 0.095$ for 14 Canadian cities under climate change for (a) varying Δ_μ and $\Delta_\sigma = 0$, and (b) $\Delta_\mu = 0$ with varying Δ_σ.

Figure 4.3 demonstrates that there are two key differences between the resulting values of m_{AU} when $\mu_{v_{A1}}$ and $\sigma_{v_{A1}}$ are increased separately. First, Fig. 4.3 shows that higher values of m_{AU} are required to achieve a given target p_{50} when the mean of V_{A1} is increased at Δ_μ, compared to when the standard deviation of V_{A1} is increased at the same rate (i.e., $\Delta_\sigma = \Delta_\mu$). For example, to achieve $p_{50} = 0.095$ when $\Delta_\mu = 0.004$ and $\Delta_\sigma = 0$, the average ultimate return period needs to be increased to $m_{AU} = 1526$ years, while when $\Delta_\mu = 0$ and $\Delta_\sigma = 0.004$ the average m_{AU} required to achieve $p_{50} = 0.095$ is only 927 years. As discussed in Section 1.4.2, the annual rate of increase in the mean has a more significant effect on the design wind speed than that of the standard deviation because the initial mean, $\mu_{V_{A1}}(0)$, is approximately ten times greater than the initial standard deviation, $\sigma_{V_{A1}}(0)$. Therefore, for the same relative increase, $\Delta = \Delta_\sigma = \Delta_\mu$, the magnitude of the mean increases more than that of the standard deviation.

The second difference in m_{AU} between Figs. 4.3(a) and (b) is that m_{AU} is constant for all locations for a given increase in $\sigma_{V_{A1}}$, as shown in Fig. 4.3(b), while m_{AU} varies across the 14 locations for a given increase in $\mu_{V_{A1}}$ (see Fig. 4.3a). The corollary of the variation between locations in m_{AU} in Fig. 4.3(a) is that if a constant value of m_{AU} is adopted across all locations (as proposed in the all-inclusive ultimate

return period method), the 50-year exceedance probability will then vary with location, assuming $\Delta_\mu > 0$. Therefore, this first method will not meet the objective of consistent exceedance probability levels across Canada, although it may improve the exceedance probability consistency relative to the LRFD methodology, discussed in Chapter 3. This problem motivates the second ultimate return period based climate change design methodology proposed in this section which will be called "Hybrid Ultimate Return Period" (HURP) method.

As the name suggests, the Hybrid Ultimate Return Period method is a hybrid approach, combining the ultimate return period and the climate change effect factor, C_c (introduced in Section 3.3). In this hybrid method, the "hybrid ultimate return period", m_{HU}, accounts for increases in the variability of q_{A1} due to climate change while the HURP method climate change effect factor, $C_{c,HU}$, accounts for the projected increases in the mean of q_{A1} due to climate change. The hybrid ultimate return period under climate change, m_{HU}, is determined in the same way as m_{AU}; eq. (1.47) is used to solve for m_{HU} such that $v_{A1,m_{HU}}$ has a 50-year exceedance probability, p_{50}, equal to a given target 50-year exceedance probability. For example, if the target 50-year exceedance probability is 0.049, $v_{A1,m_{HU}}$, is determined from

$$0.049 = 1 - \prod_{y=1}^{50} \left[F_{v_{A1}}(v_{A1,m_{HU}}; y) \right] \tag{4.8}$$

where $F_{v_{A1}}(v; y)$ is the non-stationary Gumbel distribution defined in eq. (1.39) with $\mu_{v_{A1}}(y) = \mu_{v_{A1}}(0)\left(1 + \Delta_\mu y\right)$ and $\sigma_{v_{A1}}(y) = \sigma_{v_{A1}}(0)\left(1 + \Delta_\sigma y\right)$. Since $v_{A1,m_{HU}}$ accounts for increases in $\sigma_{v_{A1}}$ and not $\mu_{v_{A1}}$, $\Delta_\mu = 0$ and $\Delta_\sigma > 0$. In this thesis the solution to eq. (4.8) is found using trial and error, and linear interpolation.

The HURP method climate change effect factor, $C_{c,HU}$, is defined in a similar way to C_c used in the LRFD method (i.e., eq. 3.5) as

$$C_{c,HU} = \left(\frac{v_{CC}}{v_{A1,m_U}} \right)^2 \tag{4.9}$$

where v_{CC} is the wind speed that has a 50-year exceedance probability, p_{50}, equal to a given target 50-year exceedance probability when $\Delta_\mu > 0$ and $\Delta_\sigma = 0$, and v_{A1,m_U} is the wind speed required to achieve the same 50-year exceedance probability target, p_{50}, but it is evaluated under current climate conditions (i.e., when $\Delta_\mu = 0$ and

$\Delta_\sigma = 0$). For example, if the 50-year exceedance probability target is 0.049, which corresponds to an annual exceedance probability of 0.001, then $m_U = 1000$ and the denominator in eq. (4.9) is $v_{A1,m_U} = v_{A1,1000}$.

Using the definition of m_{HU} provided by eq. (4.8) and the definition of $C_{c,HU}$ provided above, the characteristic wind load for the Hybrid Ultimate Return Period method is then

$$\hat{F}_W = I_W q_{A1,m_{HU}} C_e C_t C_g C_p C_{c,HU} \tag{4.10}$$

Therefore, the HURP design wind speed is $v_{HU,CC} = \sqrt{C_{c,HU}} v_{A1,m_{HU}}$. Note that for the HURP method $\alpha_W = 1.0$.

4.3.2 Application of the All-Inclusive and Hybrid Ultimate Return Period Methods

This subsection evaluates the design parameters required to provide a given target 50-year exceedance probability, as well as the corresponding design wind speeds and 50-year exceedance probabilties under climate change for the all-inclusive and hybrid ultimate return period design methods. The same two climate change cases considered in Section 3.3 are also considered here: case 1 where $\Delta_\mu = 0.0008 u_{CC}$ and $\Delta_\sigma = 0.004 u_{CC}$, and case 2 where $\Delta_\mu = 0.0016 u_{CC}$ and $\Delta_\sigma = 0.004 u_{CC}$. Recall that u_{CC} is the uncertainty factor, which accounts for uncertainty in the model projections. Each climate change case is assessed for $1.0 \leq u_{CC} \leq 2.25$.

As discussed above, the all-inclusive ultimate return period method requires determining m_{AU} such that $v_{A1,m_{AU}}$ has a 50-year exceedance probability equal to a given target value. The resulting ultimate return period, m_{AU}, accounts for increases in both the mean and standard deviation of V_{A1}. Figures 4.4(a) and (b) show the values of m_{AU} required to achieve 50-year exceedance probability targets of $p_{50} = 0.049$, 0.095 and 0.139 under climate change cases 1 and 2, respectively. These 50-year exceedance probability targets are calculated based on the annual exceedance probability targets used in Chapter 3 (i.e., p_e = 1e-3, 2e-3 and 3e-3). Figure 4.4 shows the average results over the 14 Canadian cities listed in Table 3.1 for a range of 0% to 125% model uncertainty (i.e., $1.0 \leq u_{CC} \leq 2.25$).

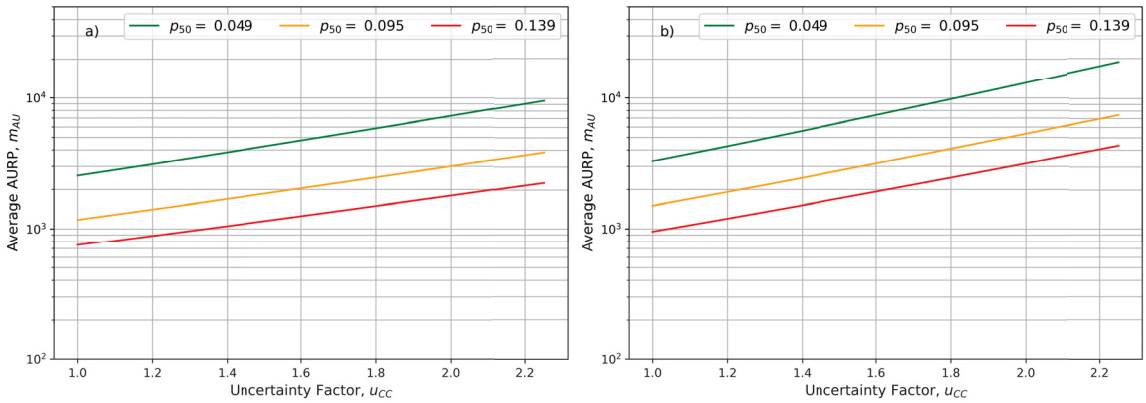

Figure 4.4: Average all-inclusive ultimate return period, m_{AU}, over 14 Canadian cities required to achieve target 50-year exceedance probability p_{50} under climate change cases (a) 1 ($\Delta_\mu = 0.0008u_{CC}$, $\Delta_\sigma = 0.004u_{CC}$) and (b) 2 ($\Delta_\mu = 0.0016u_{CC}$, $\Delta_\sigma = 0.004u_{CC}$) for $1.0 \leq u_{CC} \leq 2.25$.

Figure 4.4 demonstrates that the ultimate return periods required to achieve the exceedance probability targets under climate change are significantly larger than the current ultimate return period (i.e., $m_U = 500$), and that m_{AU} increases rapidly as Δ_μ and Δ_σ increase (i.e., u_{CC} increases). Additionally, the value of m_{AU} required to achieve $p_{50} = 0.049$ is significantly higher than that required to achieve $p_{50} = 0.139$. For example, under climate change case 1 with 125% model uncertainty $m_{AU} = 2265$ years for $p_{50} = 0.139$, while $m_{AU} = 9592$ years for $p_{50} = 0.049$.

The mid-level exceedance probability target ($p_{50} = 0.095$) is used in this subsection to determine recommended design values. The results of Fig. 4.4 are used to determine the values of m_{AU} required for climate change cases 1 and 2, assuming both 50% and 125% model uncertainty. The results are rounded to the nearest hundred for simplicity. For climate change case 1, the recommended value of m_{AU} is 1900 years assuming 50% model uncertainty, 3900 years if the model uncertainty assumed to be 125%. For climate change case 2, $m_{AU} = 2800$ years assuming 50% model uncertainty, and 7500 years assuming 125% model uncertainty. Using these recommended design parameters, the future AURP design wind speeds to be used under climate change (i.e., $v_{AU,CC} = v_{A1,m_{AU}}$) were calculated and are shown in Fig. 4.5. Figure 4.5(a) and (b) show the results for climate change cases 1 and 2, respectively. The current factored design wind speeds, v_{FD}, are included for reference.

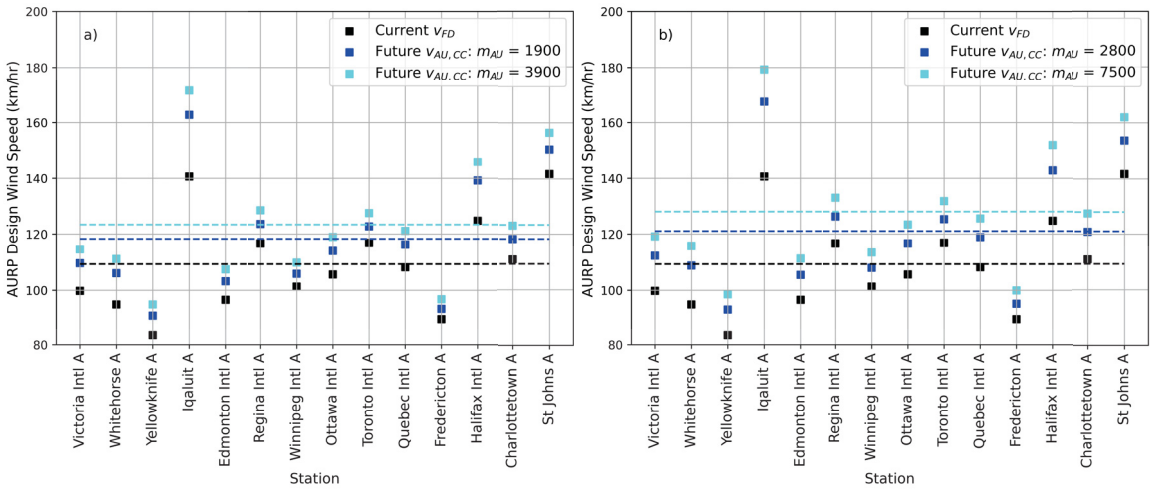

Figure 4.5: Current design wind speeds and future AURP design wind speeds, v_{FD} and $v_{AU,CC}$, respectively, for 50% and 125% model uncertainty (u_{CC}) under climate change (a) case 1 ($\Delta_\mu = 0.0008u_{CC}$, $\Delta_\sigma = 0.004u_{CC}$) and (b) case 2 ($\Delta_\mu = 0.0016u_{CC}$, $\Delta_\sigma = 0.004u_{CC}$) for 14 Canadian cities.

Figure 4.5 shows that the average design wind speed over the 14 stations will increase by 9.0 km h^{-1} for case 1, and 14 km h^{-1} for case 2, relative to the current value of v_{FD}, if the model uncertainty is assumed to be 50%. If the proposed values of m_{AU} for 125% model uncertainty are adopted, the average design wind speed will increase by 12 km h^{-1} for case 1, and 19 km h^{-1} for case 2, relative to the current v_{FD}.

Figures 4.6 and 4.7 show the 50-year exceedance probabilities, p_{50}, of the design wind speeds for the 14 stations shown in Fig. 4.5. As in Figs. 3.5 and 3.6, the probability that $v_{AU,CC}$ is exceeded over 50 years is determined using eq. (1.47), where $F_{v_{A1}}(r;y)$ is the non-stationary Gumbel distribution which includes annual relative increases in the mean and standard deviation, Δ_μ and Δ_σ, respectively. Figures 4.6(a) and (b) show p_{50} for climate change case 1 assuming (a) 50% and (b) 125% model uncertainty. The blue squares show p_{50} if the recommended design wind speeds for 50% model uncertainty are adopted, while the cyan squares demonstrate that for 125% model uncertainty. The purple squares show p_{50} if the current design wind speeds are used under climate change case 1, and the black circles denote the current 50-year exceedance probability levels for reference.

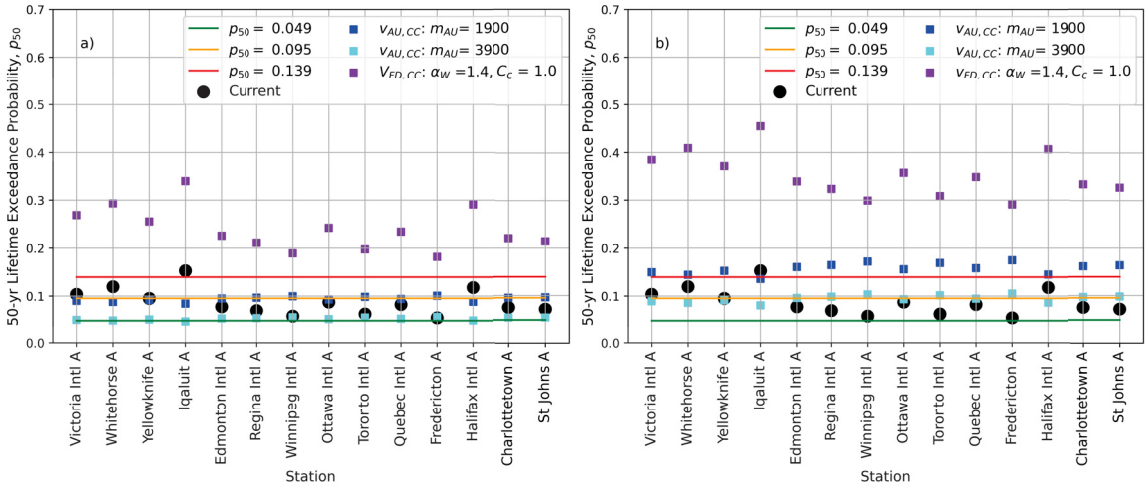

Figure 4.6: Fifty-year exceedance probability of $v_{AU,CC}$ for the AURP method, under climate change case 1 ($\Delta_\mu = 0.0008u_{CC}$, $\Delta_\sigma = 0.004u_{CC}$) assuming (a) 50% model uncertainty ($u_{CC} = 1.5$) and (b) 125% model uncertainty ($u_{CC} = 2.25$) for 14 Canadian cities.

Figures 4.7(a) and (b) are similar to 4.6(a) and (b), but show p_{50} for climate change case 2 assuming 50% and 125% model uncertainty, respectively.

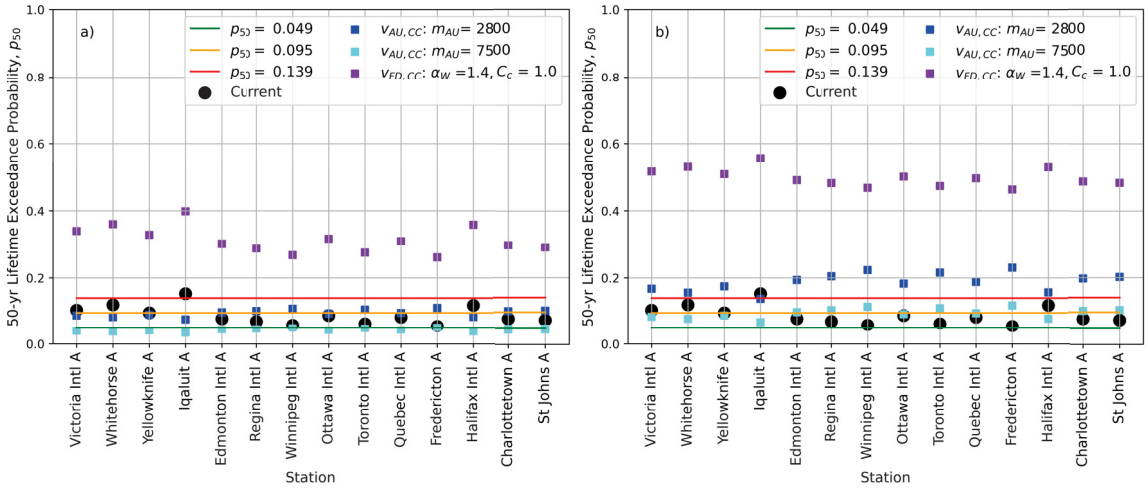

Figure 4.7: Fifty-year exceedance probability of $v_{AU,CC}$ for the AURP method, under climate change case 2 ($\Delta_\mu = 0.0016u_{CC}$, $\Delta_\sigma = 0.004u_{CC}$) assuming (a) 50% model uncertainty ($u_{CC} = 1.5$) and (b) 125% model uncertainty ($u_{CC} = 2.25$) for 14 Canadian cities.

The all-inclusive return periods, m_{AU}, in Figures 4.6 and 4.7 were selected so that the realized 50-year exceedance probability is reduced under climate change compared to

p_{50} achieved using the current factored design wind speeds under climate change (i.e., $v_{FD,CC}$ where $\alpha_W = 1.4$ and $C_c = 1.0$, shown in purple). Figures 4.6 and 4.7 show that the design wind speeds selected in Fig. 4.5 achieve the expected 50-year exceedance probabilities. That is, p_{50} for the design wind speeds recommended for 50% model uncertainty (blue squares) are approximately equal to 0.095 (orange lines) when 50% model uncertainty is realized in the future, as shown in Figs. 4.6(a) and 4.7(a). Similarly, Figs. 4.6(b) and 4.7(b) demonstrate that p_{50} for the 125% model uncertainty design wind speeds (cyan squares) are also approximately equal to 0.095 (orange lines) when 125% model uncertainty is realized in the future. If the 125% model uncertainty design wind speeds are adopted and only 50% uncertainty is realized in the future, p_{50} at the 14 locations will be approximately 0.049 (green line) under both climate change cases 1 and 2, see Figs. 4.6(a) and 4.7(a), respectively. Meanwhile, if the 50% uncertainty design wind speeds are adopted and 125% model uncertainty is realized in the future, p_{50} will be at or above the maximum 50-year exceedance probability target, $p_{50} = 0.139$, at all locations, as shown in Figs. 4.6(b) and 4.7(b).

Figures 4.6 and 4.7 also demonstrate that there is higher variability between locations in p_{50} as Δ_μ and Δ_σ increase. For example, there is higher variability between the blue squares in Fig. 4.7(b) when $\Delta_\mu = 0.0036$ and $\Delta_\sigma = 0.009$ (i.e., climate change case 2 with 125% model uncertainty), than between those in Fig. 4.6(a) when $\Delta_\mu = 0.0012$ and $\Delta_\sigma = 0.006$ (i.e., climate change case 1 with 50% model uncertainty). This increase in variability is consistent with the results in Fig 4.3(a), which shows the values of m_{AU} required to achieve $p_{50} = 0.095$ at $\Delta_\mu = 0.001$, 0.002, 0.003 and 0.004. Fig 4.3(a) shows there is higher variability in m_{AU} between locations when $\Delta_\mu = 0.004$, than when $\Delta_\mu = 0.001$. Note that climate change case 2 with 125% model uncertainty (where $\Delta_\mu = 0.0036$) is similar to the largest change in mean shown in Fig 4.3(a) (i.e., $\Delta_\mu = 0.004$ shown in magenta), while climate change case 1 with 50% model uncertainty (where $\Delta_\mu = 0.0012$) is similar to the smallest change in mean shown in Fig 4.3(a) (i.e., $\Delta_\mu = 0.001$ shown in purple).

Figure 4.8 shows the average 50-year exceedance probability, p_{50}, over the 14 locations in Figs. 4.6 and 4.7. Figure 4.8(a) and (b) show the results for climate change cases 1 and 2, respectively, for $1.0 \leq u_{CC} \leq 2.25$.

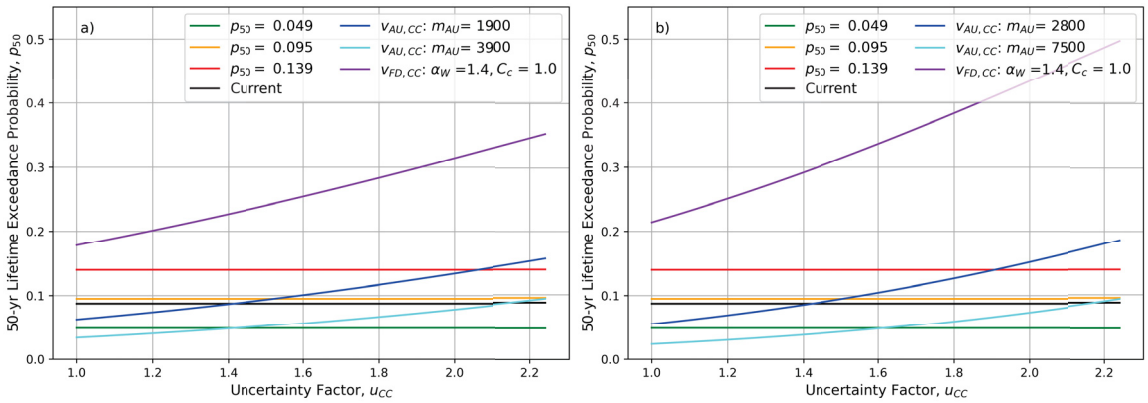

Figure 4.8: Average 50-year exceedance probability of $v_{AU,CC}$ over 14 Canadian cities for the AURP method, where the uncertainty factor, u_{CC}, ranges from 1.0 to 2.25 under climate change (a) case 1 and (b) case 2.

Figure 4.8 shows similar results to those of Fig. 3.7. The purple lines demonstrate that the 50-year exceedance probability will increase significantly under climate change if new design wind speeds are not adopted. Even under climate change case 1 with 50% model uncertainty (i.e., $\Delta_\mu = 0.0012$ and $\Delta_\sigma = 0.006$) the average 50-year exceedance probability would increase 174%, from 0.088 under current conditions to 0.24. Figure 4.8 also shows that if the design wind speeds recommended for 50% model uncertainty are adopted (blue lines), p_{50} will remain under the maximum target (i.e., $p_{50} = 0.139$) for $u_{CC} \leq 2.06$ for climate change case 1, and for $u_{CC} \leq 1.90$ for climate change case 2. Using the design wind speeds recommended for 125% uncertainty (cyan lines) results in p_{50} increasing towards the mid-level target (i.e., $p_{50} = 0.095$) as u_{CC} increases towards 2.25 for both climate change cases. However, using the 125% uncertainty design wind speeds will result in over-design (i.e., $p_{50} < 0.049$) when $u_{CC} \leq 1.41$ for climate change case 1, and $u_{CC} \leq 1.61$ for climate change case 2.

The Hybrid Ultimate Return Period design method was developed to potentially improve exceedance probability consistency across Canada. As demonstrated in Fig. 4.3, the All-Inclusive Ultimate Return Period method does not lead to consistent exceedance probabilities across Canada when the mean of V_{A1} increases over time. The HURP method is a hybrid method where m_{HU} only accounts for increases in $\sigma_{v_{A1}}$, while $C_{c,HU}$ accounts for increases in $\mu_{v_{A1}}$. Figure 4.9 shows the average value of m_{HU} over the 14 Canadian cities listed in Table 3.1 required to achieve 50-year

exceedance probability targets $p_{50} = 0.049$, 0.095 and 0.139. As discussed in Section 4.3.1 m_{HU} is evaluated with $\Delta_\mu = 0$ and $\Delta_\sigma > 0$. Since Δ_σ is the same for both climate change cases, the results in Fig. 4.9 represent those for both climate change cases 1 and 2.

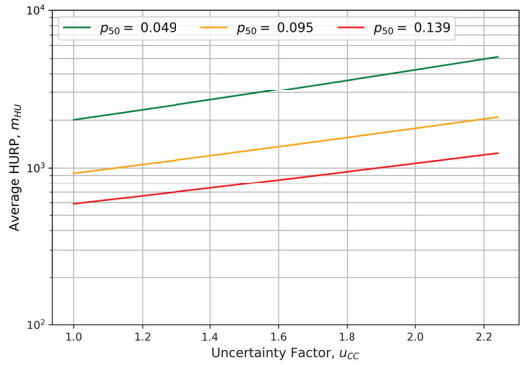

Figure 4.9: Average hybrid ultimate return period, m_{HU}, over 14 Canadian cities required to achieve target 50-year exceedance probability p_{50} under climate change cases 1 and 2 ($\Delta_\sigma = 0.004u_{CC}$) for $1.0 \leq u_{CC} \leq 2.25$.

Figure 4.9 demonstrates that the updated hyrbid method ultimate return periods to be used under climate change, m_{HU}, are significantly higher than the current ultimate return period, $m_U = 500$, determined in Section 4.2. However, the values of m_{HU} are substantially lower than the m_{AU} results in Fig. 4.4, since m_{HU} only accounts for changes in the standard deviation of V_{A1}, and does not account for changes in the mean as well. For example, to achieve $p_{50} = 0.049$ in climate change case 2 with 125% model uncertainty, $m_{AU} = 18793$ years (see Fig. 4.4b), but m_{HU} is only 5158 years, as shown in Fig. 4.9. Note that the HURP design wind speeds do not vary much from the AURP design wind speeds, as discussed shortly, since the HURP method has an additional factor, $C_{c,HU}$.

Figure 4.10 shows the average values of $C_{c,HU}$ over the 14 Canadian cities in Table 3.1 required to achieve the 50-year exceedance probability targets $p_{50} = 0.049$, 0.095 and 0.139. Figures 4.10(a) and (b) show the results for climate change cases 1 and 2, respectively.

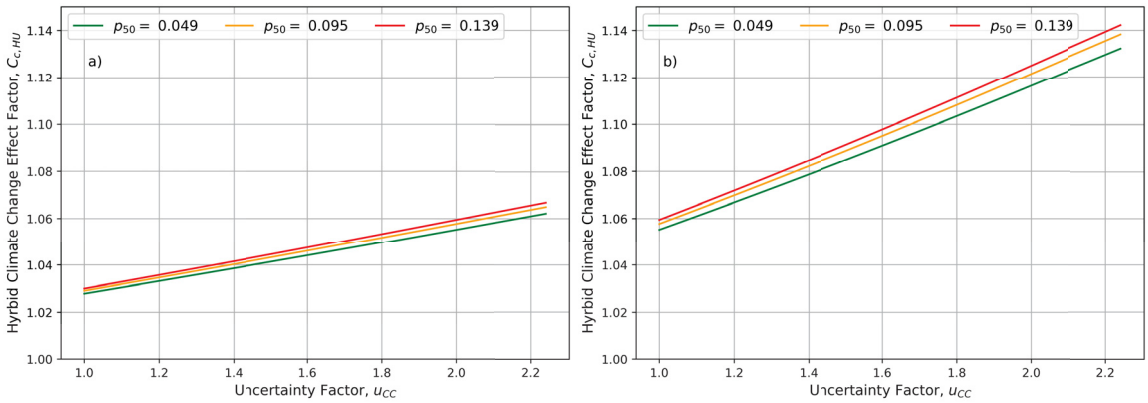

Figure 4.10: Average climate change effect factor, $C_{c,HU}$, over 14 Canadian cities required to achieve target 50-year exceedance probability p_{50} under climate change cases (a) 1 ($\Delta_\mu = 0.0008u_{CC}$) and (b) 2 ($\Delta_\mu = 0.0016u_{CC}$) for $1.0 \leq u_{CC} \leq 2.25$.

Figure 4.10 demonstrates that for each climate change case $C_{c,HU}$ is approximately equal for each of the three 50-year exceedance probability targets. For example, under climate change case 2 with 125% uncertainty $C_{c,HU} = 1.14$ is required to achieve $p_{50} = 0.049$, while $C_{c,HU} = 1.13$ achieves $p_{50} = 0.139$. Recall that $C_{c,HU}$ is the squared ratio of v_{CC} to v_{A1,m_U}, where v_{CC} and v_{A1,m_U} are the wind speeds with 50-year exceedance probabilities equal to the same target under climate change and under current conditions, respectively. Therefore, $C_{c,HU}$ is the factor the current wind pressure needs to be increased by to maintain the current exceedance probability under climate change.

Consistent with the AURP method results, the mid-level exceedance probability target (i.e., $p_{50} = 0.095$) is used to determine recommended design parameters for the HURP method. Figures 4.9 and 4.10 are used to determine the values of m_{HU} and $C_{c,HU}$, respectively, required for climate change cases 1 and 2, assuming both 50% and 125% model uncertainty. For simplicity, the values of m_{HU} are rounded to the nearest hundred, while the values of $C_{c,HU}$ are round to the nearest hundredth. For climate change case 1 with 50% model uncertainty, it is recommended that $m_{HU} = 1300$ and $C_{c,HU} = 1.04$, while for case 1 with 125% model uncertainty it is recommended that $m_{HU} = 2100$ and $C_{c,HU} = 1.07$. For climate change case 2, $m_{HU} = 1300$ and $C_{c,HU} = 1.09$ assuming 50% model uncertainty, while $m_{HU} = 2100$ and $C_{c,HU} = 1.14$ for 125% model uncertainty. Figure 4.11 shows the future design wind speeds to be used under climate change calculated using these recommended design parameters.

The future HURP design wind speed is $v_{HU,CC} = \sqrt{C_{c,HU}} v_{A1,m_{HU}}$. Figures 4.11(a) and (b) show the results for climate change cases 1 and 2, respectively. The current factored design wind speeds, v_{FD} (black squares), are included for reference.

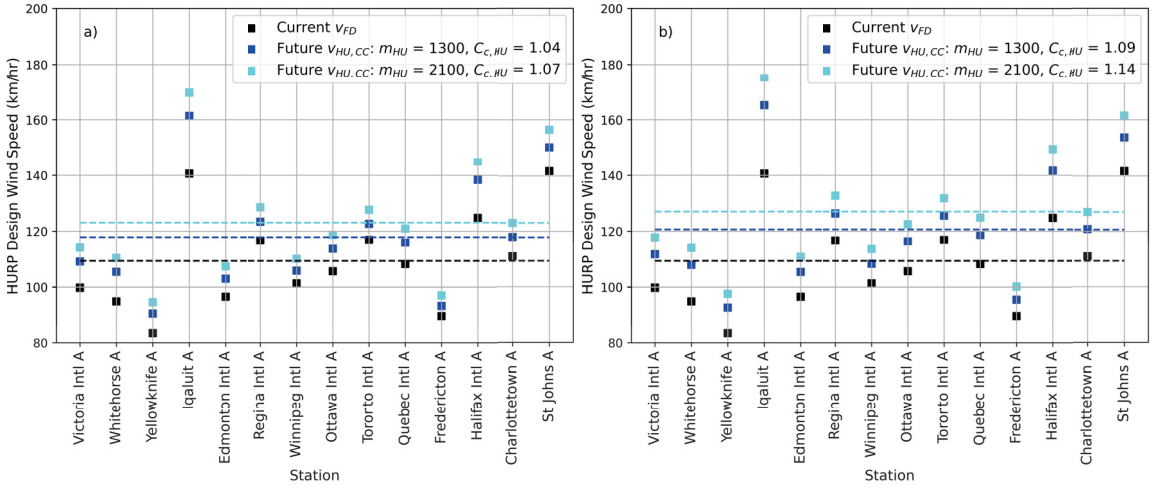

Figure 4.11: Current design wind speeds and future HURP design wind speeds, v_{FD} and $v_{HU,CC}$, respectively, for 50% and 125% model uncertainty (u_{CC}) under climate change (a) case 1 ($\Delta_\mu = 0.0008 u_{CC}$, $\Delta_\sigma = 0.004 u_{CC}$) and (b) case 2 ($\Delta_\mu = 0.0016 u_{CC}$, $\Delta_\sigma = 0.004 u_{CC}$) for 14 Canadian cities.

Figure 4.11 shows that under climate change case 1, the average future HURP design wind speed, $v_{HU,CC}$, over the 14 stations will increase 8.5 km h^{-1} assuming 50% model uncertainty and will increase 14 km h^{-1} assuming 125% model uncertainty, relative to the current average factored design wind speed, v_{FD}. For climate change case 2, the average $v_{HU,CC}$ will increase 11 km h^{-1} and 18 km h^{-1}, assuming 50% and 125% model uncertainty, respectively, relative to v_{FD}.

The 50-year exceedance probabilities, p_{50}, of the future design wind speeds, $v_{HU,CC}$, shown in Fig. 4.11 were then determined using eq. (1.47), where $F_{v_{A1}}(r; y)$ is the non-stationary Gumbel distribution defined by yearly relative increases in the mean and standard deviation, Δ_μ and Δ_σ, respectively. Figures 4.12(a) and (b) show p_{50} for the 14 Canadian cities under climate change case 1 assuming 50% and 125% model uncertainty, respectively. The blue and cyan squares show p_{50} when the design parameters recommended for 50% and 125% model uncertainty, respectively, are used. The purple squares show p_{50} when the current factored design wind speeds, v_{FD}, are used under climate change, while the black circles show p_{50} for v_{FD} under current

conditions.

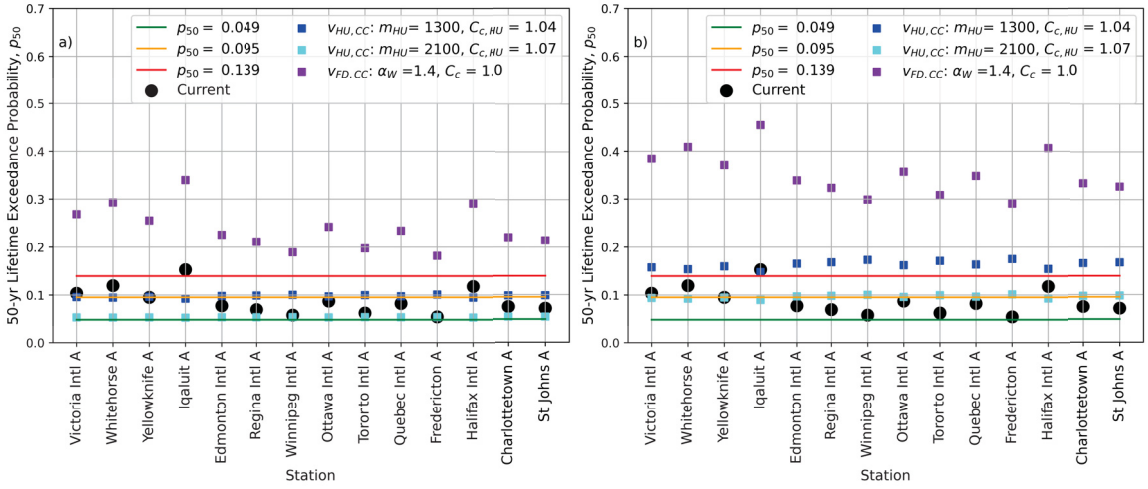

Figure 4.12: Fifty-year exceedance probability of $v_{HU,CC}$ for the HURP method, under climate change case 1 ($\Delta_\mu = 0.0008u_{CC}$, $\Delta_\sigma = 0.004u_{CC}$) assuming (a) 50% model uncertainty ($u_{CC} = 1.5$) and (b) 125% model uncertainty ($u_{CC} = 2.25$) for 14 Canadian cities.

Similarly, Figs. 4.13(a) and (b) show the 50-year exceedance probabilities, but for climate change case 2 with 50% and 125% model uncertainty, respectively.

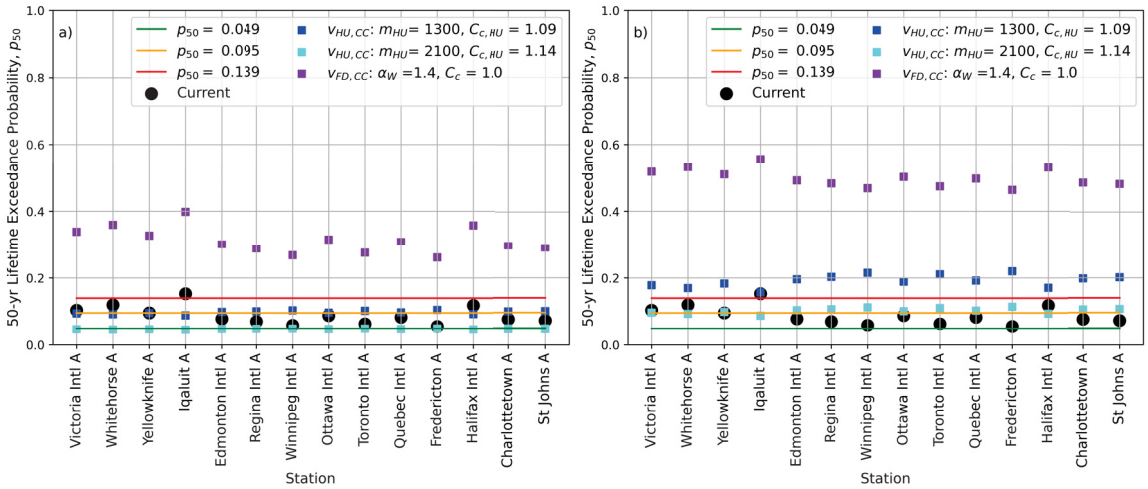

Figure 4.13: Fifty-year exceedance probability of $v_{HU,CC}$ for the HURP method, under climate change case 2 ($\Delta_\mu = 0.0016u_{CC}$, $\Delta_\sigma = 0.004u_{CC}$) assuming (a) 50% model uncertainty ($u_{CC} = 1.5$) and (b) 125% model uncertainty ($u_{CC} = 2.25$) for 14 Canadian cities.

In Figs. 4.12 and 4.13, the design parameters for the blue squares were selected

using an exceedance probability target of $p_{50} = 0.095$ under 50% model uncertainty, while the design parameters for the cyan squares were selected to achieve the same exceedance probability target, $p_{50} = 0.095$, but under 125% model uncertainty. Figs. 4.12(a) and 4.13(a), which show climate change cases 1 and 2 with 50% model uncertainty, demonstrate that the blue squares are all approximately equal to 0.095. While, the cyan squares are all approximately equal to 0.095 in Figs. 4.12(b) and 4.13(b), which show climate change cases 1 and 2 with 125% model uncertainty. This demonstrates that the realized 50-year exceedance probabilties are approximately equal to the target p_{50}, assuming the predicted climate change scenario is realized in the future.

Similar to the AURP method results (see Figs. 4.6 and 4.7), the 125% uncertainty HURP design wind speeds result in p_{50} near the minimum target (0.049) when 50% uncertainty is realized in the future, and the 50% uncertainty HURP design wind speeds results in p_{50} above the maximum target (0.139) when 125% uncertainty is realized in the future. It can also be seen, in Figs. 4.12 and 4.13 there there appears to be less variability between locations compared to when the AURP method is used. For example, there is less variability between the blue squares in Fig. 4.13(b) than between those in Fig. 4.7(b). The variability between locations in p_{50} is quantitatively assessed in Section 5.1.

Figure 4.14 shows the average value of p_{50} over the 14 locations in Figs. 4.12 and 4.13. Figure 4.14(a) shows the results for climate change case 1 for $1.0 \leq u_{CC} \leq 2.25$, while Fig. 4.14(b) shows that for climate change case 2.

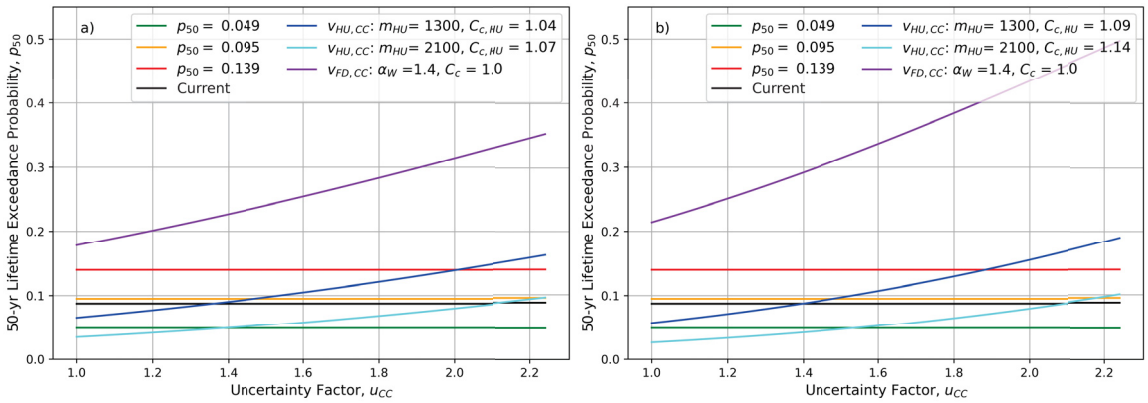

Figure 4.14: Average 50-year exceedance probability of $v_{HU,CC}$ over 14 Canadian cities for the HURP method, where the uncertainty factor, u_{CC}, ranges from 1.0 to 2.25 under climate change (a) case 1 and (b) case 2.

The results of Fig. 4.14 are similar to those for the LRFD climate change method (see Fig. 3.7) and the AURP method (see Fig. 4.8). Figure 4.14 shows that for $u_{CC} \geq 2.01$ under climate change case 1 and for $u_{CC} \geq 1.89$ under climate change case 2, the maximum p_{50} target (0.139) will be exceeded if the 50% uncertainty design wind speeds are adopted. If the 125% uncertainty design wind speeds are adopted, p_{50} will remain below the maximum target (0.139), and will only reach the mid-level target as u_{CC} approaches 2.25. However, adopting the 125% uncertainty design wind speeds will result in over-design (i.e., $p_{50} < 0.049$) for $u_{CC} \leq 1.38$ and $u_{CC} \leq 1.53$ under climate change cases 1 and 2, respectively.

Chapter 5

Discussion

5.1 Comparison of Design Methodologies

The objective of this thesis is to develop a future wind loading design methodology that (a) maintains the current 50-year lifetime exceedance probabilities under climate change, and (b) improves the 50-year exceedance probability consistency across Canada. This section compares how well the three wind loading design methods proposed in this thesis (i.e., the LRFD based method and the two ultimate return period based methods) are able to achieve these objectives.

Figure 5.1(a) shows the average future design wind speed over the 14 stations for each wind loading design method under the four climate change scenarios: (1) climate change case 1 with 50% model uncertainty, (2) climate change case 1 with 125% model uncertainty, (3) climate change case 2 with 50% model uncertainty and (4) climate change case 2 with 125% model uncertainty. The purple squares show the future design wind speeds determined using the LRFD method, $v_{FD,CC}$, while the cyan and magenta squares show the design wind speeds determined using the AURP method ($v_{AU,CC}$) and the HURP method ($v_{HU,CC}$), respectively. Recall that the LRFD design parameters (i.e., C_c and α_W) were selected to achieve the current values of p_{50} (i.e., $p_{50} = 0.088$, on average), and that AURP and HURP design parameters (i.e., m_{AU}, m_{HU} and $C_{c,HU}$) were selected to achieve the mid-level p_{50} target used in this thesis (i.e., 0.095). The current average factored design wind speed, v_{FD}, is shown as the black line for reference and was determined as the average value of v_{FD} for the 14 Canadian cities given in Table 3.2. Figure 5.1(b) then shows the 50-year exceedance probabilities for the design wind speeds in Fig. 5.1(a). The maximum, mid-level and minimum p_{50} targets used throughout this thesis are included for reference as the red, orange and green lines, respectively. The current average value of p_{50} (shown as the black line) was determined by considering the current 50-year exceedance probabilities for the 14 Canadian cities shown in Fig. 3.1, which are for the case of

no climate change.

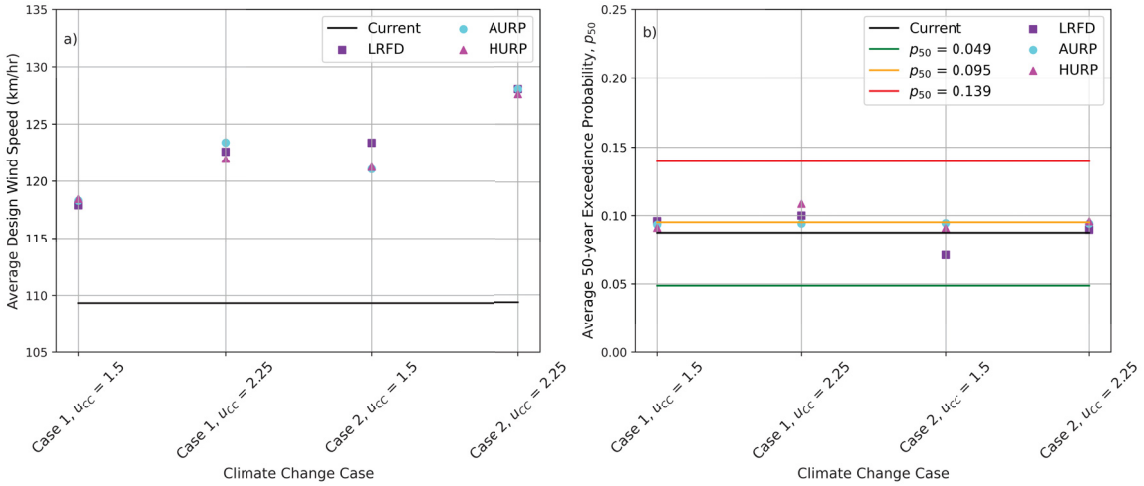

Figure 5.1: Comparison of the average (a) future design wind speeds and (b) fifty-year exceedance probabilities, p_{50}, over 14 Canadian stations for the three proposed climate change design methodologies.

Figure 5.1 demonstrates that on average all three wind loading design methods achieve very similar design wind speeds under each climate change scenario. Consequently, the corresponding average 50-year exceedance probabilities of the three design methods are also very similar. The slight discrepancies between the design methods in Fig. 5.1 are caused by the rounding of wind loading design parameters for simplicity. Therefore, the results of Fig. 5.1 demonstrate that all three wind loading design methods achieve the first objective of this thesis. That is, the current 50-year exceedance probabilities will be maintained under the projected changes to wind speed distributions due to climate change.

Two metrics are then used to evaluate how well the design methods meet the second objective of this thesis: improving 50-year exceedance probability consistency across Canada. The first metric is the standard deviation of p_{50} over all 14 stations under a given climate change scenario. Figure 5.2(a) shows the standard deviation of each of the three wind loading design methods under the same four climate change scenarios as shown in Fig. 5.1. The second metric is the difference in magnitude between the maximum and average value of p_{50} over the 14 stations under a given climate change scenario (shown in Figure 5.2b). As in Fig. 5.1(b), the current values of both p_{50} consistency metrics (black lines in Fig. 5.2) are determined using the current

values of p_{50} (see in Fig. 3.1), which are computed assuming no climate change.

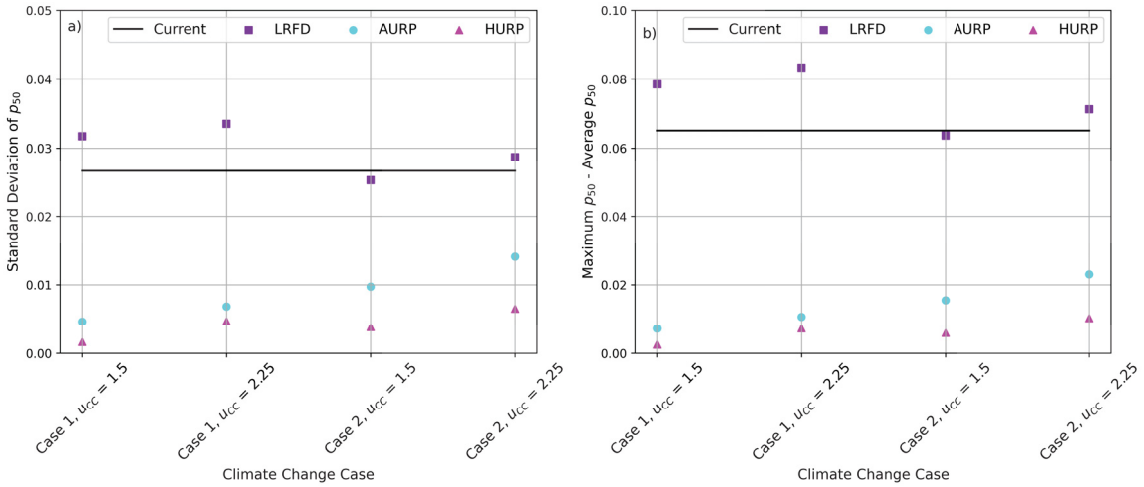

Figure 5.2: Comparison of the fifty-year exceedance probability (a) standard deviation and (b) maximum deviation from the mean using the three proposed climate change design methodologies.

Figure 5.2 demonstrates that based on both metrics the Hybrid Ultimate Return Period method achieves the most consistent exceedance probability levels under all four climate change scenarios. The average standard deviation for the AURP method over the four climate change scenarios is 0.009, while that for the HURP method is 0.004. Additionally, the average difference between the maximum and average value of p_{50} is 0.014 for the AURP method, and 0.007 for the HURP method. This demonstrates that accounting for increases in $\sigma_{v_{A1}}$ (using $v_{A1,m_{HU}}$) separately from increases in $\mu_{v_{A1}}$ (using $C_{c,HU}$) leads to improved consistency in p_{50} across Canada, compared to accounting for increases in $\mu_{v_{A1}}$ and $\sigma_{v_{A1}}$ simultaneously using the ultimate return period wind speed, $v_{A1,m_{AU}}$. Note that Hong et al. (2016) demonstrated that under current, stationary conditions the LRFD method exceedance probability variability, due to the range of $\text{CV}_{v_{A1}}$ values, is greater than that of the ultimate return period method, due to sample size effect, for return periods ranging from 500 to 700 years. This study does not further investigate the uncertainty in the HURP method design wind speeds due to large return period values, m_{HU}, but it is assumed that the aforementioned results from Hong et al. (2016) still hold under climate change.

In addition to improved exceedance probability consistency, the HURP design method has other benefits that make it a more preferable wind loading design method

compared to the AURP method. Notably, there is less uncertainty in estimates of $v_{A1,m_{HU}}$ than in estimates of $v_{A1,m_{AU}}$, since estimates of larger return period wind speeds have higher uncertainties due to lack of historical records and sampling error (see Section 4.3). Recall from Section 4.3.2 that m_{HU} values are substantially lower than values of m_{AU}, since m_{HU} only accounts for increases in $\sigma_{V_{A1}}$, as opposed to increases in both $\mu_{V_{A1}}$ and $\sigma_{V_{A1}}$. An additional benefit of the HURP method is that it allows for simpler adjustment of the wind loading design parameters, $C_{c,HU}$ and m_{HU}, as climate change projections continue to change and improve over time. For the AURP method a different design parameter, m_{AU}, is used for each combination of possible values of Δ_μ and Δ_σ. While, for the HURP method there is one value of $C_{c,HU}$ for each possible increase in $\mu_{V_{A1}}$ (Δ_μ), and one value of m_{HU} for each possible increase in $\sigma_{V_{A1}}$ (Δ_σ).

Based on this comparison, the HURP method is considered the best overall wind loading design method to be used under climate change out of the three methods proposed in this thesis. It should be used by the NBCC in the future, since it is a simple method that improves exceedance probability consistency while also limiting estimation error.

5.2 Sensitivity of HURP Design Parameters to Target Exceedance Probability

This section assesses the effect of the target exceedance probability on the Hybrid Ultimate Return Period method design parameters, and the resulting design wind speeds. The effects of the target p_{50} on the AURP and LRFD methods are not evaluated because the HURP method is considered the best wind loading design method to be used under climate change (see Section 5.1). Recall that Section 4.3.2 only showed the design parameters required to achieve the mid-level 50-year exceedance probability target (i.e., $p_{50} = 0.095$). Although the mid-level p_{50} target is close to the current average 50-year exceedance probability (i.e., 0.088), the mid-level p_{50} target may or may not be the most appropriate p_{50} target for the NBCC. As shown in Fig. 3.1, the probability that the current factored design wind speed, v_{FD}, is exceeded over 50-years varies from a maximum of 0.153 in Iqaluit, to a minimum of 0.055 in Fredericton. Since the current NBCC design values are considered to be acceptable

by society, it would be reasonable to adopt a p_{50} target in the NBCC anywhere within the range $0.055 \leq p_{50} \leq 0.153$. As previously stated, the aim of this thesis is not to recommend target reliability levels for the NBCC, but to recommend design methods and parameters that achieve a given exceedance probability target under climate change. Therefore, this section shows the design parameters and resulting design wind speeds required to meet 50-year exceedance probability targets in the range $0.049 \leq p_{50} \leq 0.139$. This range of p_{50} targets is selected because it is the range that has been considered throughout the rest of this thesis, and is the range that corresponds to stationary, annual exceedance probability targets of $p_e = 0.003$ to 0.001. Note that it is also more conservative than the current range of $0.055 \leq p_{50} \leq 0.153$.

Figure 5.3 shows how the hybrid ultimate return period, m_{HU}, varies as the p_{50} target increases from 0.049 to 0.139. The minimum, mid-level and maximum p_{50} targets used throughout this thesis are shown as the green, orange and red lines, respectively. Since climate change cases 1 and 2 both project the same rate of increase in $\sigma_{V_{A1}}$, Fig. 5.3 shows m_{HU} when $\Delta_\mu = 0$ and $\Delta_\sigma = 0.004 u_{CC}$, for $u_{CC} = 1.5$ and 2.25. Note that the hybrid ultimate return period, m_{HU}, is determined when $\Delta_\mu = 0$ and $\Delta_\sigma > 0$ (see Section 4.3.1).

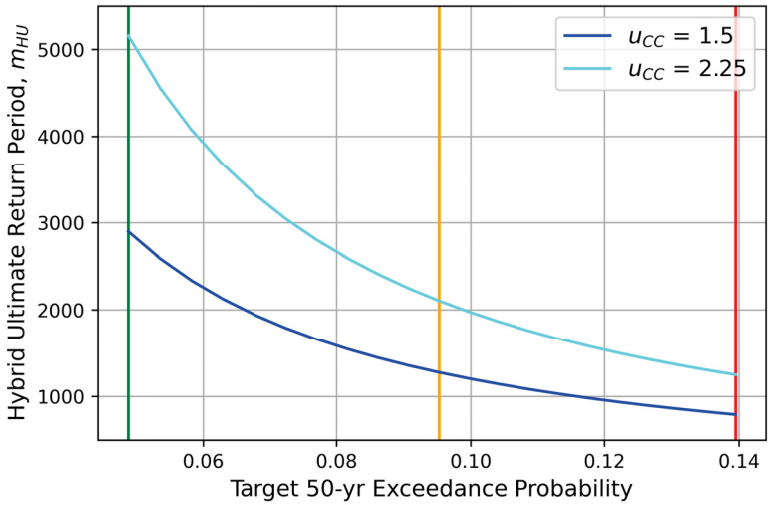

Figure 5.3: Sensitivity of the hybrid ultimate return period, m_{HU}, to the 50-year target exceedance probability when $\Delta_\mu = 0$ and $\Delta_\sigma = 0.004 u_{CC}$.

Figure 5.3 demonstrates that m_{HU} increases rapidly as the target p_{50} decreases. For example, assuming $u_{CC} = 2.25$, $m_{HU} = 5158$ when $p_{50} = 0.049$, $m_{HU} = 2104$ when

$p_{50} = 0.095$ and $m_{HU} = 1249$ when $p_{50} = 0.139$. If model uncertainty is only 50% (i.e., $u_{CC} = 1.5$), m_{HU} is significantly lower than when $u_{CC} = 2.25$ and, m_{HU} increases less as the target p_{50} decreases. Assuming $u_{CC} = 1.5$, $m_{HU} = 2899$ when $p_{50} = 0.049$, $m_{HU} = 1276$ when $p_{50} = 0.095$ and $m_{HU} = 791$ when $p_{50} = 0.139$.

Figure 5.4 shows how $C_{c,HU}$ varies with the target p_{50} for climate change cases (a) 1 and (b) 2, for $u_{CC} = 1.5$ and 2.25. The hybrid climate change effect factor, $C_{c,HU}$, is the squared ratio of v_{CC} to v_{A1,m_U}, where v_{CC} and v_{A1,m_U} are the wind speeds with 50-year exceedance probabilities equal to the same target under climate change and under current conditions, respectively. Recall that v_{CC} is calculated when $\Delta_\mu > 0$ and $\Delta_\sigma = 0$ (see Section 4.3.1). Under climate change case 1 $\Delta_\mu = 0.0008 u_{CC}$ and, $\Delta_\mu = 0.0016 u_{CC}$ under climate change case 2.

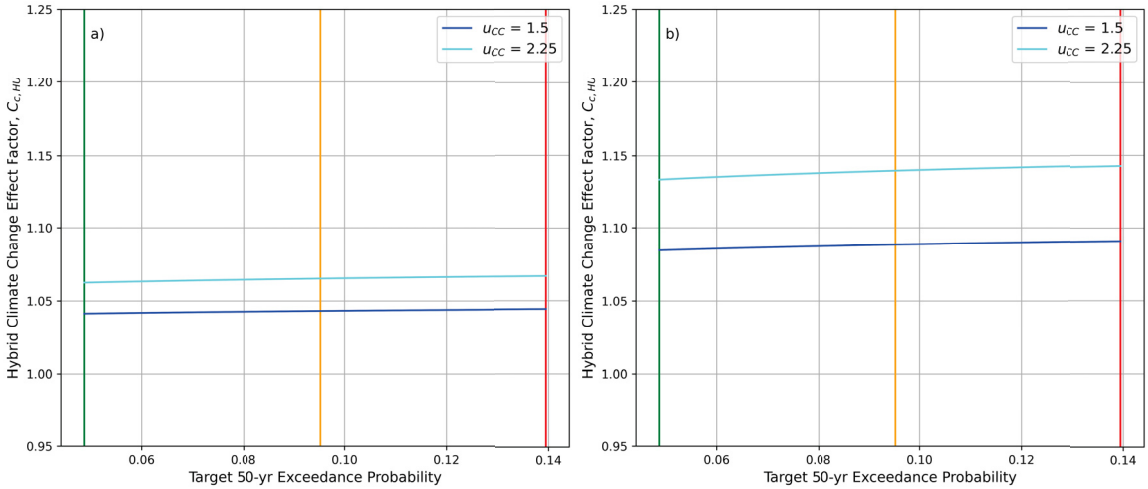

Figure 5.4: Sensitivity of the hyrbid climate change effect factor, $C_{c,HU}$, to the 50-year target exceedance probability for climate change cases (a) 1 ($\Delta_\mu = 0.0008 u_{CC}$) and (b) 2 ($\Delta_\mu = 0.0016 u_{CC}$) when $\Delta_\sigma = 0$.

Figure 5.4 demonstrates that the target p_{50} does not have a significant effect on $C_{c,HU}$. There is very minimal change in $C_{c,HU}$ as the target p_{50} increases from 0.049 to 0.139, under both climate change cases 1 and 2, assuming 50% or 125% model uncertainty. The largest change occurs under climate change case 2 with 125% model uncertainty. Under this climate change scenario $C_{c,HU} = 1.133$ when $p_{50} = 0.049$, $C_{c,HU} = 1.139$ when $p_{50} = 0.095$ and $C_{c,HU} = 1.142$ when $p_{50} = 0.139$. The total change even in this most extreme climate change scenario is less than 0.01, therefore, the effect of the target p_{50} on $C_{c,HU}$ is considered negligible. The hybrid climate change effect

factor, $C_{c,HU}$, does not significantly change with the target p_{50} because it is defined as the squared ratio of the wind speed, v_{CC}, evaluated under climate change conditions to the wind speed, v_{A1,m_U}, evaluated under current conditions, where both v_{CC} and v_{A1,m_U} have the same 50-year exceedance probability. The target p_{50} is accounted for in both the numerator and denominator of this ratio, therefore, the value of the target p_{50} has a negligible effect on $C_{c,HU}$.

Figure 5.5 shows the HURP design wind speed, determined as $v_{HU,CC} = \sqrt{C_{c,HU}} v_{A1,m_{HU}}$, calculated using the values of m_{HU} and $C_{c,HU}$ shown in Figs. 5.3 and 5.4, respectively. Figures 5.5(a) and (b) demonstrate the effect of the target p_{50} on $v_{HU,CC}$ under climate change cases 1 and 2, respectively. The black line shows the current average factored design wind speed over the 14 Canadian cities in Table 3.1 (i.e., $v_{FD} = 109\,\mathrm{km\,h^{-1}}$).

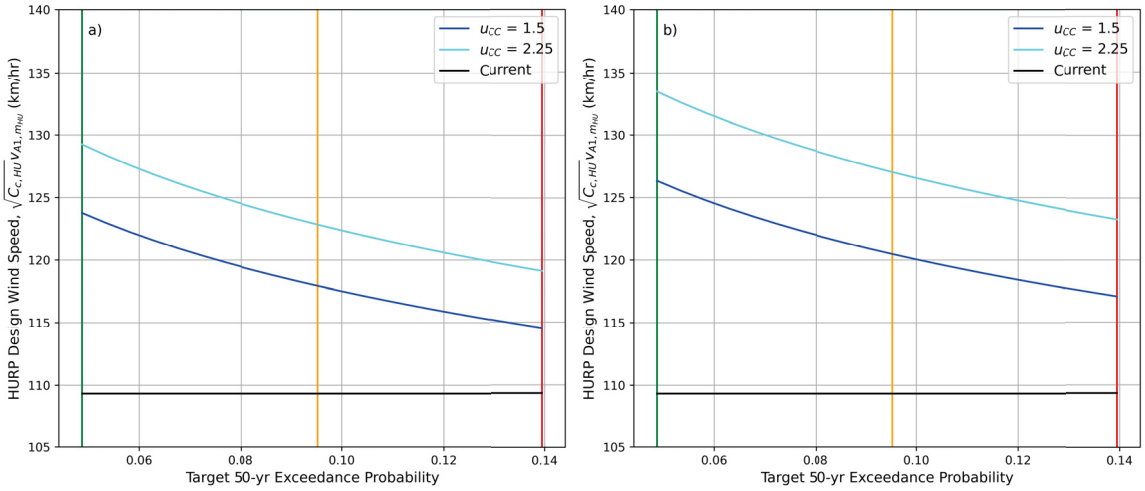

Figure 5.5: Sensitivity of the HURP design wind speed (i.e., $\sqrt{C_{c,HU}} v_{A1,m_{HU}}$) to the 50-year target exceedance probability for climate change cases (a) 1 and (b) 2.

For both climate change cases 1 and 2, Fig. 5.5 demonstrates that at a given target p_{50}, the difference between $v_{HU,CC}$ when model uncertainty is 50% and that when model uncertainty 125% remains approximately constant over the entire range of p_{50} target values from 0.049 to 0.139. Under climate change case 1 the maximum difference between $v_{HU,CC}$ when $u_{CC} = 1.5$ and $v_{HU,CC}$ when $u_{CC} = 2.25$ is $5.5\,\mathrm{km\,h^{-1}}$ and the minimum difference is $4.6\,\mathrm{km\,h^{-1}}$, while for case 2 the maximum difference is $7.1\,\mathrm{km\,h^{-1}}$ and the minimum difference is $6.2\,\mathrm{km\,h^{-1}}$. Figure 5.5 also demonstrates that the total increase in $v_{HU,CC}$ from a target p_{50} of 0.139 to 0.049, is very similar in all four of the climate change scenarios shown. Assuming 50% model uncertainty,

$v_{HU,CC}$ increases 9 km h^{-1}, from 115 km h^{-1} to 124 km h^{-1} under climate change case 1, and also increases 9 km h^{-1}, from 117 km h^{-1} to 126 km h^{-1} under climate change case 2. While, assuming 125% model uncertainty, $v_{HU,CC}$ increases 10 km h^{-1}, from 119 km h^{-1} to 129 km h^{-1} under climate change case 1, and also increases 10 km h^{-1}, from 123 km h^{-1} to 133 km h^{-1} under climate change case 2.

5.3 Effect of Design Life on Wind Design Requirements Under Climate Change

It is important to consider the difference between the real lifetime of a structure and the design working life defined by structural codes. In the NBCC the design lifetime is 50 years, during which time the structure should meet, without major interventions or repairs, the intended time-dependent performances (Croce et al., 2019). However, it is evident in practice that the real lifetime of a well-maintained structure is significantly greater, and consequently, the structure will be more susceptible to the effects of climate change (Croce et al., 2019). This section aims to assess the effect of climate change on design wind speed exceedance probabilities over design lifetimes of 50 to 100 years.

Figure 5.6 shows the average probability that the current factored design wind speed, v_{FD}, is exceeded under current (stationary) conditions over 14 Canadian cities during a d-year lifetime for the range $50 \leq d \leq 100$. The d-year minimum, mid-level and maximum target exceedance probabilities are shown as the green, orange, and red lines, respectively. The d-year exceedance probability is evaluated as $p_d = 1-(1-p_e)^d$, where d is the design lifetime, and p_e is the annual exceedance probability target introduced in Chapter 3 (i.e., p_e = 1e-3, 2e-3 or 3e-3).

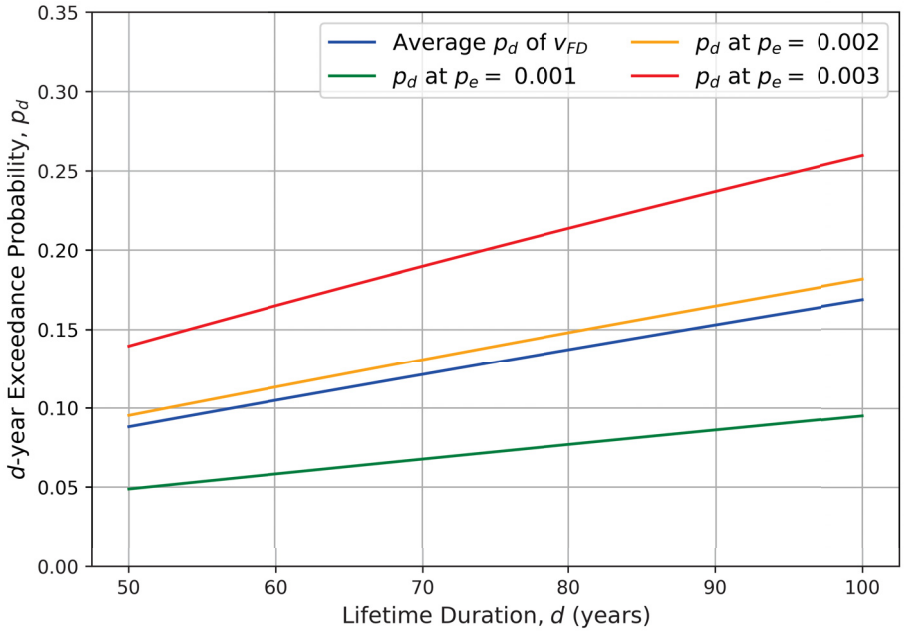

Figure 5.6: Average probability that the current factored design wind speed, v_{FD}, is exceeded over 14 Canadian cities during a d-year lifetime, where $50 \leq d \leq 100$.

Figure 5.6 demonstrates that under current (stationary) climate conditions the average d-year exceedance probability (blue line) remains slightly below the mid-level target for any design lifetime. Additionally, Fig. 5.6 shows that the difference between the minimum and maximum d-year exceedance probability targets increases as the design lifetime, d, increases. For example, the difference between p_d at $p_e = 0.001$ and that at $p_e = 0.003$ is 0.090 (0.139 - 0.049) at $d = 50$ years, and is 0.165 (0.260 - 0.095) at $d = 100$ years.

The current exceedance probabilities, which are based on a 50-year design lifetime, are deemed acceptable by society, even though it is known that the real lifetime of a structure is much longer than the 50-year design life. Therefore, although the average lifetime exceedance probability of v_{FD} increases from 0.088 at $d = 50$ years to 0.168 at $d = 100$ years (see Fig. 5.6), $p_{100} = 0.168$ is still assumed to be considered acceptable. It follows that the longer lifetime exceedance probability targets (i.e., the green, orange and red lines in Fig. 5.6) can also be considered acceptable.

Figures 5.7 and 5.8 show the 75- and 100-year lifetime exceedance probabilities under climate change for the HURP design wind speeds (proposed in Section 4.3.2), compared to the 75- and 100-year exceedance probability targets, respectively. The

75- and 100-year exceedance probability targets are as shown in Fig. 5.6 at $d = 75$ and $d = 100$ years, respectively. Figure 5.7 shows the average 75-year exceedance probability, p_{75}, over 14 Canadian cities under climate change cases (a) 1 and (b) 2, using the design wind speeds proposed in Figs. 4.11(a) and (b), respectively. Both climate change cases are evaluated over the model uncertainty range $1.0 \leq u_{CC} \leq 2.25$. The 75-year exceedance probability targets are shown as the green, orange and red lines, while the purple lines show p_{75} under climate change if the current design wind speeds continue to be used in the future. The black lines show the average p_{75} of v_{FD} under current conditions (i.e., the blue line in Fig. 5.6 evaluated at $d = 75$ years).

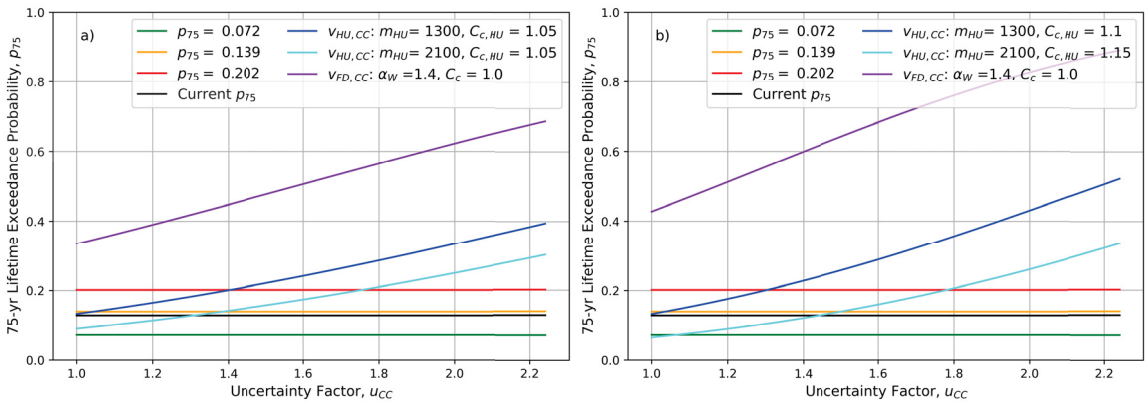

Figure 5.7: Average 75-year exceedance probability of $v_{HU,CC}$ over 14 Canadian cities for the HURP method, where the uncertainty factor, u_{CC}, ranges from 1.0 to 2.25 under climate change (a) case 1 and (b) case 2.

Figure 5.8 shows similar results to Fig. 5.7, except that the results are evaluated over an 100-year lifetime, instead a 75-year lifetime. The 100-year exceedance probability is denoted as p_{100}.

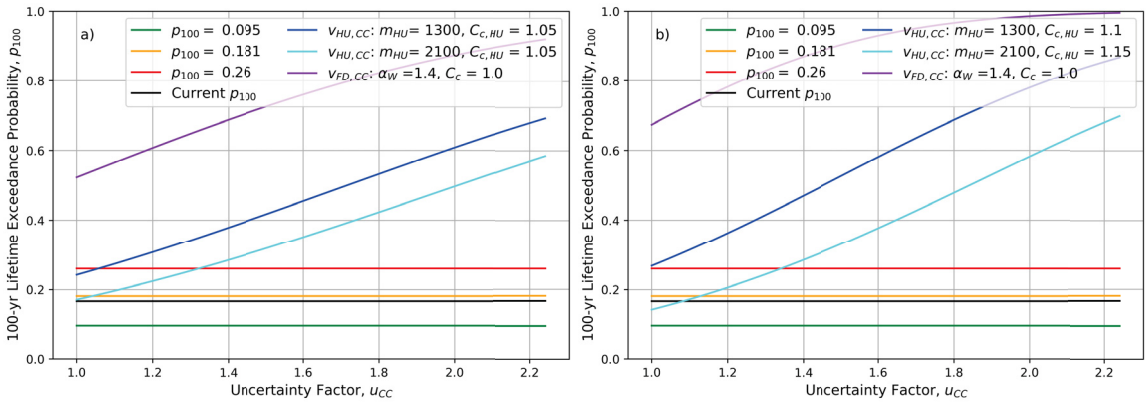

Figure 5.8: Average 100-year exceedance probability of $v_{HU,CC}$ over 14 Canadian cities for the HURP method, where the uncertainty factor, u_{CC}, ranges from 1.0 to 2.25 under climate change (a) case 1 and (b) case 2.

Figures 5.7 and 5.8 demonstrate that if the current factored design speeds continue to be used under climate change, the lifetime exceedance probabilities will far surpass the maximum targets at a 75-year lifetime, and will continue to increase further if the structure remains in service. Even under climate change case 1 with 50% model uncertainty p_{75} for v_{FD} (purple line) is 0.477, which is 136% greater than the maximum p_{75} target (i.e., 0.202).

Figures 5.7 and 5.8 also demonstrate that although the HURP design wind speed exceedance probabilities are lower than those of the current v_{FD} values, there is still reason to be concerned about the structural integrity of buildings, designed using the HURP method parameters, that remain in service longer than 50 years under climate change. Using the HURP design parameters recommended for climate change case 1 with 125% uncertainty (i.e., $m_{HU} = 2100$ years and $C_{c,HU} = 1.07$), the maximum p_{75} target will be exceeded when the model uncertainty is 88% under case 1. Meanwhile, if the HURP design parameters recommended for climate change case 1 with 50% uncertainty (i.e., $m_{HU} = 1300$ years and $C_{c,HU} = 1.04$) are used, the maximum p_{75} target will be exceeded when the model uncertainty is only 35% under case 1. Recall that the recommended HURP design parameters were selected to achieve the mid-level exceedance probability target over a 50-year design life. The above results demonstrate that under climate change case 1 structures will not meet exceedance probability targets at a 75-year lifetime, and under climate change case 2 the 75-year exceedance probabilities are even greater than those under case 1. Therefore, Figs. 5.7

and 5.8 suggest that under climate change a design lifetime larger than 50 years should be used to ensure reasonable exceedance probability levels are maintained over the entire real lifetime of structures.

Figures 5.9, 5.10 and 5.11 show the HURP design parameters required to achieve the minimum, mid-level and maximum d-year lifetime exceedance probability targets for the design lifetime range $50 \leq d \leq 100$. Figure 5.9 shows the average hybrid ultimate return periods, m_{HU}, over the 14 Canadian cities in Table 3.1. Figures 5.9(a) and (b) show the results for both climate change cases 1 and 2 (since both cases project the same increase in $\sigma_{V_{A1}}$), assuming 50% and 125% model uncertainty, respectively.

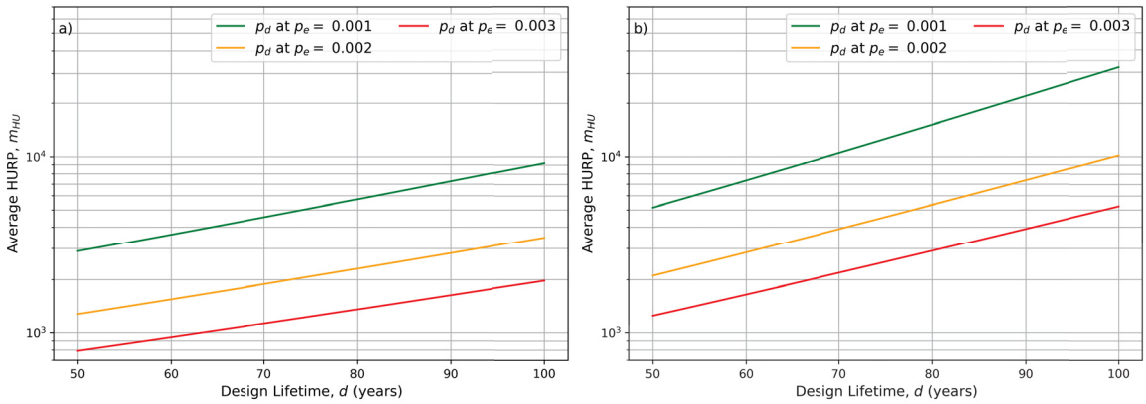

Figure 5.9: Average hybrid ultimate return period, m_{HU}, over 14 Canadian cities required to achieve target d-year exceedance probability p_d under climate change cases 1 and 2 ($\Delta_\sigma = 0.004 u_{CC}$) for $50 \leq d \leq 100$, assuming u_{CC} = (a) 1.5 and (b) 2.25.

Figure 5.9 demonstrates that the hybrid ultimate return period, m_{HU}, required to achieve a given exceedance probability level (i.e., p_d at p_e = 0.001, 0.002 or 0.003) increases exponentially with design lifetime (note that the y-axis scale is logarithmic in Fig. 5.9). Consequently, the difference between m_{HU} at the various target exceedance probability levels increases as the design lifetime increases (e.g., the difference between m_{HU} along the green line and m_{HU} along the orange line increases as d increases). Note that a consequence of increased design lifetime is that m_{HU} increases as shown in Fig. 5.9, and therefore, the uncertainty in estimations of $v_{A1,m_{HU}}$ increases. Recall that there is greater uncertainty in higher return period wind speeds due to lack of historical records and sampling error (see Section 4.3)

Figures 5.10(a) and (b) show the average hybrid climate change effect factor,

$C_{c,HU}$, over the 14 Canadian cities in Table 3.1 for climate change case 1, assuming 50% and 125% model uncertainty, respectively.

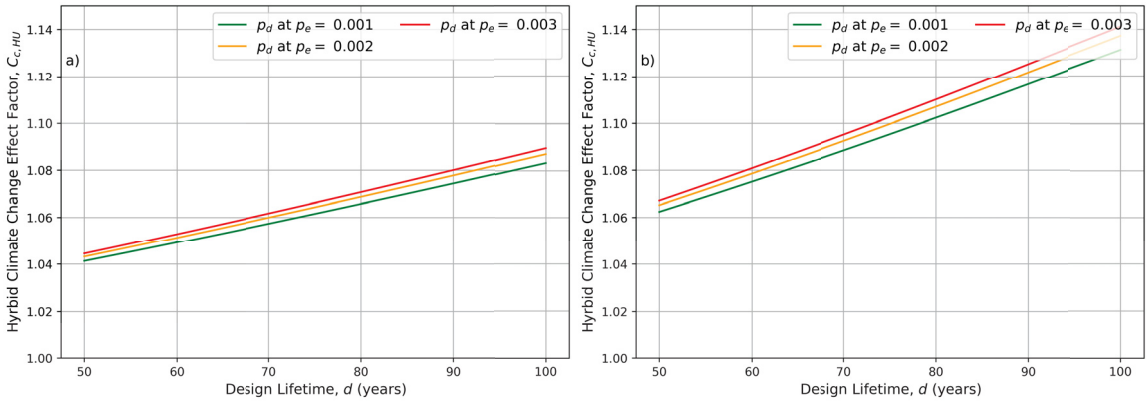

Figure 5.10: Average hybrid climate change effect factor, $C_{c,HU}$, over 14 Canadian cities required to achieve target d-year exceedance probability p_d under climate change case 1 ($\Delta_\mu = 0.0008 u_{CC}$) for $50 \leq d \leq 100$, assuming u_{CC} = (a) 1.5 and (b) 2.25.

Similarly, Figs. 5.10(a) and (b) show the average hybrid climate change effect factor, $C_{c,HU}$, over the 14 Canadian cities in Table 3.1 for climate change case 2, assuming 50% and 125% model uncertainty, respectively.

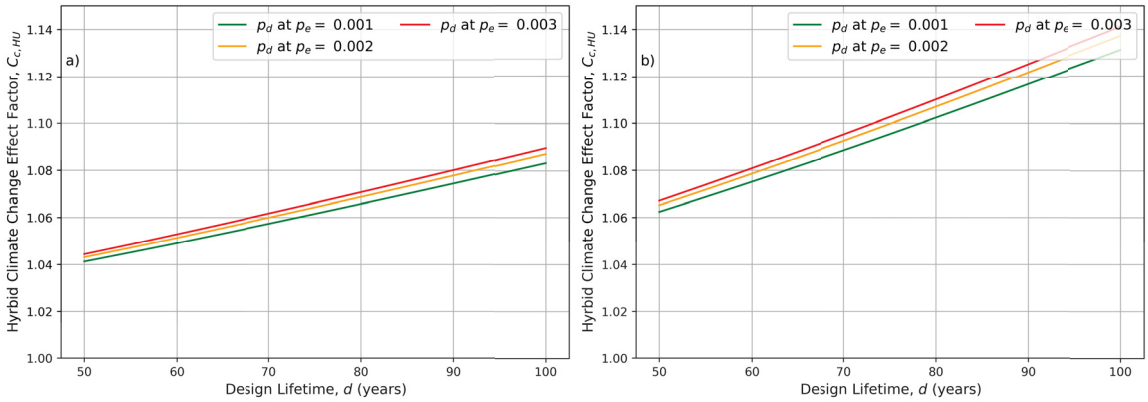

Figure 5.11: Average hybrid climate change effect factor, $C_{c,HU}$, over 14 Canadian cities required to achieve target d-year exceedance probability p_d under climate change case 2 ($\Delta_\mu = 0.0016 u_{CC}$) for $50 \leq d \leq 100$, assuming u_{CC} = (a) 1.5 and (b) 2.25.

Figures 5.10 and 5.11 demonstrate that the hybrid climate change effect factor, $C_{c,HU}$, increases linearly with design lifetime. Additionally, Figs. 5.10 and 5.11 demonstrate that the magnitude that $C_{c,HU}$ must be increased by to maintain a given exceedance probability level from d = 50 years to d = 100 years is larger for climate change

case 2 relative to case 1, and for 125% uncertainty relative to 50% uncertainty. To achieve the mid-level d-year exceedance probability target, $C_{c,HU}$ increases by 0.044 and 0.0719 from $d = 50$ years to $d = 100$ years under climate change case 1, assuming 50% and 125% model uncertainty, respectively. Under climate change case 2 $C_{c,HU}$ increases by 0.104 and 0.177 from $d = 50$ years to $d = 100$ years for the mid-level target, assuming 50% and 125% model uncertainty, respectively. Figures 5.10 and 5.11 also demonstrate that the values of $C_{c,HU}$ at each exceedance probability level are approximately equal under each of the four climate change scenarios. The maximum difference occurs between p_{100} at $p_e = 0.001$ and p_{100} at $p_e = 0.003$ under climate change case 2 with 125% model uncertainty (i.e., green and red lines in Fig. 5.11 at $d = 100$ years). At this point the difference in $C_{c,HU}$ is 0.023, which can be considered negligible given that the values of $C_{c,HU}$ are rounded to the nearest half tenth for simplicity.

The HURP design wind speeds for design lifetimes in the range $50 \leq d \leq 100$ were then determined using the HURP design parameters in Figs. 5.9, 5.10 and 5.11. Figure 5.12 shows the average HURP design wind speed, $v_{HU,CC}$, over the same 14 Canadian cities required to meet the minimum, mid-level and maximum exceedance probability target for $50 \leq d \leq 100$ under climate change case 1, assuming (a) 50% model uncertainty and (b) 125% model uncertainty.

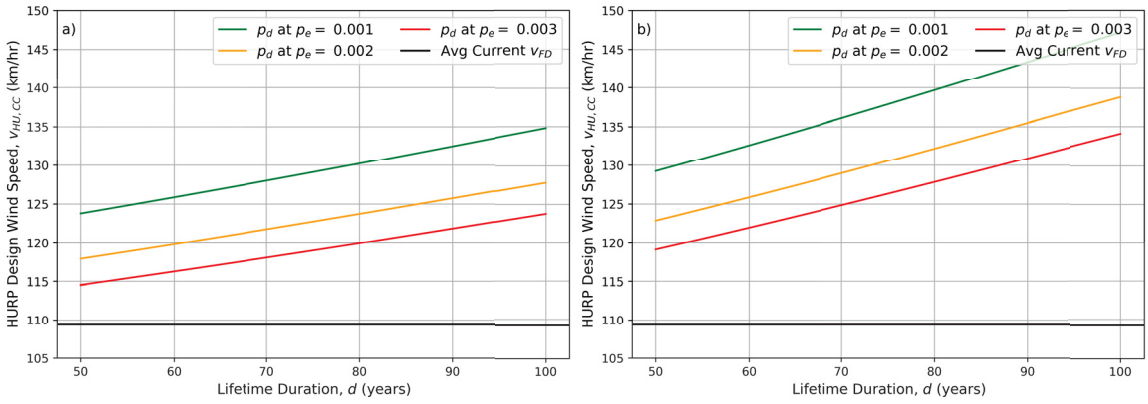

Figure 5.12: Average future HURP design wind speed, $v_{HU,CC}$, over 14 Canadian cities required to achieve target d-year exceedance probability p_d under climate change case 1 ($\Delta_\mu = 0.0008 u_{CC}$) for $50 \leq d \leq 100$, assuming u_{CC} = (a) 1.5 and (b) 2.25.

Figure 5.13 shows similar results to Fig. 5.12 but for climate change case 2, instead of case 1.

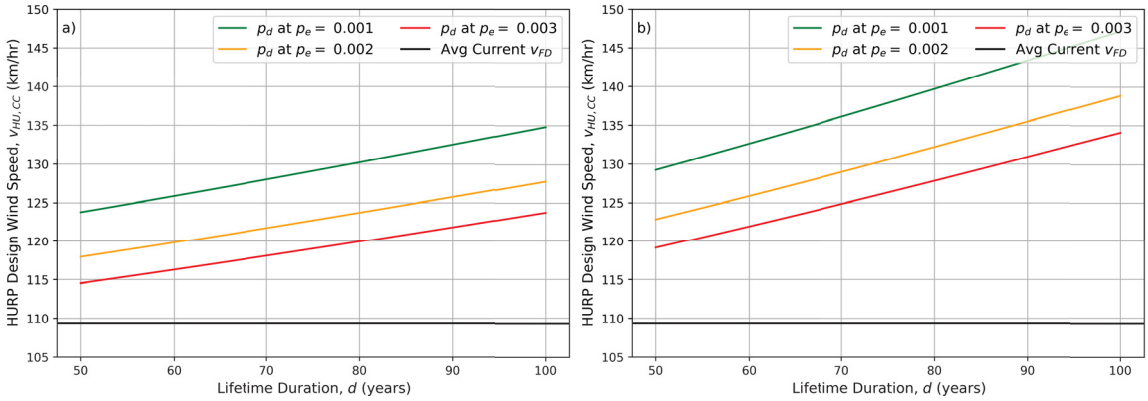

Figure 5.13: Average future HURP design wind speed, $v_{HU,CC}$, over 14 Canadian cities required to achieve target d-year exceedance probability p_d under climate change case 2 ($\Delta_\mu = 0.0016 u_{CC}$) for $50 \leq d \leq 100$, assuming u_{CC} = (a) 1.5 and (b) 2.25.

Figure 5.12 shows that to achieve the mid-level exceedance probability target, on average, $v_{HU,CC}$ will increase 10 km h^{-1}, from 118 km h^{-1} at $d = 50$ years to 128 km h^{-1} at $d = 100$ years under climate change case 1, assuming 50% uncertainty. Under climate change case 1 assuming 125% model uncertainty, on average, $v_{HU,CC}$ will increase 16 km h^{-1}, from 122 km h^{-1} at $d = 50$ years to 138 km h^{-1} at $d = 100$ years to achieve this same mid-level exceedance target. Similarly, Fig. 5.13 shows that for the mid-level target under climate change case 2 assuming 50% uncertainty the average increase in $v_{HU,CC}$ from $d = 50$ to 100 years is 13 km h^{-1}, from 120 km h^{-1} to 133 km h^{-1}, while, assuming 125% uncertainty the average increase in $v_{HU,CC}$ from $d = 50$ to 100 years is 22 km h^{-1}, from 127 km h^{-1} to 149 km h^{-1}. Both Figs. 5.12 and 5.13 demonstrate that the HURP design wind speed increases linearly with design lifetime (i.e., the difference between the green, orange and red lines is relatively constant from $d = 50$ years to $d = 100$ years). Under the most extreme scenario considered in this thesis (i.e., climate change case 2 with 125% model uncertainty) the difference between the average value of $v_{HU,CC}$ at the maximum and minimum target exceedance probability is 10 km h^{-1} at $d = 50$ years and 13 km h^{-1} at $d = 100$ years.

5.4 Design Recommendations

Under climate change, it is recommended that the Hybrid Ultimate Return Period wind loading design method be adopted in the NBCC, as well as other structural

design codes where applicable. As discussed in Section 5.1, the HURP method is the best overall wind loading design method under climate change compared to the LRFD and AURP methods. While all three methods meet the exceedance probability targets on average, the HURP method results in the most consistent exceedance probabilities across the 14 Canadian stations studied in this thesis. Recall from Section 5.1 that under current, stationary conditions the LRFD method exceedance probability variability, due to the range of $\mathrm{CV}_{v_{A1}}$ values, is greater than that of the ultimate return period method, due to sample size effect, for return periods ranging from 500 to 700 years (Hong et al., 2016), and that it is assumed that the aforementioned results still hold under climate change. An additional benefit of the HURP method compared to the AURP method is that there is less uncertainty in estimates of $v_{A1,m_{HU}}$ than in estimates of $v_{A1,m_{AU}}$. Recall that there is greater uncertainty in higher return period wind speeds due to lack of historical records and sampling error, and that m_{AU} is much larger than m_{HU} since m_{HU} only accounts for increases in $\sigma_{V_{A1}}$. The HURP method design parameters, m_{HU} and $C_{c,HU}$, are also simpler to modify when climate change projections change in the future as human behaviour evolves and climate change models improve. Structural engineers simply need to select the value of $C_{c,HU}$ based on the projected relative increase in $\mu_{V_{A1}}$, and select the value of m_{HU} based on the projected relative increase in $\sigma_{V_{A1}}$.

The recommended HURP wind loading design parameters, $C_{c,HU}$ and m_{HU}, are presented in Tables 5.1, 5.2 and 5.3 for 50, 75 and 100-year design lifetimes, respectively. The design parameters are evaluated at the minimum, mid-level and maximum exceedance probability targets used in this thesis under the four climate change scenarios (i.e., climate change cases 1 and 2 with both 50% and 125% model uncertainty). Recall that the objective of this thesis was to develop a wind loading design method to be used under climate change that achieves consistent exceedance probabilities across Canada, and not to determine the design lifetime, the target exceedance probability, nor the projected change in the distribution of V_{A1}. Therefore, the recommended design parameters are presented for a reasonable range of possible values, determined based on the literature, for the design lifetime, the target exceedance probability, and the increase in the annual maximum wind speed distribution.

Table 5.1: Fifty year lifetime HURP method design parameters for minimum, mid-level, and maximum exceedance probability targets.

Scenario	Parameter	Minimum	Mid-Level	Maximum
C1, $u_{CC} = 1.5$	$C_{c,HU}$	1.04	1.04	1.04
	m_{HU}	2900	1300	800
C1, $u_{CC} = 2.25$	$C_{c,HU}$	1.06	1.07	1.07
	m_{HU}	5200	2100	1200
C2, $u_{CC} = 1.5$	$C_{c,HU}$	1.08	1.09	1.09
	m_{HU}	2900	1300	800
C2, $u_{CC} = 2.25$	$C_{c,HU}$	1.13	1.14	1.14
	m_{HU}	5200	2100	1200

Table 5.2: Seventy-five year lifetime HURP method design parameters for minimum, mid-level, and maximum exceedance probability targets.

Scenario	Parameter	Minimum	Mid-Level	Maximum
C1, $u_{CC} = 1.5$	$C_{c,HU}$	1.06	1.06	1.07
	m_{HU}	5100	2100	1200
C1, $u_{CC} = 2.25$	$C_{c,HU}$	1.1	1.1	1.1
	m_{HU}	12600	4600	2500
C2, $u_{CC} = 1.5$	$C_{c,HU}$	1.13	1.14	1.14
	m_{HU}	5100	2100	1200
C2, $u_{CC} = 2.25$	$C_{c,HU}$	1.21	1.22	1.23
	m_{HU}	12600	4600	2500

Updated gust effect factor values, C_g, are not presented in this thesis due to lack of data available for analysis. However, it is highly recommended that further research be completed on this topic because the preliminary results in Section 1.3.4 demonstrated that the current NBCC gust effect factor recommended for the main strucutural members of large buildings (i.e., $C_g = 2.0$) may be underestimated even under the current, stationary climate conditions, and Sections 1.4.3 and 3.3.1 showed that under climate change C_g may need to be increased even further. Section 1.3.4 showed that the value of CV_V, estimated based on the "Durst Curve" (i.e., 0.16) is much lower than the empirical CV_V values estimated based on the NAV CANADA - TO2015 and EC HLY01 datasets (i.e., 0.64 and 0.69, respectively), and that these increased values of CV_V lead to a significantly larger C_g. For example, assuming $\text{CV}_V = 0.64$, the three second gust effect factor is 3.9 (i.e., $C_g = G(w = 3 \text{ sec}, W = 1 \text{ hr})^2 = 1.98^2$), which is almost double the current value of C_g in the NBCC. However, the analytical result (3.98) is for the peak gust speed, while the NBCC C_g value (2.0)

Table 5.3: One hundred year lifetime HURP method design parameters for minimum, mid-level, and maximum exceedance probability targets.

Scenario	Parameter	Minimum	Mid-Level	Maximum
C1, $u_{CC} = 1.5$	$C_{c,HU}$	1.08	1.09	1.09
	m_{HU}	9200	3500	2000
C1, $u_{CC} = 2.25$	$C_{c,HU}$	1.13	1.14	1.14
	m_{HU}	32000	10200	5200
C2, $u_{CC} = 1.5$	$C_{c,HU}$	1.18	1.19	1.2
	m_{HU}	9200	3500	2000
C2, $u_{CC} = 2.25$	$C_{c,HU}$	1.3	1.32	1.32
	m_{HU}	32000	10200	5200

is purposefully selected to be somewhat lower since wind gusts are not well correlated over large buildings, resulting in the effects of individual gusts on large buildings being less significant (NRCC, 2015). It is not clear how the C_g values in the NBCC were determined, consequently, it is unknown if C_g needs to be updated. It should also be noted that for the preliminary analysis of C_g in Section 1.3.4, the empirical CV_V values were estimated using the variance reduction function, $\gamma(T)$, which was determined using only three months of two min average wind speed measurements recorded at four southern Ontario stations (i.e., the NAV CANADA - TO2015 dataset). Therefore, analysis of a much larger dataset is also required to justify increasing C_g. Further research on C_g under climate change is also important because current climate change models suggest that CV_V will increase in the future, which would lead to increases in C_g.

Chapter 6

Conclusions

In this thesis, structural design wind loading requirements were investigated to determine future design wind loads that will (a) account for the projected changes in wind speeds due to climate change and (b) improve exceedance probability consistency across Canada. In Chapter 1, the traditional statistical modelling methods used to determine current wind design requirements were modified so that the wind speed distributions were non-stationary, since both the mean and variance of wind speeds are expected to increase in the future due to climate change. Common methods in the literature were used to develop a non-stationary extreme value model for the annual maximum one-hourly average wind speed in year y, $F_{v_{A1}}(v; y)$, and to investigate the effects of non-stationarity on return period. In this thesis $F_{v_{A1}}(v; y)$ is a non-stationary Gumbel distribution where the mean and standard deviation increase linearly with year y. The effects of non-stationarity on two interpretations of return period, (1) the expected time to the next exceedance event (m_1) and (2) the number of years with one expected exceedance event (m_2), were then assessed. The results showed that both m_1 and m_2 are reduced rapidly when the annual rate of change in the mean or standard deviation of V_{A1} increases. However, a relatively small increase in the design wind speeds results in the return period being maintained at 50 years under climate change (for both definitions, m_1 and m_2). It was also determined that m_2 is a more appropriate definition of return period under climate change because, while m_1 is more conservative, m_2 is more logical in the context of structural design. That is, it is more important to ensure structures can withstand all expected loads over the design lifetime than to consider the year of occurrence of an exceedance event. By evaluating the 50-year lifetime exceedance probability, p_{50}, it was also shown that m_1 results in slight over design relative to the current p_{50}, while m_2 approximately maintains the current p_{50}.

A study of the effects of wind speed averaging duration on the wind speed distribution, and consequently, the gust effect factor, C_g, and the m-year return period annual maximum W-average wind speed, $v_{AW,m}$, was also completed in Chapter 1. The wind speed variance reduction function, $\gamma(T)$, was determined by fitting wind speed measurements with averaging durations of two min to two hours to the fractional Gaussian noise variance reduction function. The results of this study showed that averaging duration does not have a large effect on $v_{AW,m}$. An analytical solution to the gust factor, $G(w, W)$, originally defined by Durst (1960), was also developed (recall that w and W are the short and longer term averaging durations, respectively). The analytical solution demonstrated that $G(w, W)$ can be solved based only on the parameters $g(w, W)$, CV_V, and $\gamma(T)$. The analytical gust factor, $G(w, W)$, was evaluated for short-term averaging durations ranging from 1 to 3000 seconds when W = 1 hr, and where the instantaneous wind speed coefficient of variation, CV_V, was determined empirically. The results showed that the current gust effect factor used in the NBCC for main strucutural members (i.e., $C_g = 2.0$) may be underestimated under the current, stationary climate conditions, since the analytical gust factor curve resulted in $C_g = 3.98$ at $w = 3$ sec (note that $C_g = G^2$). However, the analytical result (3.98) is for the peak gust speed, while the NBCC C_g value (2.0) is intended for large buildings, which are less affected by individual gusts since wind gusts are not well correlated over large buildings (NRCC, 2015). It is not clear how the NBCC determined C_g values; therefore, it is unknown if C_g needs to be updated. Additionally, the empirical CV_V values used to determine $G(w, W)$ were estimated using only three months of 2 min average wind speed measurements recorded at four southern Ontario stations (i.e., the NAV CANADA - TO2015 dataset). Therefore, an analysis of a much larger dataset should be completed before C_g is increased. The effect of non-stationarity on the gust factor was also assessed, assuming that climate change will cause the instantaneous wind speed mean and standard deviation to increase, and that $\gamma(T)$ will not significantly change under climate change. It was found that if μ_V and σ_V increase at the same rate (i.e., $\Delta_\mu = \Delta_\sigma = \Delta$) C_g will not change in the future, while if $\Delta_\mu < \Delta_\sigma$ C_g will increase and if $\Delta_\mu > \Delta_\sigma$ C_g will decrease.

Chapter 2 provides a literature review of Canadian extreme wind speed projections, estimated using state-of-the-art climate change models. Based on the results of

these studies, it was concluded that the annual maximum wind speed mean is likely to increase 4% over the next 50 years across most regions of Canada, although, in some locations the mean may increase up to 8%. The maximum change, across all regions, in the annual maximum wind speed standard deviation is estimated to be 20% over the next 50 years. In addition, the results suggested that the gust factor, G, is expected to increase 12% over the same time period across most regions of Canada, and up to 20% for some regions of the west coast. The sources of uncertainty in these climate models include the emissions scenario realized in the future, the model formulation and the internal (or natural) variability in the Earth's climate. While studies that aim to quantify the magnitude of these sources of uncertainty are limited, it was concluded that the emissions scenario uncertainty is approximately 15-50% and the model formulation uncertainty is approximately 30-75%. Internal variability is assumed to be accounted for in the model projections because the studies used in this thesis are based on 30 years of simulated data, which is considered sufficient when accounting for sampling uncertainty. The total uncertainty in the projected changes in wind speed distributions is then between 45% and 125%. In this thesis, total uncertainty was assumed to lie between 50 and 125%.

In Chapter 3, the current structural LRFD methods used in Canada for buildings under wind loading were assessed and updated such that the current wind load exceedance probabilities are maintained under climate change. Specifically, updated values of α_W and $\hat{F}_W$ were determined such the probability that the factored design wind load, $\alpha_W \hat{F}_W$, is exceeded over the design life of the structure remains constant in the future. The LRFD method to be used under climate change, proposed herein, requires increasing α_W such that α_W accounts for all current sources of uncertainty, as well as the increased variability in the annual maximum one-hourly average wind pressure, q_{A1}, due to climate change. Additionally, $\hat{F}_W$ is increased in this LRFD method by adding a climate change effect factor, C_c (proposed herein), which accounts for the projected increase in the mean of q_{A1} due to climate change. Design parameters to be used under climate change (i.e., α_W and C_c), and the resulting design wind speeds were proposed for 14 Canadian locations under four climate change scenarios. The 50-year exceedance probabilities of these design wind speeds are then evaluated under a range of climate change scenarios. The results showed that under

the most extreme climate change case assessed in this thesis (i.e., climate change case 2 with 125% uncertainty), the average design wind speed would need to increase $19\,\mathrm{km\,h^{-1}}$ to maintain the current 50-year lifetime exceedance probabilities, while under the least extreme climate change case assessed in this thesis (i.e., climate change case 1 with 50% uncertainty), the average design wind speed would need to increase $8.6\,\mathrm{km\,h^{-1}}$ to maintain the current 50-year lifetime exceedance probabilities.

Further analysis of the effect of climate change on the gust effect factor was also completed in Chapter 3. The non-stationary gust factor, G_y, was evaluated in terms of the total relative increase in CV_V over y years, η_{CV}, for $0 \leq \eta_{\mathrm{CV}} \leq 1$. The increase in CV_V corresponding to the projected increases in G due to climate change estimated by Jeong and Sushama (2019) was then determined. Assuming 125% model uncertainty in Jeong and Sushama's (2019) estimates, G will increase 27% across most regions of Canada by 2071-2100, while on the west coast G will increase up to 45%. It was found that CV_V increases 58% when G increases 27%, and that CV_V increases 97% when G increases 45%. These expected increases in the instantaneous wind speed coefficient of variation were found to be much greater than the expected increase in $\mathrm{CV}_{v_{A1}}$ (i.e., 36%, assuming 125% model uncertainty), however, there is no physical reason for CV_V and $\mathrm{CV}_{v_{A1}}$ to be equal.

Chapter 4 assessed the ultimate return period method, an alternative wind loading design method used in the ASCE-7, in which the factored design wind speed is defined as the product of a wind load factor of 1.0 and a much longer return period annual maximum wind speed, v_{A1,m_U}. Under current climate conditions the ultimate return period has been shown to achieve improved exceedance probability consistency across Canada (Hong et al., 2016). The current ultimate return period design wind speeds were evaluated at three annual exceedance probability targets: p_e = 1e-3, 2e-3 and 3e-3 (which correspond to ultimate return periods of 1000, 500 and 333 years, respectively). The results showed that the current factored design wind speed is closest to the 500-year return period design wind speed at most of the 14 locations that were assessed. Therefore, adopting the ultimate return period method under current climate conditions with m_U = 500 years will result in minimal changes to the design wind speed at most locations, but will greatly improve exceedance probability consistency across Canada such that the annual exceedance probability is 2e-3 at all locations.

Two alternative ultimate return period methods were then proposed, which account for the projected changes in the distribution of V_{A1} under climate change. Similar to the LRFD method proposed in Chapter 3, the climate change ultimate return period design parameters were selected such that the 50-year exceedance probability, p_{50}, is approximately equal to a target 50-year exceedance probability under a given climate change scenario. The first method was named the "All-Inclusive Ultimate Return Period" (AURP) method. The AURP design wind speed under climate change is defined as $v_{AU,CC} = v_{A1,m_{AU}}$, where m_{AU} is the"all-inclusive ultimate return period". The method was named "all-inclusive" to refer to the fact that m_{AU} is an updated value of m_U that accounts for increases in both the mean and standard deviation of V_{A1} due to climate change.

The second method was named the "Hybrid Ultimate Return Period" (HURP) method because the HURP method combines the ultimate return period and the climate change effect factor, the latter of which was proposed in the LRFD method in Chapter 3. In the HURP method the "hybrid ultimate return period", m_{HU}, accounts for increases in the standard deviation of q_{A1} due to climate change, while the HURP method climate change effect factor, $C_{c,HU}$, accounts for the projected increases in the mean of q_{A1} due to climate change. Design parameters for both the AURP and HURP method were proposed for the same four climate change scenarios assessed in Chapter 3. The resulting design wind speeds and 50-year exceedance probabilities were then presented. As expected the values of m_{AU} were much greater than m_{HU}, since m_{HU} only accounts for changes in the standard deviation of V_{A1}, and does not account for changes in the mean as well. The results also showed that, on average, the design wind speeds and 50-year exceedance proabilities of the two methods were similar, however, there appeared to be more variability in p_{50} between locations for the AURP method compared to HURP method.

Finally, in Chapter 5, the effects of the target exceedance probability and design lifetime on the HURP method design parameters and wind speeds were investigated, since the HURP method was determined to be the best overall wind loading design method. The three proposed climate change wind loading design methods were compared by assessing which method best achieved the objectives of this thesis, that is, to develop a future wind loading design methodology that (a) maintains the current

50-year lifetime exceedance probabilities under climate change, and (b) improves the 50-year exceedance probability consistency across Canada. It was shown that on average all three methods maintain the current average exceedance probability, but that the HURP method led to the most consistent exceedance probabilities across the 14 locations assessed in this thesis. Additional benefits of the HURP method were also discussed including that there is less uncertainty in estimates of the HURP design wind speeds than in estimates of the AURP design wind speeds, and that the HURP method is the easiest method for structural engineers to modify as climate change projections evolve in the future. Therefore, the HURP method is considered the best overall wind loading design method to be used under climate change out of the three methods proposed in this thesis. Note that under current, stationary conditions the LRFD method exceedance probability variability, due to the range of $\mathrm{CV}_{v_{A1}}$ values, is greater than that of the ultimate return period method, due to sample size effect, for return periods ranging from 500 to 700 years (Hong et al., 2016). This study does not further investigate the uncertainty in the HURP method design wind speeds due to large return period values, m_{HU}, but it is assumed that the aforementioned results from Hong et al. (2016) still hold under climate change.

The sensitivity of the HURP design parameters to the target exceedance probability was also evaluated, and it was shown that m_{HU} increases as the target exceedance probability decreases, while $C_{c,HU}$ remains approximately constant. Consequently, the HURP design wind speed increases moderately as the target exceedance probability decreases. Under all four climate change cases assessed in this thesis, the average design wind speed increased by approximately $10\,\mathrm{km\,h^{-1}}$ when the 50-year exceedance probability target is increased from 0.139 to 0.049. The effects of design lifetime on the HURP method design wind speeds and exceedance probabilities were then investigated because in practice the real lifetime of a well-maintained structure is significantly larger than the design working life defined by structural codes (which is 50 years in the NBCC). Under current, stationary climate conditions the lifetime exceedance probability increases from 0.088 at 50 years to 0.168 at 100 years; it is assumed that this increase is deemed acceptable by society. The results showed that the proposed HURP method design wind speeds will not meet the target exceedance probabilities (i.e., the currently accepted exceedance levels) under climate change

even at a 75-year design lifetime. Therefore, design parameters should be selected for a larger design lifetime, more representative of the real lifetime of a structure to ensure its structural integrity. The HURP method design parameters, and corresponding wind speeds required to achieve the minimum, mid-level and maximum exceedance probability targets for design lifetimes ranging from 50 to 100 years were presented for the four climate change scenarios. The required increases in the design wind speeds were relatively moderate. For example, the average design wind speed increased $22\,\mathrm{km\,h^{-1}}$ from 50 to 100 year under climate change case 2 with 125% model uncertainty.

6.1 Recommendations for Future Work

For the HURP method, future research is recommended in the following areas:

- Expansion of the study of the HURP method performed in Chapter 4 across more locations in Canada
- Comparison of the variability in the lifetime exceedance probabilities between the LRFD method and the HURP method under climate change, where the additional uncertainty in estimates of $v_{A1,m_{HU}}$ due to the large return period, m_{HU}, is considered

Further research on the gust effect factor is recommended in the following areas:

- Review of how C_g was determined in the current NBCC, and validation of the current C_g by repeating the analysis performed in Section 1.3.4 using a dataset of 1 sec wind speed measurements recorded at several locations across Canada, over a time period which sufficiently accounts for seasonal changes
- Comprehensive study of C_g under climate change which considers peak gust lifetime exceedance probabilities, accounting for projected changes in CV_V and in the frequency of wind gust events under climate change

References

Allen, D. E. (1992), 'Canadian highway bridge evaluation: reliability index', *Canadian Journal of Civil Engineering* **19**, 987–991.

Allen, M. R., Dube, O. P., Solecki, W., Aragón-Durand, F., Cramer, W., Humphreys, S., Kainuma, M., Kala, J., Mahowald, N., Mulugetta, Y., Perez, R., Wairiu, M. and Zickfeld, K. (2018), *An IPCC special report on the impacts of global warming of 1.5 °C above pre-industrial levels and related global greenhouse gas emission pathways, in the context of strengthening the global response to the threat of climate change, sustainable development, and efforts to eradicate poverty*, in , chapter Framing and Context.

Asch, R., Pilcher, D., Rivero-Calle, S. and Holding, J. (2016), 'Demystifying models: Answers to ten common questions that ecologists have about earth system models', *Limnology and Oceanography Bulletin* **25**.

Bartlett, F. M., Hong, H. P. and Zhou, W. (2003*a*), 'Load factor calibration for the proposed 2005 edition of the national building code of canada: Companion-action load combinations', *Canadian Journal of Civil Engineering* **30**(2), 440–448.

Bartlett, F. M., Hong, H. P. and Zhou, W. (2003*b*), 'Load factor calibration for the proposed 2005 edition of the national building code of canada: Statistics of loads and load effects', *Canadian Journal of Civil Engineering* **30**(2), 429–439.

Cheng, L., AghaKouchak, A., Gilleland, E. and Katz, R. W. (2014), 'Non-stationary extreme value analysis in a changing climate', *Climatic change* **127**(2), 353–369.

Cheng, S. C., Lopes, E., Fu, C. and Huang, Z. (2014), 'Possible impacts of climate change on wind gusts under downscaled future climate conditions: Updated for canada', *Journal of Climate* **27**(3), 1255–1270.

Cooley, D. (2013), *Return periods and return levels under climate change*, Springer Netherlands, Dordrecht, pp. 97–114.

Croce, P., Formichi, P. and Landi, F. (2019), 'Climate change: Impacts on climatic actions and structural reliability', *Applied Sciences* **9**(24), 5416.

Durst, C. (1960), 'Wind speeds over short periods of time', *Meteor. Mag* **89**(1056), 181–187.

Ellingwood, B. R. (1994), 'Probability-based codified design: past accomplishments and future challenges', *Structural Safety* **13**, 159–176.

Ellingwood, B. R., Galambos, T., MacGregor, J. and Cornell, C. (1980), *Development of a Probability Based Load Criterion for American National Standard A58*, Vol. 13, US Department of Commerce, National Bureau of Standards.

Faranda, D., Lucarini, V., Turchetti, G. and Vaienti, S. (2011), 'Numerical convergence of the block-maxima approach to the generalized extreme value distribution', *Journal of statistical physics* **145**(5), 1156–1180.

Feng, T., Fu, Z., Deng, X. and Mao, J. (2009), 'A brief description to different multi-fractal behaviors of daily wind speed records over china', *Physics Letters A* **373**(45), 4134–4141.

Fenton, G. A. (1999), 'Estimation for stochastic soil models', *Journal of Geotechnical and Geoenvironmental Engineering* **125**(6), 470–485.

Fenton, G. A., Naghibi, F., Dundas, D., Bathurst, R. J. and Griffiths, D. V. (2015), 'Reliability-based geotechnical design in 2014 canadian highway bridge design code', *Canadian Geotechnical Journal* **53**(2), 236–251.

Fenton, G. and Griffiths, D. V. (2008), 'Risk assessment in geotechnical engineering', *John wiley&Sons, Inc* pp. 381–400.

Fisher, R. A. and Tippett, L. H. C. (1928), Limiting forms of the frequency distribution of the largest or smallest member of a sample, *in* 'Mathematical Proceedings of the Cambridge Philosophical Society', Vol. 24, Cambridge University Press, pp. 180–190.

Flato, G., Marotzke, J., B., A., Braconnot, P., Chou, S. C., Collins, W., Cox, P., Driouech, F., Emori, S., Eyring, V., Forest, C., Gleckler, P., Guilyardi, E., Jakob, C., Kattsov, V., Reason, C. and Rummukainen, M. (2018), *An IPCC special report on the impacts of global warming of 1.5 °C above pre-industrial levels and related global greenhouse gas emission pathways, in the context of strengthening the global response to the threat of climate change, sustainable development, and efforts to eradicate poverty*, in , chapter Evaluation of Climate Models.

Friedman, J., Hastie, T. and Tibshirani, R. (2001), 'The elements of statistical learning', **1**(10).

Giblett, M. A. (1932), *The Structure of Wind over Level Country: Report on Experiments Carried Out at the Royal Airship Works, Cardington*, HM Stationery Office.

Gnedenko, B. (1943), 'Sur la distribution limite du terme maximum d'une serie aleatoire', *Annals of mathematics* pp. 423–453.

Goyette, S. (2008), 'Development of a model-based high-resolution extreme surface wind climatology for switzerland', *Nat Hazards* **44**, 329–339.

Harper, B., Kepert, J. and Ginger, J. (2010), *Guidelines for converting between various wind averaging periods in tropical cyclone conditions*, WMO, Geneva, Switzerland.

Hawkins, E. and Sutton, R. (2009), 'The potential to narrow uncertainty in regional climate predictions', *Bulletin of the American Meteorological Society* **90**(8), 1095–1108.

Hong, H. P., Mara, T., Morris, R., Li, S. and Ye, W. (2014*a*), 'Basis for recommending an update of wind velocity pressures in canadian design codes', *Canadian Journal of Civil Engineering* **41**(3), 206–221.

Hong, H. P., Ye, W. and Li, S. H. (2016), 'Sample size effect on the reliability and calibration of design wind load', *Structure and Infrastructure Engineering* **12**(6), 752–764.

Hong, H. P., Zu, G. G. and King, J. P. C. (2014*b*), 'Reliability consideration for fatigue design of sign, luminaire, and traffic signal support structures under wind load', *Journal of Wind Engineering and Industrial Aerodynamics* **126**, 60–74.

International Panel on Climate Change (IPCC) (2018), *An IPCC special report on the impacts of global warming of 1.5 °C above pre-industrial levels and related global greenhouse gas emission pathways, in the context of strengthening the global response to the threat of climate change, sustainable development, and efforts to eradicate poverty.*

Jeong, D. I. and Sushama, L. (2018), 'Projected changes to extreme wind and snow environmental loads for buildings and infrastructure across canada', *Sustainable Cities and Society* **36**, 225–236.

Jeong, D. I. and Sushama, L. (2019), 'Projected changes to mean and extreme surface wind speeds for north america based on regional climate model simulations', *Atmosphere* **10**, 497.

Kariyawasam, S. N. (1996), Development of probability based resistance factors and companion-action load factors for concrete design in Canada, PhD thesis, University of Alberta.

Katz, R. W. (2013), *Statistical Methods for Nonstationary Extremes*, Springer Netherlands, Dordrecht, pp. 15–37.

Krayer, W. R. and Marshall, R. D. (1992), 'Gust factors applied to hurricane winds', *Bulletin of the American Meteorological Society* **73**(5), 613–618.

Kumar, D., Mishra, V. and Ganguly, A. (2015), 'Evaluating wind extremes in cmip5 climate models', *Clim Dyn* **45**, 441–453.

Lombardo, F. and Ayyub, B. (2017), 'Approach to estimating near-surface extreme wind speeds with climate change considerations', *ASCE-ASME Journal of Risk and Uncertainty in Engineering Systems, Part A: Civil Engineering* **3**(3), A4017001.

Madsen, H. O., Krenk, S. and Lind, N. C. (2006), *Methods of structural safety*, Courier Corporation.

Mandelbrot, B. B. and Van Ness, J. W. (1968), 'Fractional brownian motions, fractional noises and applications', *SIAM review* **10**(4), 422–437.

Miller, C. A. (2011), 'Revisiting the durst gust factor curve', *Canadian Journal of Civil Engineering* **38**(9), 998–1001.

National Research Council of Canada (2015), *National Building Code of Canada*, 14 edn, National Research Council of Canada, Ottawa.

Nikulin, G., Kjellström, E., Hansson, U., Strandberg, G. and Ullerstig, A. (2011), 'Assessing the vulnerability of wind energy to climate change and extreme events', *Tellus A* **63**, 41–55.

Olsen, J. R., Lambert, J. H. and Haimes, Y. Y. (1998), 'Risk of extreme events under nonstationary conditions', *Risk Analysis* **18**(4), 497–510.

Pickands, J. et al. (1975), 'Statistical inference using extreme order statistics', *the Annals of Statistics* **3**(1), 119–131.

Pryor, S. C., Barthelmie, R., Clausen, N., Drew, M., MacKellar, N. and Kjellström, E. (2012*a*), 'Analyses of possible changes in intense and extreme wind speeds over northern europe under climate change scenarios', *Clim Dyn* **38**, 189–208.

Pryor, S. C., Barthelmie, R. and Schoof, J. (2012*b*), 'Past and future wind climates over the contiguous usa based on the north american regional climate change assessment program model suite', *Journal of Geophysical Research: Atmospheres* **117**(D19).

Pryor, S. C., Shephard, T. J. and Barthelmie, R. J. (2018), 'Interannual variability of wind climates and wind turbine annual energy productions', *Wind Energy Science* **3**, 651–665.

Racherla, P., Shindell, D. and Faluvegi, G. (2012), 'The added value to global model projections of climate change by dynamical downscaling: A case study over the continental us using the giss-modele2 and wrf models', *Journal of Geophysical Research: Atmospheres* **117**(D20).

Read, L. K. and Vogel, R. M. (2015), 'Reliability, return periods, and risk under nonstationarity', *Water Resources Research* **51**(8), 6381–6398.

Renard, B., Sun, X. and Lang, M. (2013), *Bayesian methods for non-stationary extreme value analysis*, Springer Netherlands, Dordrecht, pp. 39–95.

Reynolds, O. (1895), 'Iv. on the dynamical theory of incompressible viscous fluids and the determination of the criterion', *Philosophical transactions of the royal society of london.(a.)* (186), 123–164.

Seneviratne, S. I., Nicholls, N., Easterling, D., Goodess, C. M., Kanae, S., Kossin, J., Luo, Y., Marengo, J., McInnes, K., Rahimi, M., Reichstein, M., Sorteberg, A., Vera, C. and Zhang, X. (2017), *An IPCC special report on the impacts of global warming of 1.5 °C above pre-industrial levels and related global greenhouse gas emission pathways, in the context of strengthening the global response to the threat of climate change, sustainable development, and efforts to eradicate poverty*, in , chapter Changes in climate extremes and their impacts on the natural physical environment.

Vandal, T., Kodra, E., Ganguly, S., Michaelis, A., Nemani, R. and Ganguly, A. R. (2017), Deepsd: Generating high resolution climate change projections through single image super-resolution, *in* 'Proceedings of the 23rd acm sigkdd international conference on knowledge discovery and data mining', pp. 1663–1672.

Vickery, P. J. and Skerlj, P. F. (2005), 'Hurricane gust factors revisited', *Journal of Structural Engineering* **131**(5), 825–832.

Vickery, P., Wadhera, D., Galsworth, J., Peterka, J. A., Irwin, P. and Griffis, L. (2010), 'Ultimate wind load design gust wind speeds in the united states for use in asce-7', *Journal of Structural Engineering* **36**(5), 613–625.

World Economic Forum (2020), 'Global risks report 2020: An unsettled world'.

Xu, Y. (2019), 'Estimates of changes in surface wind and temperature extremes in southwestern norway using dynamical downscaling method under future climate', *Weather and Climate Extremes* **26**, 1721.